

## Experimental and numerical study of fatigue behaviour at the microscale of cementitious materials

Gan, Y.

**DOI**

[10.4233/uuid:4fd952d3-f892-4567-8e51-e6623c7a6650](https://doi.org/10.4233/uuid:4fd952d3-f892-4567-8e51-e6623c7a6650)

**Publication date**

2022

**Document Version**

Final published version

**Citation (APA)**

Gan, Y. (2022). *Experimental and numerical study of fatigue behaviour at the microscale of cementitious materials*. [Dissertation (TU Delft), Delft University of Technology]. <https://doi.org/10.4233/uuid:4fd952d3-f892-4567-8e51-e6623c7a6650>

**Important note**

To cite this publication, please use the final published version (if applicable). Please check the document version above.

**Copyright**

Other than for strictly personal use, it is not permitted to download, forward or distribute the text or part of it, without the consent of the author(s) and/or copyright holder(s), unless the work is under an open content license such as Creative Commons.

**Takedown policy**

Please contact us and provide details if you believe this document breaches copyrights. We will remove access to the work immediately and investigate your claim.

**Experimental and numerical study of fatigue behaviour at  
the microscale of cementitious materials**

Yidong Gan  
甘屹东



# **Experimental and numerical study of fatigue behaviour at the microscale of cementitious materials**

## **Dissertation**

for the purpose of obtaining the degree of doctor  
at Delft University of Technology  
by the authority of the Rector Magnificus, Prof.dr.ir. T.H.J.J. van der Hagen,  
chair of the Board for Doctorates  
to be defended publicly on  
Monday 12 September 2022 at 12:30 o'clock

by

**Yidong GAN**

Master of Engineering in Bridge Engineering,  
Hunan University, P.R. China,  
born in Hunan, P.R. China

This dissertation has been approved by the promotor

Composition of the doctoral committee:

Rector Magnificus,	chairperson
Prof. dr. ir. K. van Breugel	Delft University of Technology, promoter
Prof. dr. ir. E. Schlangen	Delft University of Technology, promoter
Dr. B. Šavija	Delft University of Technology, copromoter

Independent members:

Prof. W. Chen	Wuhan University of Technology, China
Prof. H. Stang	Technical University of Denmark, Denmark
Prof. dr.ir. L.J. Sluys	Delft University of Technology
Prof. dr.ir. R. Benedictus	Delft University of Technology
Prof. dr.ir. M.A.N. Hendriks	Delft University of Technology, reserve member



Keywords: Cementitious materials, cement paste, fatigue, lattice fracture model, X-ray computed tomography, nanoindentater

Printed by Ipskamp Printing, The Netherlands

Cover design: Jingcun Cheng

ISBN: 978-94-6421-840-4

Copyright © 2022 by Yidong Gan

All rights reserved. No part of the material protected by this copyright notice may be reproduced or utilized in any form or by any means, electronic or mechanical, including photocopying, recording or by any information storage and retrieval system, without written consent from the author.

*To my family*



# Content

List of symbols	vi
List of abbreviations	viii
List of figures	ix
List of tables	xiii

## **Chapter 1 .....1**

### **General introduction**

1.1 Research Background .....	2
1.1.1 General ageing phenomenon .....	2
1.1.2 Fatigue of concrete.....	3
1.2 Objective and scope .....	5
1.3 Strategy of the research .....	9
1.4 Outline of the thesis .....	7
References .....	9

## **Chapter 2 ..... 12**

### **Literature review**

2.1 Introduction.....	13
2.2 Factors influencing fatigue behaviour .....	14
2.2.1 Factors for material composition .....	14
Effect of w/c ratio.....	14
Effect of binder type.....	14
Effect of fibre addition .....	15
2.2.2 Factors for loading scenario .....	15
Effect of loading frequency .....	15
Effect of rest period.....	16
Effect of variable amplitude .....	16
2.3 Experimental characterisation of fatigue damage .....	17
2.3.1 Direct approach of damage characterisation.....	17
2D microscope observation.....	17
3D X-Ray computed tomography .....	20
2.3.2 Indirect approach of damage characterisation .....	22
Stiffness degradation.....	22
Acoustic emission technique .....	23

Electrical resistivity measurement .....	23
Pore structure change .....	23
2.3.3 General remarks .....	24
2.4 Models and theories for fatigue analysis .....	25
2.4.1 Wöhler curve .....	25
2.4.2 Paris' law .....	25
2.4.3 Cohesive zone model .....	28
2.4.4 Damage mechanics.....	30
2.4.5 General remarks .....	31
2.5 Conclusions .....	32
References .....	34

## **Chapter 3 .....** 41

### **Miromechanical and fatigue properties of cement paste at microscale**

3.1 Introduction .....	42
3.2 Experimental approach .....	43
3.2.1 Materials .....	43
3.2.2 Preparation of micro-cantilever beams .....	43
3.2.3 Experimental set-up .....	44
Quasi-static bending test.....	45
Fatigue bending test.....	46
3.3 Experimental results and discussion .....	50
3.3.1 Mechanical properties measured in quasi-static tests .....	50
3.3.2 Fatigue life and <i>S-N</i> curve.....	51
3.3.3 Evolution of fatigue damage .....	54
Changes in MCB stiffness .....	54
Fatigue damage evaluation through XCT .....	55
3.3.4 ESEM analysis of fracture surface .....	56
3.3.5 Development of fatigue compliance .....	61
3.4 Conclusions .....	63
References .....	65

## **Chapter 4 .....** 71

### **Miromechanical and fatigue properties of ITZ at microscale**

4.1 Introduction .....	72
4.2 Experimental approach .....	73
4.2.1 Materials and sample preparation.....	73



4.2.2 Quasi-static and fatigue bending test .....	78
Quasi-static bending test.....	79
Fatigue bending test.....	80
4.3 Experimental results and discussion .....	82
4.3.1 Mechanical properties measured in quasi-static tests .....	82
4.3.2 Fatigue properties .....	83
4.3.3 Fracture surface .....	84
4.3.4 Residual deformation.....	88
4.3.5 Stiffness variation.....	90
4.3.6 General discussion.....	92
4.4 Conclusions.....	93
References.....	95

**Chapter 5 ..... 99**

**Lattice modelling of fatigue response of cement paste at microscale**

5.1 Introduction.....	100
5.2 Numerical approach .....	101
5.2.1 Experimentally-obtained 2D virtual specimens .....	101
5.2.2 General description of lattice model.....	102
Domain discretization.....	102
Mechanical constitutive law.....	103
5.2.3 Fatigue lattice model.....	105
Constitutive law for cyclic loading .....	105
Residual deformation .....	109
5.3 Model calibration and validation.....	110
5.4 2D uniaxial tensile fatigue life and fracture behaviour .....	117
5.5 Conclusions.....	122
References.....	124

**Chapter 6 ..... 128**

**Lattice modelling of fatigue response of ITZ at microscale**

6.1 Introduction.....	129
6.2 Numerical approach .....	129
6.2.1 2D ITZ virtual specimens .....	129
6.2.2 Lattice modelling of ITZ.....	131
6.3 Model calibration and validation.....	133
6.4 2D uniaxial tensile simulation of ITZ.....	139

6.5 Conclusions .....	144
References .....	146
<b>Chapter 7 .....</b>	<b>148</b>
<b>Mesoscopic modelling of fatigue behaviour of mortar using output from microscopic modelling</b>	
7.1 Introduction .....	149
7.2 Numerical approach .....	150
7.2.1 2D mortar virtual specimens .....	150
7.2.2 Constitutive law for mortar simulation .....	151
7.3 Result and discussion .....	154
7.3.1 Uniaxial tensile fracture simulation .....	154
7.3.2 Uniaxial fatigue simulation .....	156
7.3.3 Fatigue damage evolution .....	157
7.4 Conclusions .....	161
References .....	163
<b>Chapter 8 .....</b>	<b>166</b>
<b>Retrospection, conclusions and prospects</b>	
8.1 Retrospection .....	167
8.2 Conclusions .....	168
8.3 Prospects .....	170
Summary .....	172
Samenvatting .....	174
Acknowledgements .....	176
List of publications .....	179
Curriculum vitae .....	181



## List of symbols

---

$a, b$	material coefficients for Wöhler fatigue equation	[-]
$\Delta a$	incremental crack length due to fatigue	[m]
$A$	cross-section area of the beam element	[ $\mu\text{m}^2$ ]
$C(t)$	fatigue compliance	[ $10^{-6}/\text{MPa}$ ]
$d$	fractured length	[ $\mu\text{m}$ ]
$d_{soft}$	constant percentage of reduction in strength	[%]
$D$	fatigue damage index	[-]
$D_i$	fatigue damage index at the $i$ -th analysis step	[-]
$E_{d1}$	elastic modulus of damaged element due to fatigue	[GPa]
$E_n$	elastic modulus of the element	[GPa]
$E_{static}$	static elastic modulus	[GPa]
$f_a, f_b$	remaining strength of the damaged element due to fatigue	[MPa]
$f_{fz}$	loading frequency	[Hz]
$f_t$	flexural strength	[MPa]
$F_{max}$	maximum fatigue load	[mN]
$J_{tot}$	total material compliance under cyclic loading	[ $10^{-6}/\text{MPa}$ ]
$J(t, t_0)$	basic creep compliance	[ $10^{-6}/\text{MPa}$ ]
$\Delta J_f$	fatigue compliance due to the crack growth	[ $10^{-6}/\text{MPa}$ ]
$h$	side length of the square beam cross-section	[ $\mu\text{m}$ ]
$I$	moment of inertia	[ $\mu\text{m}^4$ ]
$k$	slope of load-displacement curve	[mN/ $\mu\text{m}$ ]
$k_{int}$	initial stiffness of specimen	[mN/ $\mu\text{m}$ ]
$\Delta K$	stress intensity factor range	[ $\text{MPa}\cdot\text{m}^{1/2}$ ]
$L$	the loading length of beam	[ $\mu\text{m}$ ]
$M$	local bending moment of the element	[mN $\cdot\mu\text{m}$ ]
$N$	number of cycles	[-]
$N_a$	local normal force of the element	[mN]
$N_i$	fatigue life of element at the $i$ -th analysis step	[-]
$N_f$	fatigue life of specimen	[-]
$R$	the ratio of minimum fatigue stress to the maximum fatigue stress	[-]
$R_a$	arithmetic mean height of a line	[ $\mu\text{m}$ ]
$S$	stress level	[%]
$S_a$	arithmetic mean height of a surface	[ $\mu\text{m}$ ]
$S_i$	stress level of the element at the $i$ -th analysis step	[%]
$S_q$	root mean square height of a surface	[ $\mu\text{m}$ ]
$S_{nom}$	nominal stress levels	[%]
$S_{mod}$	modified stress levels	[%]
$t$	fatigue loading time	[s]
$t_0$	time at the beginning of fatigue loading	[s]
$t_1$	time unit	[s]
$t_i$	time at the $i$ -th step	[s]
$W$	cross-sectional moment of resistance	[ $\mu\text{m}^3$ ]
$\alpha$	specific basic creep compliance of specimen at 1 s	[ $10^{-6}/\text{MPa}$ ]
$\alpha_c$	specific basic creep compliance of element at 1 s	[ $10^{-6}/\text{MPa}$ ]
$\alpha_M$	bending influence factor	[-]
$\alpha_N$	normal force influence factor	[-]
$\beta$	exponent in creep function of specimen	[-]
$\beta_c$	exponent in creep function of element	[-]
$\epsilon_0$	strain at the peak stress	[ $\mu\text{m}/\mu\text{m}$ ]

$\varepsilon_a, \varepsilon_b$	strain at the remaining strength of element	[ $\mu\text{m}/\mu\text{m}$ ]
$\varepsilon_c$	constant compressive strain	[ $\mu\text{m}/\mu\text{m}$ ]
$\varepsilon_f$	residual strain at the highest comparative stress of element	[ $\mu\text{m}/\mu\text{m}$ ]
$\varepsilon_{p1}, \varepsilon_{p2}$	residual strain of element	[ $\mu\text{m}/\mu\text{m}$ ]
$\varepsilon(t)$	strain for the upper fibre of beam at the fixed end	[ $\mu\text{m}/\mu\text{m}$ ]
$\varepsilon_{ve}$	viscoelastic strain	[ $\mu\text{m}/\mu\text{m}$ ]
$\varepsilon_{max}$	maximum strain of element	[ $\mu\text{m}/\mu\text{m}$ ]
$\sigma$	stress of specimen	[MPa]
$\sigma_c$	comparative stress of element	[MPa]
$\sigma_{sf}$	highest comparative stress of element	[MPa]
$\sigma_{max}$	applied maximum stress	[MPa]
$\Delta\sigma$	fatigue stress amplitude	[MPa]
$\delta$	displacement of the indenter tip	[ $\mu\text{m}$ ]
$\gamma$	constant exponent	[-]

## List of abbreviations

---

AE	Acoustic emission
AFm	Monosulfate
AFt	Ettringite
BSE	Backscattered electron
BSP	Boltzmann superposition principle
CaCO <sub>3</sub>	Calcium carbonate
CFM	Continuous function model
CH	Calcium hydroxide
C-S-H	Calcium-silicate-hydrate
EDS	Energy-dispersive X-ray spectroscopy
ESEM	Environmental Scanning Electron Microscope
FIB	Focused ion beam
FPZ	Fracture process zone
GGBS	Ground granulated blast-furnace slag
HD	High-density
ITZ	Interfacial transition zone
LD	Low-density
MCB	Micro-cantilever beam
MIP	Mercury intrusion porosimetry
RBSM	Rigid Body Spring Method
RH	Relative humidity
ROI	Region of interest
SE	Secondary electron
SEM	Scanning electron microscopy
S-N	Stress versus fatigue life curve
TEM	Transmission electron microscopy
UHC	Unhydrated cement
UHPC	Ultra-High Performance Concrete
XCT	X-ray computed tomography
3DMA	Three Dimensional Medial Axis Analysis

## List of figures

---

- Figure 1-1 Evolution of the performance of an ageing system
- Figure 1-2 A multiscale view of heterogeneous cement-based materials
- Figure 1-3 Outline of the thesis
- Figure 2-1 (a) A microscope image of microcracks oriented parallel to the load direction with crack widths in a longitudinal section of a specimen that has been damaged for up to 90% of the fatigue life; (b) SEM image of the crack pattern near an aggregate; (c) SEM image of the crack pattern in paste matrix
- Figure 2-2 High-angle annular dark field STEM images of UHPC cement paste under the compressive fatigue loading
- Figure 2-3 The distribution of medial axis (the warm color is a small burn number and the cold color represents a large burn number; the red color represents burn number 1) and the amount of burn number in cubic concrete specimens ( $10 \times 10 \times 10 \text{ mm}^3$ ) under the stress level of (a) 0%, (b) 60% and (c) 90%
- Figure 2-4 The ICT images for (a) the fatigue damage evolution in concrete specimens with the size of 50 mm in diameter and 100 mm in height under compressive fatigue loading and (b) the distribution of detected pores under the stress level of 80%
- Figure 2-5 Illustration of the fatigue damage evolution under compressive fatigue loading
- Figure 2-6 The assumed fracture of the nanoscale element for (a) an atomic lattice block; (b) a disordered system of nanoparticles of the calcium silicate hydrate
- Figure 2-7 The fictitious crack model (a) the assumed stress distribution near the crack; (b) the assumed linear relationship between the stress and the crack opening displacement
- Figure 2-8 The description of continuous function model
- Figure 2-9 The numerical results of mesoscopic model based on RBSM for tensile fatigue: (a) an example of the tensile fatigue fracture pattern (red particles represent aggregate and grey for mortar) (b) the strain history in fatigue simulation under 80% of tensile strength
- Figure 3-1 Schematic diagram of sample preparation
- Figure 3-2 Backscattered electron image of the cross-sections of MCB with w/c 0.4
- Figure 3-3 Secondary electron image of the diamond cylindrical wedge tip with an enlarged view of the tip head
- Figure 3-4 Schematic diagram of test set-up
- Figure 3-5 Cyclic load history applied in MCB fatigue tests
- Figure 3-6 Typical displacement-number of cycles curve
- Figure 3-7 Typical development of residual strain at the maximum fatigue load
- Figure 3-8 The CT scanning of the micro-cantilever beams and segmented pore structure
- Figure 3-9 Typical load-displacement curve of MCB (w/c 0.4, 28d) under monotonic loading
- Figure 3-10 The relationship between the elastic modulus and flexural strength (28d)
- Figure 3-11 The nominal stress level versus number of cycles to failure
- Figure 3-12 The modified stress level versus number of cycles to failure
- Figure 3-13 Stiffness degradations of 10 MCBs (28d) for each w/c ratio under cyclic loading (note that vertical axis does not start at zero)
- Figure 3-14 XCT examination of fatigue damage in MCBs (w/c 0.4)
- Figure 3-15 The overview of static and fatigue fractured surfaces (w/c 0.5)

- Figure 3-16 The (a) BSE image; (b) SE image of tensile zone of MCB after static failure (w/c 0.5)
- Figure 3-17 The (a) BSE image; (b) SE image of tensile zone of MCB after fatigue failure (w/c 0.5)
- Figure 3-18 Three static fractured surfaces of MCBs and marked cracks
- Figure 3-19 Three fatigue fractured surfaces of MCBs and marked cracks with (a)  $N_f = 63544$ ; (b)  $N_f = 35045$  and (c)  $N_f = 10328$
- Figure 3-20 The evolution of fatigue compliance for (a) w/c 0.4 and (b) w/c 0.5
- Figure 3-21 The comparison of fatigue compliance curves for w/c 0.4 between test data and BSP based calculations
- Figure 4-1 (a) A slice of quartzite aggregate with the thickness of around 1 mm; (b) 3D contour map of surface roughness; (c) BSE image and EDS of aggregate surface and (d) SE image of quartz crystals
- Figure 4-2 Backscattered electron images of (a) the side view of ITZ and (b) the cross-sections of ITZ samples with w/c 0.4, 28 days
- Figure 4-3 The 3D XCT results of w/c 0.3 ITZ beam samples and the detected porosity distribution calculated based on segmented 2D slices
- Figure 4-4 The segmented pores and unhydrated cement particles in the ROI of two ITZ samples per w/c ratio (grey represents hydration products)
- Figure 4-5 Schematic diagram of test set-up (d is the distance between the load point and the boundary of the aggregate)
- Figure 4-6 Load-displacement curves for ITZ samples with two w/c ratios
- Figure 4-7 Illustration of cyclic load history applied in MCB fatigue tests
- Figure 4-8 Examples of load-displacement curves for two cycle blocks
- Figure 4-9 Illustration of residual displacement and loading stiffness calculation
- Figure 4-10 The comparison of (a) the flexural strength and (b) elastic modulus of ITZ sample (28 d) and the cement paste sample
- Figure 4-11 The *S-N* curves for ITZ samples and the comparison with the results of pure cement paste samples
- Figure 4-12 The front views and side views of fractured ITZ samples subjected to (a) monotonic loading and (b) cyclic loading
- Figure 4-13 (a) Some large CH crystals with preferred orientation observed on the aggregate surface after static fracture; (b) the images of hydration products and small cavities at higher magnifications and (c) schematic presentation of the hydration products distribution on the aggregate surface (Note that the sketch is used for illustration purposes only and the shape and sizes of hydration products are not exact)
- Figure 4-14 The evolution curves of residual displacement for (a) w/c 0.3 and (b) w/c 0.4 ITZ specimens
- Figure 4-15 Comparison of fatigue compliance curves for ITZ and cement paste specimens from Chapter 3
- Figure 4-16 The evolutions of normalized stiffness during multiple cycle blocks for (a) w/c 0.3 ITZ samples, and (b) w/c 0.4 ITZ samples. Note that the  $k_1$  is the loading stiffness of the first cycle in a cycle block and  $k_i$  is the *i*-th cycle loading stiffness
- Figure 4-17 Normalized stiffness evolution at the final cycle block
- Figure 5-1 (a) the CT image of a micro-cantilever beam; (b) segmentation results for different w/c ratios
- Figure 5-2 Lattice element generation procedure
- Figure 5-3 Simulation results of one w/c 0.4 sample ( $1650 \mu\text{m} \times 300 \mu\text{m}$ ): (a) the fracture pattern under static loading; (b) the comparison of the stress-strain curve with experimental results
- Figure 5-4 The constitutive law of individual lattice elements subjected to cyclic loading



- Figure 5-5 The effect of cycle block value on the simulated fatigue life and computational time
- Figure 5-6 The comparison of experimentally measured fatigue compliances and simulation results (w/c 0.4 and 0.5, 28 days)
- Figure 5-7 The effect of  $b$  on the simulated  $S-N$  curves
- Figure 5-8 Simulated  $S-N$  curves for one virtual sample (w/c 0.4, 28 days) using different fatigue parameters
- Figure 5-9 The simulated  $S-N$  curves for different virtual samples
- Figure 5-10 Examples of the fatigue fracture patterns for w/c 0.4 and 0.5 virtual samples
- Figure 5-11 A typical simulated stress-strain curve for one w/c 0.4 sample under cyclic loading with the upper stress level of 90%
- Figure 5-12 The stress evolutions of different types of upper fiber beam elements in the region of interest under cyclic loading: (a) fracture pattern; (b) location 1 and (c) location 2
- Figure 5-13 The simulated elastic modulus degradation along with the experimental results
- Figure 5-14 The generated lattice model from CT scans for uniaxial tensile fatigue simulation
- Figure 5-15 Simulated uniaxial tensile fatigue  $S-N$  curves for w/c 0.4 virtual samples
- Figure 5-16 One example of fatigue crack development in cement paste (w/c 0.4) under uniaxial tensile fatigue loading at the stress level of 87.4% and the simulated fatigue life  $N_f$  is 37470
- Figure 5-17 Different fatigue fracture behaviours of cement pastes (w/c 0.4) under the (a) stress level of 85% (fatigue life  $N_f=3053$ ); and (b) the stress level of 50% (fatigue life  $N_f=3572216$ )
- Figure 6-1 The 3D XCT results of w/c 0.3 ITZ beam samples and 2D slices
- Figure 6-2 The 2D XCT images of w/c 0.4 paste-aggregate composites with different aggregate surfaces
- Figure 6-3 Lattice element generation procedure (grey pixel represents cement paste, orange represents aggregate and blue represents pore)
- Figure 6-4 Generation lattice model based on 2D images of ITZ microstructures with different surface textures (black pixel represents UHC, orange represents aggregate, yellow represents LD C-S-H and red represents HD C-S-H)
- Figure 6-5 Comparison of simulated load-displacement curves and fracture patterns of ITZ beams with the w/c ratio of 0.3 using three different sets of local mechanical properties, see Table 6-1
- Figure 6-6 Comparison of experimentally measured load-displacement curves and simulation results of (a) w/c 0.3 and (b) w/c 0.4
- Figure 6-7 Simulated  $S-N$  results using 13 different sets of local fatigue properties and the comparison with experimental results in Chapter 4
- Figure 6-8 The simulated results of (a) applied stress magnitude-fatigue life curves and (b) stress level-fatigue life curves
- Figure 6-9 The simulated evolution of sample stiffness
- Figure 6-10 The simulated stress-strain diagrams of ITZ models with (a) flat aggregate surfaces and (b) natural rough surfaces under uniaxial tension
- Figure 6-11 The crack patterns for different ITZ models
- Figure 6-12 (a) The comparison of  $S-N$  curves between cement paste and ITZ; (b) The relationship between the applied stress and number of cycles to failure
- Figure 6-13 The variation of ITZ stiffness during the whole fatigue life under uniaxial tensile fatigue loading
- Figure 7-1 An irregular shape particle described by spherical harmonics
- Figure 7-2 The 3D digital mortar sample ( $50 \times 50 \times 50$  mm<sup>3</sup>) and the extracted 2D slice (red represents sand, grey represents paste matrix and blue is pore)

- Figure 7-3      Approximations of the non-linear stress-strain responses of paste matrix and ITZ using multi-linear curves
- Figure 7-4      The simulated stress-strain curves of mortar for (a) the ‘weak’ ITZ and (b) ‘strong’ ITZ
- Figure 7-5      The simulated fracture patterns of mortar samples with different ITZ properties (yellow represents the paste matrix, grey represents the ITZ and the orange represents the aggregate, and the crack is blue)
- Figure 7-6      The comparison of experimental and numerical *S-N* results
- Figure 7-7      The contour maps of fatigue damage at different stages of cyclic loading at the stress level of 60% for virtual mortar samples with (a) the weak ITZ (Mortar\_F\_2,  $N_f=30486$ ) and (b) the strong ITZ (Mortar\_R\_2,  $N_f=660866$ )
- Figure 7-8      The contour maps of fatigue damage at different stress levels for virtual mortar samples (a) Mortar\_R\_4,  $N_f=661074$  (60%), 10670 (80%) and (b) Mortar\_F\_7,  $N_f=34543$  (60%), 10918 (80%)

## List of tables

---

Table 3-1	Measured porosities and mechanical properties of MCBs (28d)
Table 5-1	Local properties for different phases of hydrated cement paste
Table 5-2	Calibrated parameters for the fatigue simulation
Table 5-3	The simulation results for 8 virtual samples under uniaxial tensile fatigue
Table 6-1	Local properties for different interfacial phases
Table 6-2	Local mechanical properties of different phases in paste-aggregate composite
Table 6-3	Local fatigue parameters of different phases in paste-aggregate composite
Table 6-4	The summary of ITZ models
Table 7-1	Step-wise constitutive relations of cement paste and ITZ up-scaled from the microscopic modelling in Chapter 5 and 6 (Interface 1: strong ITZ, Interface 2: weak ITZ)
Table 7-2	Local fatigue properties of different phases in mortar (Interface 1: strong ITZ, Interface 2: weak ITZ)



# 1

## GENERAL INTRODUCTION

*This chapter introduces the background and motivation of the current research. The urgency and challenges of ageing concrete structures are addressed. The focus is then fixed to one of the typical ageing phenomena, i.e., the fatigue of concrete. The layout of the thesis, objectives, methodology and scope of the research are given.*

## 1.1 RESEARCH BACKGROUND

### 1.1.1 GENERAL AGEING PHENOMENON

Ageing is an inherent feature of natural and man-made materials, including cementitious materials [1]. Ageing can be defined as the change of performance of materials, structures or systems with elapsed time. The origin of ageing can be traced back to the atomic scale, where fundamental entities are continuously moving with a probability to leave their original position. It is the nature of all matter and lies at the basis of ageing processes. In addition, a variety of gradients at different scales, e.g. temperature, humidity and ion concentration, are driving forces of ageing, promoting changes with elapsed time. Therefore, ageing research must be multi-scale and multi-disciplinary.

The ageing phenomenon involves slow and irreversible alteration of chemical or physical (micro)structures, which is generally detrimental to the material properties. It may lead to the gradual loss of the function of a structure or a system with increasing likelihood of failure. According to [2], a substantial part of the world's infrastructure structures has been built between the fifties and eighties of the past century. Their average service life is around 50 to 80 years. This means that these structures have experienced ageing for a long time and will reach the end of their lifetime in the coming decades. A vast investment on the maintenance and repair of the structures is inevitable, and is already becoming a huge financial burden for the society.

Although the awareness of ageing has increased recently, one major concern is that people simply do not know what condition a structure is in, nor how its condition is changing over its lifetime. In other words, it is difficult to predict the ageing process as it may start already in the stage that a structure is still performing well according to its specifications. Figure 1-1 illustrates the evolution of the performance of an ageing system. It indicates that after a short period of 'teething' problems, the system will reach the required level of performance. That is the level at which the system should demonstrate its capacity to meet safety and functional criteria. This seems to be a dormant period, where 'nothing happens' at the macroscale. However, multiple hidden ageing processes at lower scales are actually ongoing and lead to imperceptible changes of system performance. After a certain period, the performance of the system starts to decay. If timely and appropriate maintenance or repair is not provided to the system, this may lead to disastrous consequences.

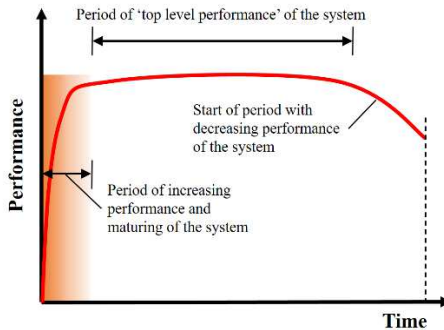


Figure 1-1 Evolution of the performance of an ageing system [1]

The understanding of ageing mechanisms at the material level is the key to dealing with ageing issues. Based on the knowledge at the fundamental level, reliable models can be developed to describe and predict the change of performance of a system with time. An associated challenge is the development of appropriate tests, which are also needed to validate these predictive models. By using these predictive tools, we should be able to design materials and structures such that their service life can be extended and savings can be harvested, and to better plan and predict repair and maintenance activities. Furthermore, it may help in making decisions whether a structure should be demolished or repaired.

### 1.1.2 FATIGUE OF CONCRETE

As one of the typical ageing phenomena, fatigue is usually defined as a process of progressive, permanent change in the internal structure of the material [3,4]. These changes are mainly attributed to the progressive growth of internal microcracks, which may eventually coalesce into macrocracks and lead to the complete fracture [5,6]. Many concrete structures, such as off-shore structures, tall buildings, roads and bridges, are inevitably subjected to fatigue or some kind of cyclic loading [7–9]. As far as the cyclic loading is concerned, this could be caused by environmental factors, e.g., winds, waves and temperature differences, or it may also be due to mechanical effects such as the passage of vehicles or trains, machine tool loading and impacts.

The fatigue of concrete has received considerable research attention. There are several reasons for the recent interest in this type of loading for concrete [10]. Firstly, it has been recognised that the fatigue loading may have significant influence on the material properties, especially on the mechanical and transport properties. Secondly,

the growth of serious overloading due to the raising number of heavy vehicles on concrete bridges or pavements is a major cause for accelerating ageing of transportation infrastructures. In addition, more slender and light concrete structures have recently been built thanks to the application of high strength concrete and lightweight concrete, accompanied by reductions in safety margins. This further increases the percentage of the live load in the total load and accelerates the fatigue damage evolution in concrete structures. Generally, fatigue failure in structural components occurs suddenly under cyclic loads with a magnitude much lower than their static load bearing capacity [6,11]. Moreover, hardly noticeable fatigue induced damage that accumulates over a long time could also severely deteriorate concrete structures [12,13]. Therefore, a clear understanding the fatigue behaviour of concrete is of great importance for ensuring the safety and durability of these structures.

The phenomenon of concrete fatigue is very complex as it involves multiple spatial scales owing to the multiscale heterogeneous nature of concrete [14,15]. Figure 1-2 illustrates the material structures of cement-based material at different length scales: at the nanoscale, the calcium-silicate-hydrate (C-S-H) is generally considered as the 'basic building blocks' of concrete [16], which has a sheet-like molecular structure [17]; the packing of these C-S-H sheets further forms the C-S-H globule (or C-S-H particle) at the sub-microscale [18]; for the main binding phase in the concrete, i.e., the cement paste, different packing densities of C-S-H particles, along with unhydrated cement (UHC) grains, capillary pores and other hydration products can be recognised at the microscale; while at the mesoscale, the cement paste becomes the main constituent of the mortar, which also comprises small aggregates and the interfacial transition zone (ITZ) between the aggregate and the paste matrix; when the larger aggregates are added, the length scale moves up to the concrete level; eventually, at the macroscale or structural level, the concrete can be simply considered as a homogeneous and isotropic solid, which facilitates the design of concrete structures. Besides, the presences of numerous pores and cracks ranging from sub-nanometres to centimetres, along with the wide scope of sizes of ingredients in concrete, lead to complex mechanical interactions, i.e. fracture and crack propagation, at different scales [19]. Therefore, the concrete can be considered as a complicated system [20]. To address the essential question of how the fatigue fracture process happening at smaller scales affects the macroscopic fatigue performance of concrete, experiments and simulations are needed at every scale.



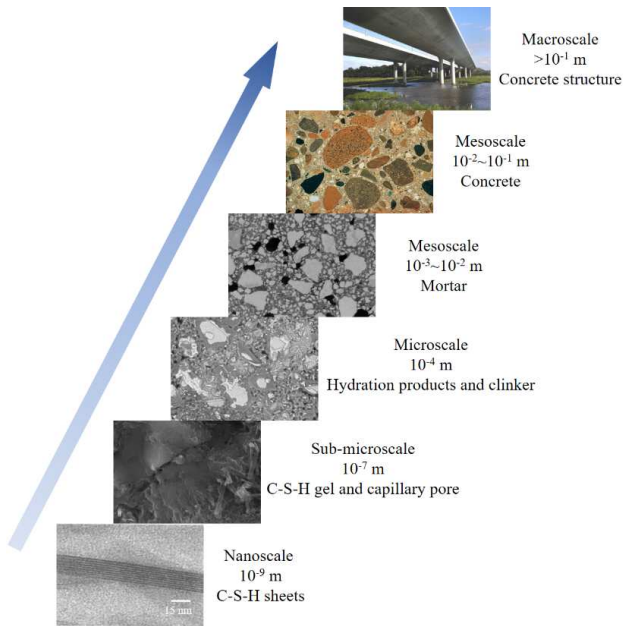


Figure 1-2 A multiscale view of heterogeneous cement-based materials adapted from [17,21–23]

## 1.2 OBJECTIVE AND SCOPE

This work aims to improve the knowledge regarding the fatigue behaviour of cementitious materials at the microscale and to develop a multiscale modelling scheme from micro- to mesoscale to estimate the fatigue properties. This study also aims to reveal the fatigue damage and residual deformation evolution in cementitious materials, and offer a reference to engineers and researchers for assessing the ageing of concrete structures subjected to the cyclic loading, and to designers for designing structures to meet their expected service life. The main objective is achieved through the following objectives:

- Development of novel experimental techniques for characterisation of mechanical and fatigue properties of cementitious materials at the microscale. This includes preparation and testing of micrometre sized specimens.
- Investigation of fatigue fracture, fatigue damage and residual deformation evolution of cement paste and ITZ at the microscale.

- Development of a modelling approach for simulating the micromechanical and fatigue behaviour of cementitious materials. The microstructures of cement paste and ITZ need to be considered in the model. The input parameters for micromechanical and fatigue properties of constituents in cement paste and ITZ need to be identified through a calibration and validation procedure using experimental results.

- Development of a proper upscaling approach that could bridge two scales, i.e. micro and mesoscale. In this approach, the mechanical and fatigue properties obtained at the microscale can be directly used as the inputs in the mesoscopic simulations of mortar. Therefore, the origin and evolution of the fatigue fracture process at a lower scale can be captured and their impacts at a higher scale of observation can be reproduced.

- Investigation of the effect of material structure at different length scales on the macroscopic fatigue performance of cementitious materials using the developed model.

In this research, ordinary Portland cement CEM I 42.5 N is used as the binder of cementitious materials. In total three w/c ratios, i.e. 0.3 0.4 and 0.5, are used in this study. All specimens are cured in sealed conditions at room temperature for 28 days. The experimental work focuses on the flexural fatigue properties of cementitious materials. With regard to the fatigue loading scheme, only the cyclic load with a constant stress amplitude is used. In the numerical investigation, both the flexural and uniaxial fatigue behaviour is simulated and analysed. Since significant computational time is required for the fatigue simulation, the two-dimensional (2D) modelling is used in current study.

### 1.3 STRATEGY OF THE RESEARCH

The strategy to achieve the objectives of this research is as follows:

- Firstly, a precision micro-dicing machine is used to fabricate micrometre sized samples. With the help of a nanoindentation measurement device, micro-bending tests are performed to study the flexural fatigue behaviour of two major components in the mortar, i.e., the cement paste and the interfacial transition zone (ITZ). The fatigue life, stiffness evolution and residual deformation can be obtained from these tests. The fatigue fracture surface and damage evolution are assessed using an Environmental Scanning Electron Microscope (ESEM) and X-ray computed tomography (XCT).

- Secondly, a numerical model using a 2D lattice network is developed to simulate the fatigue behaviour of cementitious material at the microscale. Images of 2D microstructures of cement pastes and ITZ obtained from XCT tests are used as inputs and mapped to the lattice model. Different local mechanical and fatigue properties are assigned to different phases of the cement paste and interfacial transition zone. A cyclic constitutive law is proposed for considering the fatigue damage evolution. Fatigue experimental results obtained at the same length scale are used to calibrate and validate the model.

- For upscaling of the mechanical and fatigue properties, a parameter-passing scheme is adopted. In this way, the simulated output properties of cement paste from the microscale modelling are used as input properties for mesoscale modelling. The local mechanical and fatigue properties considered in the multiscale modelling mainly consist of strength, elastic modulus and the relationship between the fatigue life and stress level.
- By using the above modelling strategies, the effects of material structures on the global fatigue performance of cementitious materials can be properly simulated. This can help to understand the multi-scale fracture mechanism of such materials under fatigue loading. Possible strategies to mitigate fatigue related ageing process are discussed based on the obtained knowledge in this study.

## 1.4 OUTLINE OF THE THESIS

This thesis is divided into eight chapters, including an introduction (Chapter 1) and conclusions (Chapter 8). The thesis layout is given in Figure 1-3. This current chapter presents the general introduction. Chapter 2 gives a literature survey of the knowledge regarding fatigue behaviour of cement-based materials.

Chapter 3 presents an experimental investigation of fatigue properties of cement paste at the microscale. Micro-cantilever cyclic bending tests are performed using a nanoindenter. The size dependency of flexural fatigue life of cement paste specimen is investigated. Microscopic observations with ESEM on both static and fatigue fractured surfaces are compared. The fatigue damage evolution is assessed based on the loading stiffness evolution and observations with the XCT technique. The possible mechanisms for the development of residual deformation for cement paste subjected to cyclic loading are discussed.

In Chapter 4, the flexural strength and fatigue properties of ITZ are experimentally investigated at the micrometre length scale. The hardened cement paste cantilevers attached to a quartzite aggregate surface are prepared and tested under monotonic and cyclic load. The comparison of micromechanical and fatigue properties between the ITZ and cement paste is conducted. The results presented in Chapter 4, together with previous experimental investigations on the cement paste provides an experimental basis for a multiscale analysis of mortar in the following chapters.

Chapter 5 and Chapter 6 present a numerical model using a 2D lattice network to investigate the fatigue behaviour of cement paste and ITZ at the microscale. Microstructures and local mechanical and fatigue properties are assigned to the model. The flexural fatigue properties, in terms of  $S-N$  curve, stiffness degradation and fracture pattern, are obtained. The uniaxial tensile fatigue behaviour of the cement paste and ITZ are also simulated. The effects of microstructure and stress level on the fatigue fracture are studied using the proposed model.

Chapter 7 focuses on the multi-scale modelling scheme. The obtained mechanical and fatigue properties at the microscale are used as inputs in the mesoscopic modelling. The mesostructure of mortar is considered in the mesoscopic model. The obtained numerical results are compared with available experimental data in literature.

Chapter 8 summarizes the work in this thesis and gives conclusions and prospects. Remarks and recommendations for further research are presented.

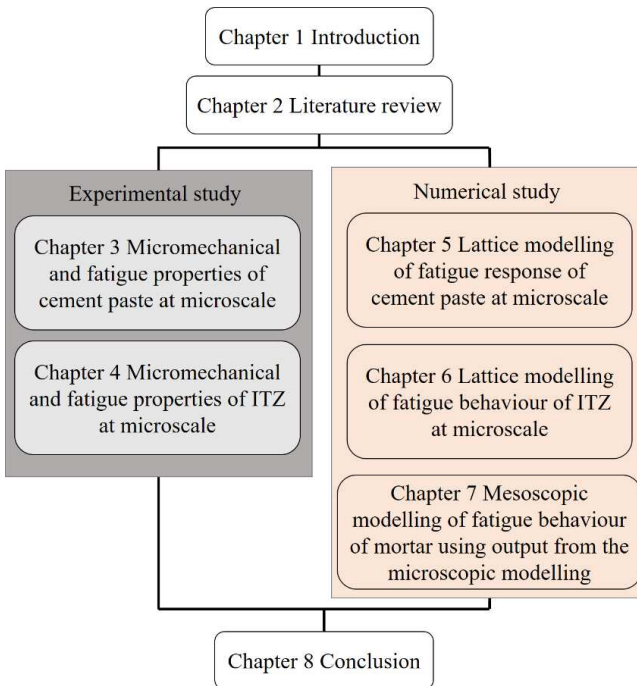


Figure 1-3 Outline of the thesis

## REFERENCES

- [1] K. van Breugel, D. Koleva, T. van Beek, *The ageing of materials and structures: Towards scientific solutions for the ageing of our assets*, 2017.
- [2] K. Van Breugel, *Societal Burden and Engineering Challenges of Ageing Infrastructure*, *Procedia Eng.* 171 (2017) 53–63.
- [3] K. Keerthana, J.M. Chandra Kishen, *An experimental and analytical study on fatigue damage in concrete under variable amplitude loading*, *Int. J. Fatigue.* 111 (2018) 278–288.
- [4] J.K. Kim, Y.Y. Kim, *Experimental study of the fatigue behavior of high strength concrete*, *Cem. Concr. Res.* 26 (1996) 1513–1523.
- [5] J. Qiu, E. Yang, *Micromechanics-based investigation of fatigue deterioration of engineered cementitious composite (ECC)*, *Cem. Concr. Res.* 95 (2017) 65–74.
- [6] Q. Li, B. Huang, S. Xu, B. Zhou, R.C. Yu, *Compressive fatigue damage and failure mechanism of fiber reinforced cementitious material with high ductility*, *Cem. Concr. Res.* 90 (2016) 174–183.
- [7] T.T.C. Hsu, *Fatigue and microcracking of concrete*, *Matériaux Constr.* 17 (1984) 51–54.
- [8] L. Gao, C.T.T. Hsu, *Fatigue of concrete under uniaxial compression cyclic loading*, *ACI Mater. J.* 95 (1998) 575–581.
- [9] T.T.C. Hsu, *Fatigue of Plain Concrete*, *ACI J. Proc.* 78 (1981) 292–304.
- [10] D. Hordijk, *Local approach to fatigue of concrete*, PhD Thesis, Delft Univ. Technol. (1991) 216.
- [11] C. Gaedicke, J. Roesler, S. Shah, *Fatigue crack growth prediction in concrete slabs*, *Int. J. Fatigue.* 31 (2009) 1309–1317.
- [12] X.H. Wang, E. Bastidas-Arteaga, Y. Gao, *Probabilistic analysis of chloride penetration in reinforced concrete subjected to pre-exposure static and fatigue loading and wetting-drying cycles*, *Eng. Fail. Anal.* 84 (2018) 205–219.
- [13] C. Fu, H. Ye, X. Jin, D. Yan, N. Jin, Z. Peng, *Chloride penetration into concrete damaged by uniaxial tensile fatigue loading*, *Constr. Build. Mater.* 125 (2016) 714–723.
- [14] K.M. Simon, J.M. Chandra Kishen, *A multiscale approach for modeling fatigue crack growth in concrete*, *Int. J. Fatigue.* 98 (2017) 1–13.
- [15] C. Pichler, R. Lackner, *Identification of logarithmic-type creep of calcium-silicate-hydrates by means of nanoindentation*, *Strain.* 45 (2009) 17–25.
- [16] M. Vandamme, F.J. Ulm, *Nanoindentation investigation of creep properties of calcium silicate hydrates*, *Cem. Concr. Res.* 52 (2013) 38–52.
- [17] A. Gmira, M. Zabat, R.J.M. Pellenq, H. Van Damme, *Microscopic physical basis of the poromechanical behavior of cement-based materials*, *Mater. Struct. Constr.* 37 (2004) 3–14.
- [18] H.M. Jennings, *Colloid model of C-S-H and implications to the problem of creep and shrinkage*, *Mater. Struct. Constr.* 37 (2004) 59–70.
- [19] J.-L. Le, Z.P. Bažant, *Unified nano-mechanics based probabilistic theory of quasibrittle and brittle structures: II. Fatigue crack growth, lifetime and scaling*, *J. Mech. Phys. Solids.* 59 (2011) 1322–1337.
- [20] K. Van Breugel, *Concrete: A material that barely deserves that qualification*, in: *Int. RILEM Conf. Mater. Sci.*, RILEM Publications SARL, 2010; pp. 13–32.
- [21] Y. Gan, H. Zhang, Y. Zhang, Y. Xu, E. Schlangen, K. van Breugel, B. Šavija, *Experimental study of flexural fatigue behaviour of cement paste at the microscale*, *Int. J. Fatigue.* 151 (2021).

- [22] M. Zhang, Multiscale Lattice Boltzman- Finite Element Modelling of Transport Properties in Cement-based Materials, 2013.
- [23] V. Brunello, C. Canevali, C. Corti, T. De Kock, L. Rampazzi, S. Recchia, A. Sansonetti, C. Tedeschi, V. Cnudde, Understanding the microstructure of mortars for cultural heritage using X-ray CT and MIP, *Materials (Basel)*. 14 (2021).



# 2

## LITERATURE REVIEW

*This chapter gives an overview on fatigue behaviour of cementitious materials. Firstly, the influencing factors for fatigue behaviour are briefly reviewed. Afterwards, a literature survey of experimental characterisation techniques for fatigue damage evolution is presented. Moreover, general models and theories for fatigue analysis are summarized. Based on the current literature state of the art, knowledge gaps that are going to be bridged in this thesis are outlined.*



## 2.1 INTRODUCTION

The word *fatigue* originated from the Latin expression *fatigāre*, which means ‘to exhaust’. Even though it is commonly used to describe the physical or mental tiredness of people, the word *fatigue* has also become a widely accepted term in engineering vocabulary for describing the damage and failure of materials under repeated loading [1]. Studies on fatigue date back to the nineteenth century, during which several disastrous railroad accidents due to fatigue were reported [2]. These tragic accidents forced railway engineers to pay serious attention to fatigue issues in metallic materials. At the beginning, fatigue was thought to be a mysterious phenomenon because fatigue failure occurred abruptly without any visible warning [3]. Therefore, numerous investigations have been conducted to understand the nature of fatigue in metals. Noteworthy research on fatigue was done by the German engineer August Wöhler, who performed the first systematic fatigue investigations on railway axles during the period 1852-1869 [4]. He developed the well-known Wöhler curve and recognised that the fatigue is a fracture phenomenon occurring after a large numbers of load cycles with the loading magnitude much lower than the strength.

Despite the early attention on fatigue of metallic materials, the interest on fatigue of cement-based material lagged for nearly 40 years. Considère and De Joly conducted the first fatigue tests on mortar specimens [5,6]. Investigations on concrete fatigue, like those on metal fatigue, were also motivated by practical problems. In general, two types of fatigue loading can be defined [7], i.e. the low-cycle fatigue with high stress levels (such as earthquakes, storms, etc.) and the high-cycle fatigue with relatively low stress levels (traffic loading, wind and wave loading, etc.). Numerous concrete structures suffer from serious safety and durability issues caused by these two types of fatigue loading [7–9]. Therefore, it is important to understand the fatigue behaviour of concrete for practical purposes. Since concrete is a quasi-brittle material with multiscale heterogeneous material structure, the mechanisms of fatigue are quite different from those of metallic materials. Fatigue crack propagation in concrete is a very complex process, involving damage accumulation at multiple length scales. The macroscopic fatigue performance of concrete not only depends on the material structure and fatigue properties of components at different scales, such as w/c ratio [10,11], porosity [11–13], binder type [14–16], addition of fibre [17–21] and aggregate type [22,23], but is also influenced by several external factors, such as temperature [24], moisture content [24,25], maximum stress level [8,26], loading frequency [27,28] and rest period [29,30], etc.

Over the past century, tremendous efforts have been devoted to concrete fatigue [31–34]. Unlike the relatively well-understood fatigue mechanisms in metal fatigue, a clear understanding of fatigue behaviour of concrete is still missing. Many important scientific problems still remain unsolved. These problems include at least: (1) how does the multiscale heterogeneous material structure of concrete affect the fatigue behaviour; (2) how does fatigue damage evolve inside the concrete; (3) how to properly simulate and predict the fatigue behaviour?

This review will be directed toward research efforts on understanding, evaluating and simulating concrete fatigue. This chapter is organized as follows: firstly, several factors influencing the fatigue behaviour of concrete are briefly reviewed; afterwards, a literature survey of experimental characterisation techniques for fatigue damage evolution is presented; in addition, general models and theories for fatigue analysis are also summarized; at the end, knowledge gaps that are going to be bridged in this thesis are outlined.

## 2.2 FACTORS INFLUENCING FATIGUE BEHAVIOUR

Fatigue behaviour of cementitious materials can be influenced by many factors. These factors can be roughly divided into two categories, i.e., the factors for material composition, such as the w/c ratio, binder type, addition of fibre, and factors for loading scenarios, such as loading frequency, rest period and variable amplitude. In this section, the effect of each factor on fatigue behaviour is briefly reviewed.

### 2.2.1 FACTORS FOR MATERIAL COMPOSITION

#### EFFECT OF W/C RATIO

Antrim [35] investigated the effect of w/c ratio on the compressive fatigue behaviour of cement paste and plain concrete. It was found that, for both paste and concrete, the number of cycles to failure is much higher for the 0.45 w/c ratio than for the 0.70 w/c ratio at a given stress magnitude. This is mainly due to the increased porosity for a higher w/c ratio. However, it should be noted that when the percentage of static strength is plotted against the fatigue life (*S-N* curve), there seems to be no discernible difference in *S-N* curve with a varying w/c ratio. This is because the w/c ratio can also substantially affect the static strength of cementitious materials [36]. Similar results have also been reported by Klaiber and Lee [10], who investigated the flexural fatigue behaviour of concrete with the w/c ratio from 0.32 to 0.60. It was found that the fatigue life decreased for lower w/c ratio (0.32) concretes. This is probably due to the shrinkage-induced damage that increased at lower w/c ratios [37,38].

#### EFFECT OF BINDER TYPE

Tse et al. [14] studied the compressive fatigue properties of concretes containing fly ash. Different replacement ratios of fly ash were tested. Compared on the basis of stress as a percentage of strength, no significant difference between fatigue strength of concrete with 50% cement replacement by fly ash and that of plain concrete was observed. However, when compared on the basis of absolute value of the applied compressive stress, the fatigue strength of concrete with 25% or 50% cement

replacement by high-calcium fly ash was significantly higher than that of plain concrete, while the fatigue strength of concrete with low-calcium fly ash was significantly lower than that of plain concrete. The authors suggested that 25% replacement of cement with low-calcium fly ash, or high-calcium fly ash with 50% replacement in concrete can lead to equivalent or even higher compressive and fatigue strengths at 28 days compared to plain concrete. Guo et al. [15] investigated the effect of different proportions of ground granulated blast-furnace slag (GGBS) on the flexural fatigue performance of 197 days old concretes. It was found that the brittleness of concrete was decreased by the incorporation of GGBS. This resulted in higher fracture energy and more tortuous cracking path of concrete. Moreover, potential hydration and pozzolanic effect of the presence of GGBS in the matrix prolonged the fatigue life compared to that of plain concrete. Specifically, the effect of GGBS on the fatigue behavior of concrete is more obvious at the lower stress levels.

### EFFECT OF FIBRE ADDITION

Studies on the fatigue behaviour of plain and fibre-reinforced concrete have been reviewed by Lee and Barr [34]. It was shown in the majority of studies that the inclusion of fibres can improve the fatigue performance of concrete. Grzybowski and Meyer [21] suggested that the addition of fibres has a dual effect on the cyclic behaviour of concrete. On one hand, fibres are able to bridge microcracks and retard their growth, thereby enhancing the composite's performance under cyclic loading. On the other hand, the presence of fibres increases the pore and initial microcrack density, resulting in a decrease of strength. Therefore, the overall outcome of these two competing effects depends on the fibre content.

## 2.2.2 FACTORS FOR LOADING SCENARIO

### EFFECT OF LOADING FREQUENCY

Graf and Brenen [39] investigated the effect of loading frequency on the fatigue life of concrete. They found that the loading frequency in the range between 4.5-7.5 Hz had little effect on the fatigue life, but when it decreased below 0.16 Hz the fatigue life decreased. Mudock [40] suggested that when the stress level was less than 75% of the tensile strength, frequencies between 1 and 15 Hz had little influence. The study of Sparks and Menzies [41] showed that for a stress level larger than 75%, the loading frequency greatly affected the fatigue life, but when the stress level is lower than 75%, frequencies between 0.1 and 100 Hz had no effect on the fatigue life. It was also argued that since the loading frequency determines the loading rate of fatigue tests, a higher loading rate may enhance the static and fatigue strength of cementitious materials [28,42].

### EFFECT OF REST PERIOD

In view of the intermittent nature of traffic loading, the effect of the length of the rest period was also studied by several researchers [29,30,43]. Hilsdorf and Kesler [29] investigated the influence of rest period on the flexural fatigue behaviour of plain concrete at the age of 7 days. They found that the fatigue strength of plain concrete increases with the introduction of periodic rest periods, indicating the occurrence of partial recovery during the rest period. This beneficial effect was found to be a function of the length of the rest period when the length is less than 5 minutes. Further increasing the length of the rest period from 5 to 27 minutes did not affect the final result. Raithby and Galloway found that a very short rest period (only 2 s) had no effect on the fatigue strength of concrete. However, it is clear that increasing rest period (up to several days or weeks) can raise the fatigue strength due to continuing hydration [40] or self-healing in the presence of water [44].

### EFFECT OF VARIABLE AMPLITUDE

Most fatigue studies have been performed to determine the influence of constant amplitude loading [45]. However, in actual concrete structures the stress cycles vary greatly in both magnitude, number and order. Oh [46] performed variable-amplitude fatigue tests on concrete beams and found that the fatigue failure of concrete is greatly influenced by the magnitude and sequence of variable-amplitude cyclic loadings. When the magnitude of fatigue loading was gradually decreased, the generated fatigue damage seemed to be larger than in the concrete subjected to increasing loading magnitude. Unfortunately, the complex damage accumulation process in concrete exposed to a more random loading is still unclear and only a few cumulative fatigue damage hypotheses have been proposed for concrete [46–48]. Among them, the Miner's law is often applied to consider the effect of variable loading amplitude [49] and it states that if there are  $k$  different stress levels and the average number of cycles to failure at the  $i$ -th stress,  $S_i$ , is  $N_i$ , then the damage fraction,  $D$ , is:

$$D = \sum_{i=1}^k \frac{n_i}{N_i} \quad (2-1)$$

where  $n_i$  is the number of cycles accumulated at stress  $S_i$ . In general, when the damage fraction  $D$  reaches 1, fatigue failure occurs. The applicability of this law in concrete fatigue has been examined by several researches [45–47,50]. Slemes [47] found that Miner's rule is useful for describing the cumulative damage due to variable-amplitude loadings. Similarly, Cornelissen and Reinhardt also suggested that Miner's law is a safe failure criterion in general. However, it was found by Holmen [50] that the variable amplitude loading seems to generate more damage than predicted by Miner's law. This is probably due to sequence effects present by variable loading. However, limited

information regarding the damage accumulation process in concrete under variable loading amplitudes can be found in the literature.

## 2.3 EXPERIMENTAL CHARACTERISATION OF FATIGUE DAMAGE

In past decades, many experimental techniques have been used to characterise the fatigue damage in concrete. Depending on how the fatigue damage is revealed, these techniques can be classified into two types: direct and indirect approaches.

- 1) Direct approaches include the microscope, scanning electron microscopy (SEM) and X-ray computed tomography (XCT) technique, which are able to visualise the propagation of microcracking under fatigue loading.
- 2) Indirect approaches include the stiffness degradation measurements, acoustic emission technique, electrical resistivity measurements, variations in pore structure and transport properties. In this case, the fatigue damage is indirectly evaluated by monitoring the change of other properties. In this section, experimental characterisations of fatigue damage evolution using these two types of method are reviewed and some obtained insights are presented and discussed.

### 2.3.1 DIRECT APPROACH OF DAMAGE CHARACTERISATION

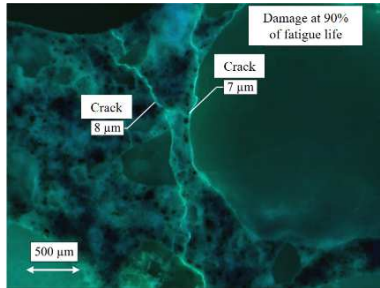
#### 2D MICROSCOPE OBSERVATION

Through direct microscopic observation many characteristics of fatigue cracks, such as the size, number and distribution, can be examined. However, due to the limitation of nano- and micro-structural characterization techniques, the fatigue fracture behaviour can only be examined at a certain length scale. In the late 1980s, Saito [51] used a stereoscopic microscope to determine the type and amount of microcracking in slices cut from normal weight concretes specimens, which were subjected to static and fatigue tensile loadings. The microscopy results showed that the cyclic loading merely results in a few more microcracks than the static loading. This is probably due to the limited magnification of the microscope (15-30 $\times$ ) used in his study. Instead, Shah and Chandra [52] observed a significant increase in microcracking by using a microscope with a higher magnification (200 $\times$ ). There were nearly three times as many microcracks compared to those created by the static loading with the same stress. Moreover, they also found that microcracking under cyclic compressive loading consisted of extensive branching in the paste matrix plus a substantial amount of cracking at the aggregate-paste interface. Similarly, Toumi et al. [53] observed a higher number of interface cracks using a SEM technique. More diffuse microcracks in the matrix were also detected compared to the static crack pattern. When plotting the measured crack length versus the number of cycles, a steady stage with a constant crack growth rate depending on the upper loading level can be identified. This stage

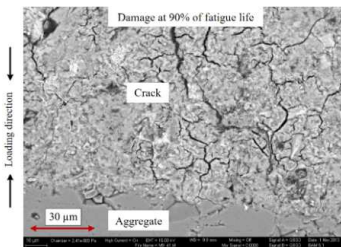
corresponds to the phase II in Figure 2-5. In addition, a new fatigue fracture mechanism was observed by Li et al. [54], who conducted a SEM analysis on fibre-reinforced concretes subjected to compressive fatigue loading. A clear trace of 'friction' was observed in the fatigue failure surface. The authors speculated that this may be caused by the crushing and friction process occurring between crack surfaces and fibres.

By using fluorescent microscopy and SEM, Thiele [55] examined the damage in concrete at three stages of fatigue. Examples of obtained microscopy and SEM images of the crack pattern in damaged concrete are shown in Figure 2-1. It was found that both the crack length and crack width increase dramatically before fatigue failure. Nevertheless, the changes in the crack pattern are insignificant in both phase I and phase II indicated in Figure 2-5. The author further assumed that damage also occurs on a smaller scale than considered in their research (presumably smaller than  $1\ \mu\text{m}$ ). Similar findings have also been reported in [11,56]. In addition, it was also noted by the author that even before unloading of the sample, the microstructure of the sample shows a pronounced pattern of cracks, which is likely due to the shrinkage during hydration. Moreover, owing to the destructive nature of microscopy investigations, it is not possible to follow up further development of crack patterns that had been identified in previous loading cycles.

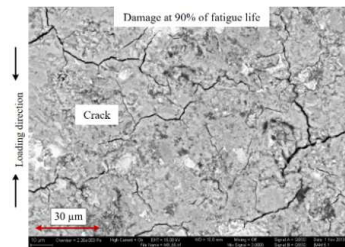
In a recent work performed by Schaan et al. [57], the transmission electron microscopy (TEM), combined with a focused ion beam (FIB) sample preparation, were employed to investigate the compressive fatigue damage in Ultra-High Performance Concrete (UHPC). At the early stage of fatigue loading, several needle-shaped regions have formed with a length of 150 – 250 nm and a width of 20 – 35 nm in the bulk matrix, as is shown in Figure 2-2. Meanwhile, the C-S-H compounds become denser during the fatigue process. Other components of the material, such as aggregate or unhydrated cement clinker, and silica fume particles, remain unaffected. These needle-shaped structural regions, which are initially believed to be the precursors of nanocracks, continuously grow in number and increasingly deplete with surrounding C-S-H as fatigue progresses. However, upon further investigation with the energy-dispersive X-ray spectroscopy (EDS) technique [58], the author concluded that these regions are related to locations where formation of ettringite occurs. It was argued that, since ettringite can readily recrystallize upon changes in environmental parameters, a recurring dissolution and crystallization can exert pressure on the surrounding material, leading to solidification and, eventually, the formation of nanocracks [58]. However, as yet very limited information regarding fatigue fracture behaviour at the nanoscale is available in literature.



(a) Microscope image of microcracks



(b) SEM image of the crack pattern near an aggregate



(c) SEM image of the crack pattern in paste matrix

Figure 2-1: (a) A microscope image of microcracks oriented parallel to the load direction with crack widths in a longitudinal section of a specimen that has been damaged for up to 90% of the fatigue life; (b) SEM image of the crack pattern near an aggregate; (c) SEM image of the crack pattern in paste matrix. Adapted from [55]

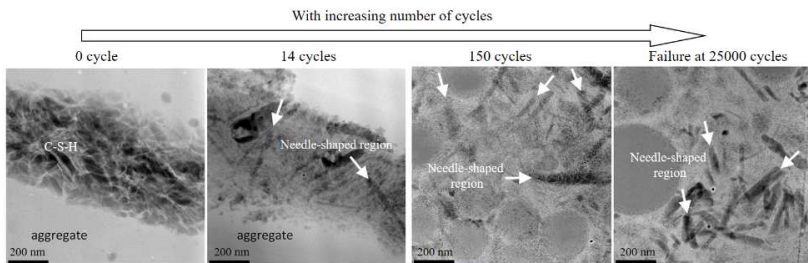


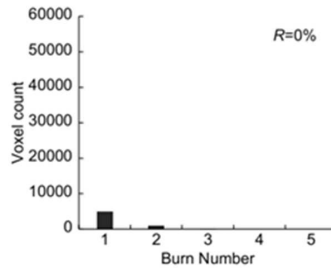
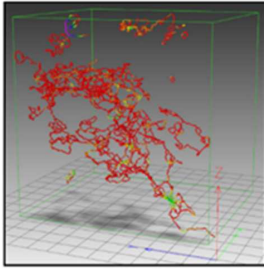
Figure 2-2: High-angle annular dark field STEM images of UHPC cement paste under the compressive fatigue loading adapted from [57]

### 3D X-RAY COMPUTED TOMOGRAPHY

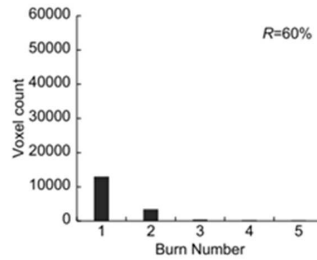
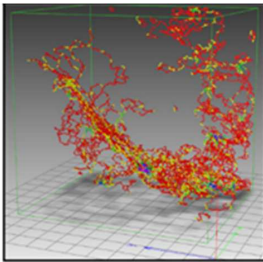
For traditional microscopy observations of fatigue damage, the tests have to be stopped and the specimens need to be cut in order to prepare the samples for the investigations. Moreover, the preparation of the samples may introduce some unwanted damage, which damage is difficult to distinguish from fatigue cracks. Therefore, the non-destructive X-ray computed tomography (XCT) technique seems to be a good alternative. The XCT technique has been widely used to characterise the internal microstructure of materials, due to its non-destructive nature and ability to track and visualize 3D details of the microstructure, including different phases, interfaces, pores and cracks [59,60]. Recently, several studies have employed the XCT technique to investigate the fatigue damage evolution in concrete. Sharma et al. [61] performed in-situ XCT tests on concrete specimens subjected to compressive cyclic loadings. The local fracture mechanisms, such as the crack opening and closing, crack tip extension and diversion and crack tip blunting were observed in the XCT images at different cycles. It was also revealed that there are many microcracks generated before the occurrence of macrocracks. Obara et al. [62] proposed a new method to estimate the damage using the XCT technique. In their work, the Three Dimensional Medial Axis Analysis (3DMA) was employed to analyze the damage evolution in concrete specimens subjected to a cyclic loading. The cyclic loading is programmed as variable amplitude loading with step-wise increase in the maximum load. The burn number and medial axis of the parameters in the 3DMA were used to evaluate the width and length of cracks, respectively. Generally, the larger values of these parameters represent a higher degree of damage. The obtained damage distributions in concrete specimens with different stress levels are shown in Figure 2-3, indicating a damage localization phenomenon. It was concluded that the XCT with 3DMA method is useful to evaluate damage in a specimen while under loading. However, only cracks with a width of more than 50  $\mu\text{m}$  could be detected reliably by XCT.

Fan and Sun [63] also applied the XCT technique with a spatial resolution of 1  $\mu\text{m}^3/\text{voxel}$  to investigate compressive fatigue damage evolution in cylindrical concrete specimens of 50 mm in diameter and 100 mm in height. The fatigue crack at different stages can be clearly visualized, as shown in Figure 2-4(a). The observed fatigue crack expanded with the increasing number of cycles, and the crack width was in the range of 0.6-1.7 mm at 90% of the fatigue life. The change of porosity of the specimen was also determined based on XCT images and used as an indicator to describe the degree of damage, see Figure 2-4(b). It was found that the porosity gradually increased and reached a value of 20% at 90% of the fatigue life. However, it should be noted that the resolutions of most commercially available XCT instruments are often not sufficient to detect extremely small fatigue-induced damage. Therefore, the XCT can only detect relatively wide cracks shortly before fatigue failure [11,56].

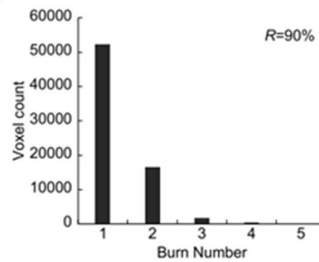
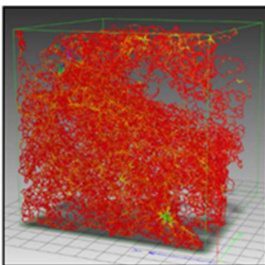




(a) At stress level of 0%

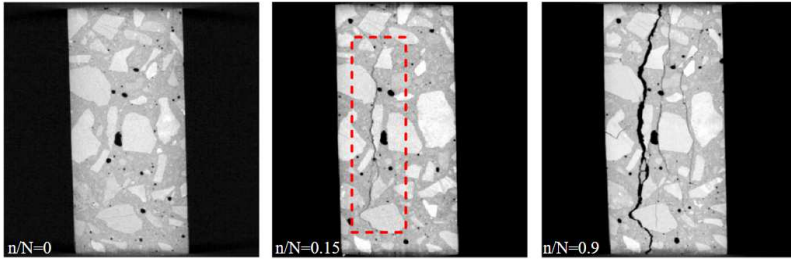


(b) At stress level of 60%

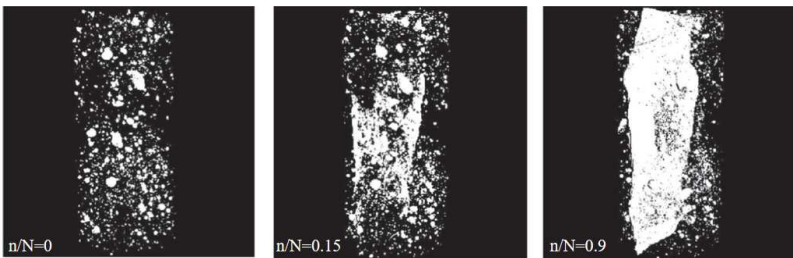


(c) At stress level of 90%

Figure 2-3: The distribution of medial axis (the warm color is a small burn number and the cold color represents a large burn number; the red color represents burn number 1) and the amount of burn number in cubic concrete specimens ( $10 \times 10 \times 10$  mm<sup>3</sup>) under the stress level of (a) 0%, (b) 60% and (c) 90% adapted from [62]



(a) The evolution of fatigue crack



(b) The evolution of detected pores

Figure 2-4: The ICT images for (a) the fatigue damage evolution in concrete specimens with the size of 50 mm in diameter and 100 mm in height under compressive fatigue loading and (b) the distribution of detected pores under the stress level of 80% adapted from [63]

### 2.3.2 INDIRECT APPROACH OF DAMAGE CHARACTERISATION

#### STIFFNESS DEGRADATION

In addition to direct observations, fatigue damage evolution in cementitious material can also be evaluated by using indirect approaches. In general, the initiation and propagation of cracks causes a continuous decrease in stiffness. Since the stiffness can easily be derived from the stress-strain curves, many researchers have used the change of stiffness as an indicator for fatigue damage [19,23,27,64,65]. It was found that the evolution of global stiffness under fatigue loading exhibits an 'S' shaped curve, which can be divided into three stages: the first stage is a rapid drop of stiffness; the second stage is characterised by a steady and slow decrease of stiffness and the third stage corresponds to a dramatic decline of stiffness. Kolluru et al. [65] found that the measured crack growth during fatigue loading shows a trend similar to the change in

stiffness. The degradation rate of stiffness largely depends on the loading frequency and maximum stress level [27,66]. However, this macroscopic damage indicator can only provide a global trend for the damage evolution.

#### ACOUSTIC EMISSION TECHNIQUE

To obtain additional information regarding the damage propagation inside the specimen, several researchers have applied the acoustic emission (AE) technique to evaluate the fatigue crack growth in concrete [56,67–69]. This non-destructive technique also enables real-time monitoring of microscopic processes as well as crack propagation inside the concrete. Different AE parameters, such as the amplitude, energy, count and duration, are often considered in terms of their quantitative distribution to detect the degree of generated damage and crack distribution [67,68]. Recently, Oneschkow et al. [69] investigated the fatigue behaviour of mortar and concrete samples using the AE technique. A higher AE activity was observed for concrete compared to mortar due to the presence of coarse aggregate. Moreover, a gradually increasing AE activity in the concrete was observed at the lower stress level, which cannot be reflected by the change of specimen stiffness. This indicated a damage process at very small scales (perhaps on a sub-microscale) during the fatigue process.

#### ELECTRICAL RESISTIVITY MEASUREMENT

Cao and Chung [70] attempted to detect minor fatigue damage by measuring the electrical resistivity of mortar specimens. It was found that the baseline resistivity irreversibly increased as cycling progressed due to damage generation (i.e., microcracking), which was most significant in the first few cycles, and diminished as cycling progressed. Later, a follow-up study on concrete fatigue conducted by the authors [71] showed that the measured resistivity decreased during the loading stage of the compressive fatigue cycle due to defect diminution (i.e., closing of microcracks). It then increased during the unloading stage due to the defect extension (i.e., propagation or enlargement of microcracks). Moreover, a comparison between results of cement paste and mortar samples showed that the interface between the paste and aggregate contributed to the defect diminution effect. As an alternative option to monitor the real-time damage accumulation non-destructively, the electrical resistivity measurement provides some new insights into the fatigue damage evolution in concrete.

#### PORE STRUCTURE CHANGES

A study of Zhang [12] demonstrates that several characteristics of the pore structure, such as the porosity and specific surface area, can be used as micro- or mesoscopic indicators to evaluate the macroscopic damage of concrete under fatigue

loading. The testing results based on mercury intrusion porosimetry (MIP), helium pycnometry and nitrogen adsorption methods showed that, under flexural fatigue loading, the magnitudes of all these indicators increased almost linearly with the increasing number of cycles. Both porosity in mortar (mainly macro pores) and interface between mortar and coarse aggregates (interfacial cracks) developed at a similar rate. The experimental results also showed good correlations between macroscopic mechanical properties (e.g., residual bending strength and Young's modulus) and micro- or mesoscopic parameters (porosity and mean pore size distribution). By using the MIP, Schaan et al. [57] also observed an increase of pore volume in the 30 – 500 nm pore radius range in cement paste specimen due to fatigue loading. Similar findings have also been reported Shen et al. in [72]. However, a continuous and accurate characterisation of the pore structure subjected to fatigue loadings is still a challenging task. Instead of direct examination of the pore structure, the fatigue damage evolution may also be reflected by the variation of transport properties. Fu et al. [73] investigated the chloride penetration in fatigue-damaged concrete with various loading levels. A quantitative correlation between the residual strain and the apparent chloride diffusivity of fatigue-damaged concrete has been established. In general, the chloride diffusivity increases with fatigue damage. It was found that when the maximum fatigue load is greater than 30-35% of the ultimate tensile load, the chloride penetration dramatically increased, suggesting that a substantial damage had been generated. Similarly, Desmettre and Charron [44] examined the real time variations of water permeability of normal-strength concrete and fibre-reinforced concrete under cyclic loading. It was found that the addition of fibres could arrest the fatigue crack growth as indicated by the smaller growth of water permeability compared to that in normal-strength concrete. However, due to the presence of water in the specimens in these tests, the transport properties may be affected by the self-healing process and, therefore, may not be a precise indicator for the fatigue damage.

### 2.3.3 GENERAL REMARKS

Many macroscopic fatigue damage indicators have been proposed to monitor the global fatigue damage evolution of concrete under the cyclic loading. It is clear that fatigue damage occurs at the macroscopic level in the form of stable crack growth. Recent applications of XCT offer an opportunity to continuously evaluate the fatigue damage evolution at lower scales and demonstrate the influence of mesoscopic features. However, less is known at the nano- and microscopic levels where the accumulations of fatigue damage in different components, and how they contribute to the global damage remains largely a matter of conjecture. Therefore, more advanced techniques may be needed to characterise the fatigue behaviour at these scales.

## 2.4 MODELS AND THEORIES FOR FATIGUE ANALYSIS

Besides experimental investigations, many models and theories have been developed over the past decades to predict and simulate the fatigue behaviour of cementitious materials. A review on the existing fatigue models is given in the following sections.

### 2.4.1 WÖHLER CURVE

Fatigue of materials is commonly characterised by an  $S-N$  curve (stress level versus fatigue life), also known as the Wöhler curve [74]. The stress level is generally calculated by dividing the maximum fatigue stress by the static strength of an identical specimen. If  $N$  is plotted on a logarithmic scale and  $S$  on a linear scale, the  $S-N$  curve will become approximately a straight line. To consider the effect of minimum fatigue stress on the fatigue life, Aas-Jakobsen [75] proposed a modified  $S-N$  relationship incorporating the stress ratio  $R$  (the ratio of minimum fatigue stress to the maximum fatigue stress), which is based on the observed linear relationship between  $S$  and  $R$ . Moreover, due to the significant scatter in fatigue life data, a family of  $S-N$  curves with a certain probability of failure, known as  $S-N-P$  plots, is also used [76,77]. The  $S-N$  curve is found to be largely affected by the mix composition of concrete and also the loading history. Generally, considerable experimental data is required to draw the  $S-N$  curves. These experimentally obtained  $S-N$  curves are widely adopted and remain the primary design tool for predicting the fatigue life of concrete structures. However, the major drawback of the  $S-N$  method is that it is purely phenomenological, without any information regarding the physical processes in the microstructure. The lack of generality of this method limits its application for different concrete mixtures. Moreover, it has been recognised that designers should not only know when fatigue failure occurs, but also how much damage has been accumulated during the structure's service life [78]. Therefore, researchers tend to accomplish a more ambitious goal, i.e., to predict, or to at least understand, the fatigue damage evolution or propagation of cracks at lower scales rather than just observing the macroscopic results.

### 2.4.2 PARIS' LAW

Thanks to the advent of fracture mechanics, designers and engineers are able to investigate the fatigue phenomenon on a theoretical basis [79,80]. Since the fatigue of material involves initiation and propagation of microcracks, fracture mechanics is found to be a useful tool for studying the fatigue fracture process. In general, there are three stages for the fatigue fracture process [34,55], as shown in Figure 2-5. The first stage is the crack initiation stage. The initiation of a crack is always associated with stress concentrations, which may be due to flaws, surface discontinuities or pre-existing

cracks. The crack initiation process in concrete can be ignored as there is already a large number of pre-existing cracks in the material even prior to any loading. The second stage is the stable crack propagation stage, which is characterised by slow and progressive growth of multiple cracks to a critical size. At this stage, the residual strain of concrete increases with an almost constant rate. Meanwhile, multiple cracks gradually propagate in the concrete with the increasing number of cycles, resulting in a decrease of stiffness. This is followed by the final stage of rapid crack growth. In the final stage of concrete fatigue, when a sufficient number of cracks have propagated and coalesced, a continuous macrocrack is formed, eventually leading to the failure.

Most studies into the fatigue phenomenon focus on the crack propagation stage as it generally accounts for the largest portion of the fatigue life [79,81,82]. According to experimental observations on metallic materials, Paris and Erdogan [81] proposed a law to describe the fatigue crack growth rate by relating it to the amplitude of the stress intensity factor range  $\Delta K$ :

$$\frac{da}{dN} = C(\Delta K)^m \quad (2-2)$$

where  $C$  and  $m$  are experimentally obtained constants dependent on the material,  $da/dN$  is the crack growth per cycle. Meanwhile, the Paris' law is well-known and its modifications have gained wide acceptance for the application in metals. The first study attempting to apply the Paris' law for concrete was conducted by Baluch et al. [83]. Following their study, many numerical and analytical models based on the Paris' law have been developed to predict the fatigue life of concrete [84–86].

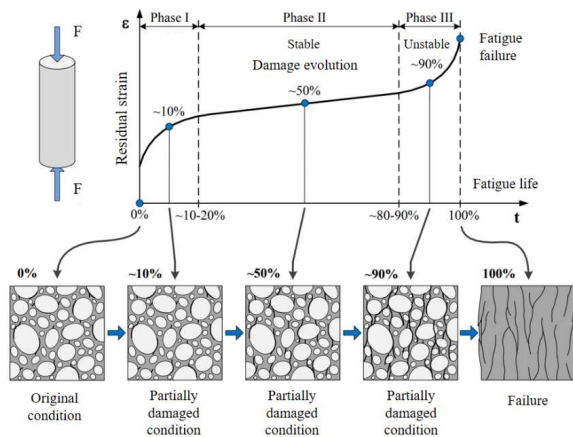


Figure 2-5: Illustration of the fatigue damage evolution under compressive fatigue loading adapted from [55]

In addition, several attempts have been made to modify the original Paris' law in order to improve the prediction accuracy. For instance, Bažant and Xu [80] proposed a size-adjusted Paris' law to consider the size effect of fracture in concrete specimens. The effect of variable amplitude cyclic loading was also included in the Paris' law by Slowik et al. [87]. In a recent theoretical study by Le and Bažant [88], the Paris' law was physically justified for brittle and quasi-brittle materials based on atomic fracture mechanics and an energetic analysis, which relates the fatigue kinetics of a macrocrack to the growth rate of nanocracks. This law was then used to relate the probability distribution of critical stress amplitude to the probability distribution of fatigue lifetime. It was found that the proposed theoretical model yields a power-law relation for the  $S$ - $N$  curve. In their work, the propagation of a nanocrack is assumed to be the result of the fracture between nanoscale elements [89]. Such nanoscale elements can be either an atomic lattice block representing a crystal grain of brittle ceramic, see Figure 2-6(a), or a completely disordered system of nanoparticles of the calcium silicate hydrate (C-S-H) in concrete, see Figure 2-6(b). For more details regarding the physical explanations and formulations of the nanoscale crack propagation under the cyclic loading, the reader is referred to [88–90].

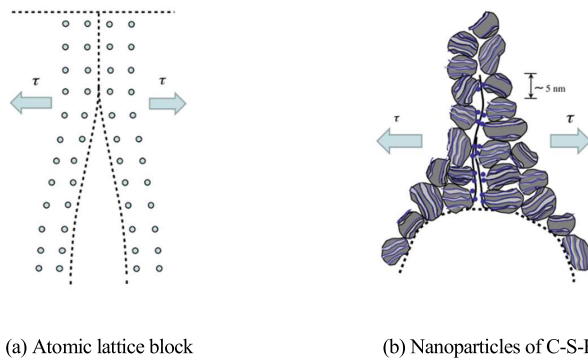


Figure 2-6: The assumed fracture of the nanoscale element for (a) an atomic lattice block; (b) a disordered system of nanoparticles of the calcium silicate hydrate adapted from [88]

However, it is known that in front of the crack tip in concrete there exists a so-called fracture process zone (FPZ), which is assumed to consist of many closely spaced microcracks [91,92]. This zone offers resistance to the crack growth owing to various toughening mechanisms, such as particle interlock, aggregate bridging, surface friction and crack branching, among others [93]. Due to the presence of a large fracture process zone, the Paris' law based on the linear elastic fracture mechanics may give erroneous results even with carefully modified versions [93,94]. Hence, for a better understanding

of the fatigue crack propagation phenomenon in concrete, the nonlinear behaviour in front of the crack tip needs to be properly described [95].

### 2.4.3 COHESIVE ZONE MODEL

In the work of Hillerborg et al. [96], a non-linear fracture mechanics model has been proposed to simulate the complex tensile fracture behaviour in concrete under monotonic loading conditions. In this model, the fracture process zone is modelled as a fictitious crack that can transfer cohesive stresses, as is shown in Figure 2-7(a). In reality, this cohesive crack corresponds to the diffused microcracking zone in concrete with some remaining ligaments that allow the stress transfer. The maximum cohesive stress that can be transmitted is assumed to be a decreasing function of the crack-opening displacement [96]. Note that for simplicity the linear or bilinear softening curve is often assumed [97,98]. Therefore, the crack growth can be readily simulated as a consequence of continuous de-bonding of the fracture process zone [98–100]. Moreover, the energy balance can also be considered in the model. As is depicted in Figure 2-7(b), the amount of energy absorbed per unit crack area in widening the crack from zero to  $\omega_1$  can be calculated as the area between the curve and the coordinate axes. The proposed cohesive crack model is found to yield realistic results regarding the crack formation and propagation under the monotonic loading [96].

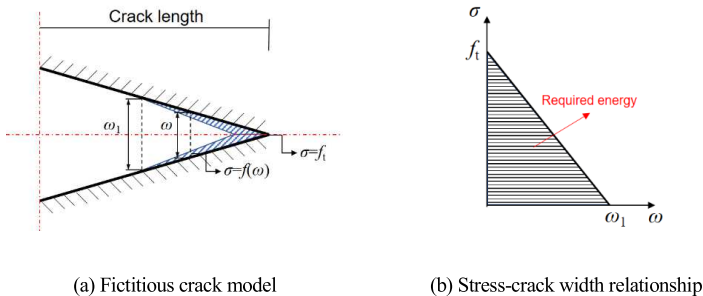


Figure 2-7: The fictitious crack model adapted from [96] (a) the assumed stress distribution near the crack; (b) the assumed linear relationship between the stress and the crack opening displacement

Due to its success in monotonic fracture cases, the principle of the cohesive zone model was then applied for simulating the fatigue fracture of concrete [101–104]. Based on Hillerborg's model, an extended version considering the cyclic loading conditions was proposed by Gylltoft [105]. By introducing a cyclic softening stress-strain relationship, the model is able to describe the progressive tensile fatigue failure of concrete. Afterwards, many attempts have been made to modify the shape of the cyclic



softening curve [101–103]. Among them, Hordijk [102] proposed the continuous function model (CFM), which provides an accurate approximation of the complete unloading–reloading cycle, see Figure 2-8. Based on a close inspection of experimental results, four analytical expressions were used for the CFM and each of them represents a certain stage of the cyclic constitutive law, i.e., (I) the post-peak envelop curve, (II) the unloading curve, (III) the gap on the envelop curve and (IV) the reloading curve. Hordijk [102] found that after one unloading–reloading cycle, the intersection point between the reloading curve and the envelop curve will not be the original unloading point. This deviation ( $\omega_{inc}$ ) is thought to be caused by the material degradation during the loading cycle and can be determined using the following expression:

$$\frac{\omega_{inc}}{\omega_c} = 0.1 \left( \frac{\omega_{eu}}{\omega_c} \right) \left\{ \ln \left( 1 + 3 \frac{\sigma_{eu} - \sigma_L}{f_t} \right) \right\} \quad (2-3)$$

where  $f_t$  is the tensile strength of concrete. Other parameters can be found in Figure 2-8. An appealing feature of this approach is that the analytical expression can be easily implemented as a mathematical subroutine in numerical simulations. This provides new solutions to simulate the complex fatigue fracture behaviour of concrete.

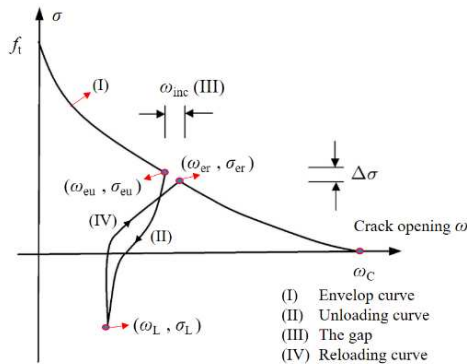
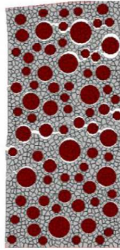


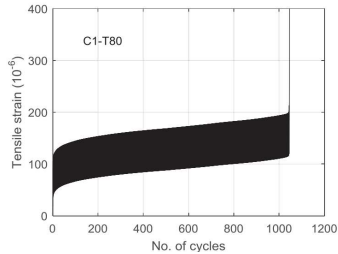
Figure 2-8: The description of continuous function model adapted from [102]

However, most cohesive crack models focus on describing the behaviour of a single macroscopic crack in concrete. Only until recently, Gong et al. [106] developed a mesoscopic fatigue model based on the Rigid Body Spring Method (RBSM). The constitutive laws used for the cyclic loading, which are similar to the principle of cohesive zone model, were developed at normal and shear directions for the mortar and interfacial transition zone (ITZ). The fracture pattern and the strain history under tensile fatigue loading can be obtained by this model, as shown in Figure 2-9. A good agreement was found between the simulation results and experimental data, in terms

of  $S-N$  curve and strain history. But still, the knowledge regarding the fatigue fracture mechanisms at lower scales and the effects of microstructural features on the growth of multiple cracks is rather limited. Therefore, more efforts are still needed with respect to the multiscale investigation of concrete fatigue.



(a) Tensile fatigue fracture pattern



(b) Strain history in fatigue simulation

Figure 2-9: The numerical results of mesoscopic model based on RBSM for tensile fatigue adapted from [106]; (a) an example of the tensile fatigue fracture pattern (red particles represent aggregate and grey for mortar) (b) the strain history in fatigue simulation under 80% of tensile strength

#### 2.4.4 DAMAGE MECHANICS

An alternative method to consider the fatigue damage evolution in concrete is the damage mechanics. Damage mechanics has been extensively used to model the progressive degradation of mechanical properties of materials caused by the propagation and coalescence of microcracks, microvoids and similar defects [107–109]. In this approach, damage variables need to be introduced to describe the degree of deterioration of the material. Afterwards, constitutive equations of damage evolution for these variables are formulated in the framework of thermodynamics [108]. These equations are calibrated and validated with experimental data to model different damage processes [110–113]. It is known that the concrete subjected to fatigue loadings will experience gradual accumulation of damage in terms of the microcracking, which manifests itself in the degradation of mechanical properties such as stiffness. Therefore, the damage mechanics approach may be suitable for describing the fatigue behaviour of concrete. Over past decades, many phenomenological macroscopic damage models have been developed [113–117]. Suaris et al. [113] proposed a stress-based damage model for monotonic and cyclic behaviour of concrete. The damage evolution law was obtained using an approach similar to the bounding surface plasticity theory [118]. The macroscopic behaviour of concrete under compression, tension and cyclic loading can be well predicted by this model. By combining the concepts of damage mechanics and fracture mechanic, Fathima and Kishen [116] proposed a damage model

for the case of constant amplitude cyclic loading. In their work the damage evolution law was proposed through a closed form expression for dual dissipation potential, which was derived using the principles of thermodynamics and dimensional analysis. Progressive stiffness reduction due to the fatigue loading can be captured by the model. The same authors further extended the analytical model to consider the variable amplitude cyclic loading in [48]. In the work of Liang et al. [119], the fatigue behaviour of large reinforced concrete structures was simulated by implementing the constitutive damage model into the finite element analysis. The damage distribution and the potential fatigue damage failure pattern of concrete structures can be reasonably predicted by the model.

In addition to the macroscopic models, a few mesoscopic fatigue damage models have been proposed recently [120–122]. Grassl and Rempling [120] developed a damage-plasticity interface constitutive model to describe the irreversible strain under the cyclic loading. This calibrated interface model was then inserted into the mesoscale simulation of concrete by considering an idealized heterogeneous mesostructure. It has been demonstrated that the typical hysteresis loops for cyclic loading and the macroscopic damage evolution can be modeled as a structural result of localized irreversible strains on the constitutive level. A different strategy to consider the fatigue damage evolution was proposed by Sun and Xu [121]. In their work a fatigue damage variable was established by homogenizing the collective effect of microscale cracks, while crack growth was determined based on the Paris' law. The mesoscopic heterogeneity of concrete was also introduced by introducing probability distributions to material properties. The effectiveness of the model was verified by comparing calculated results with experimental results.

Even though the macroscopic and mesoscopic damage phenomena of concrete can be predicted quite reliably with damage mechanics, the underlying physical origin of fatigue at the microscale is still not clear. Moreover, only very limited information regarding the damage evolution of basic constituents and their effects on the overall fatigue behaviour of concrete can be found in available literature.

#### **2.4.5 GENERAL REMARKS**

Various types of models have been developed to describe the macroscopic fatigue behaviour by establishing a law for propagation of local cracks. Several semi-empirical equations with some theoretical considerations [88,90] or purely phenomenological models [101–103] have been proposed. Both qualitative understanding and quantitative predictions of concrete fatigue can be obtained with these models. However, the complex microstructural mechanisms in concrete, e.g. material properties and material structures at different scales, have not been considered in these models yet. As a results, they may have less applicability once different material compositions are used. Furthermore, substantial experimental evidences have

confirmed that many microscopic (or mesoscopic) features of cementitious materials can significantly affect the macroscopic fatigue behaviour.

To efficiently cope with the multiscale nature of concrete, multiscale modelling schemes are often applied [123]. The aim of a multiscale model is to establish a relation between macroscopically observed phenomena and their lower-scale origin. When dealing with the multiscale heterogeneity of concrete, it is preferable to consider the material structures and local properties of basic components at different scales in the model in order to increase the prediction accuracy [124]. In recent decades, great progress has been made in multiscale modelling strategies of static fracture of concrete and examples of such models can be found in literature [123,125–127]. Despite the achievements in modelling static fracture, little work has been done to simulate the fatigue fracture behaviour of concrete in a multiscale manner. There are two main reasons for this. Firstly, it has been recognized that fatigue cracking behaviour is more complex than static fracture. Basic knowledge of static mechanical properties of concrete is an essential starting point for the analysis of more complex fatigue fracture [102]. Only the maturing and reliable multiscale modelling scheme for the static fracture analysis can be further extended to simulate fatigue behaviours. Therefore, most research efforts are initially devoted to this aspect [125,128]. Another reason is that the knowledge regarding the fatigue behaviour of cementitious materials at nano- and microscales is very limited. As suggested in previous sections, there is a technical challenge to experimentally characterise fatigue damage evolution at low scales. So far, most fatigue models only focus on the macroscopic or mesoscopic fatigue damage evolution, which is much easier to measure and compare. It is necessary, however, to develop more advanced techniques and appropriate multiscale modelling schemes to predict macroscopic fatigue properties of concrete.

## 2.5 CONCLUSION

Based on the presented state of the art on fatigue of concrete, the following conclusions can be drawn:

- (1) From past experimental work it can be learned that microstructural features of concrete can significantly affect its macroscopic fatigue behaviour. For a reliable and accurate prediction of concrete fatigue, it is essential to first improve the understanding of the fatigue behaviour of concrete and its constituents at different scales, and then to establish quantitative relationships between microscopic features and macroscopic fatigue performance.
- (2) Most literature studies focused on developing macroscopic indicators to describe the global fatigue damage evolution of concrete. However, the knowledge regarding the fatigue damage accumulation at lower scales is rather limited. Therefore, more advanced techniques are needed to characterise the fatigue properties at lower scales.

- (3) A brief review of existing fatigue models indicates that the complex microstructural effects on macroscopic fatigue of concrete have not been considered in these models. Even though multiscale modelling schemes provide a promising solution to cope with the multiscale nature of concrete, little work has been done on this aspect, mainly due to the limited knowledge of fatigue behaviour of concrete at lower scales. Therefore, more efforts are needed in the development of both experimental characterisation and multiscale modelling of concrete fatigue.

In the following chapters, a new experimental technique will be proposed and developed to characterise the fatigue behaviour of cementitious materials at the microscale. A multiscale modelling scheme will be proposed to link fatigue damage mechanisms of cementitious materials at the micro- and mesoscale.

## REFERENCES

- [1] S. Suresh, *Fatigue of materials*, Cambridge university press, 1998.
- [2] W. Schlitz, *A history of fatigue*, *Eng. Fract. Mech.* 54 (1996) 263–300.
- [3] J. Schijve, *Fatigue of structures and materials in the 20th century and the state of the art*, *Int. J. Fatigue.* 25 (2003) 679–702.
- [4] A. Wöhler, *Versuche zur Ermittlung der auf die Eisenbahnwagenachsen einwirkenden Kräfte und die Widerstandsfähigkeit der Wagen-Achsen*, *Zeitschrift Für Bauwes.* 10 (1860) 583–614.
- [5] A. Considère, *Influence des armatures métalliques sur les propriétés des mortiers et bétons*, Gauthier-Villars, 1899.
- [6] D. Joly, *La resistance et l'“elasticite des” ciments Portland*, *Ann Pons Chaussees.* 16 (1898) 198–244.
- [7] T.T.C. Hsu, *Fatigue of Plain Concrete*, *ACI J. Proc.* 78 (1981) 292–304.
- [8] T.T.C. Hsu, *Fatigue and microcracking of concrete*, *Matériaux Constr.* 17 (1984) 51–54.
- [9] L. Gao, C.T.T. Hsu, *Fatigue of concrete under uniaxial compression cyclic loading*, *ACI Mater. J.* 95 (1998) 575–581.
- [10] F.W. Klaiber, D.Y. Lee, *The effects of air content, water-cement ratio, and aggregate type on the flexural fatigue strength of plain concrete*, *Am. Concr. Institute, ACI Spec. Publ. SP-075* (1982) 111–131.
- [11] Y. Gan, H. Zhang, Y. Zhang, Y. Xu, E. Schlangen, K. van Breugel, B. Šavija, *Experimental study of flexural fatigue behaviour of cement paste at the microscale*, *Int. J. Fatigue.* 151 (2021).
- [12] B. Zhang, *Relationship between pore structure and mechanical properties of ordinary concrete under bending fatigue*, *Cem. Concr. Res.* 28 (1998) 699–711.
- [13] M.A. Vicente, D.C. González, J. Mínguez, M.A. Tarifa, G. Ruiz, R. Hindi, *Influence of the pore morphology of high strength concrete on its fatigue life*, *Int. J. Fatigue.* 112 (2018) 106–116.
- [14] E.W. Tse, D.Y. Lee, F.W. Klaiber, *Fatigue behavior of concrete containing fly ash*, *Spec. Publ. SP-091* (1986) 273–289.
- [15] L.P. Guo, W. Sun, K.R. Zheng, H.J. Chen, B. Liu, *Study on the flexural fatigue performance and fractal mechanism of concrete with high proportions of ground granulated blast-furnace slag*, *Cem. Concr. Res.* 37 (2007) 242–250.
- [16] X. Chen, L. Xu, J. Bu, *Dynamic tensile test of fly ash concrete under alternating tensile-compressive loading*, *Mater. Struct. Constr.* 51 (2018) 20.
- [17] S. Müller, V. Mechtcherine, *Fatigue behaviour of strain-hardening cement-based composites (SHCC)*, *Cem. Concr. Res.* 92 (2017) 75–83.
- [18] J. Qiu, E. Yang, *Micromechanics-based investigation of fatigue deterioration of engineered cementitious composite (ECC)*, *Cem. Concr. Res.* 95 (2017) 65–74.
- [19] S.J. Stephen, R. Gettu, *Fatigue fracture of fibre reinforced concrete in flexure*, *Mater. Struct. Constr.* 53 (2020) 1–11.
- [20] C.D. Johnston, R.W. Zemp, *Flexural fatigue performance of steel fiber reinforced concrete. Influence of fiber content, aspect ratio, and type*, *ACI Mater. J.* 88 (1991) 374–383.
- [21] M. Grzybowski, C. Meyer, *Damage accumulation in concrete with and without fiber reinforcement*, *ACI Mater. J.* 90 (1993).
- [22] K.M.A. Sohel, K. Al-Jabri, M.H. Zhang, J.Y.R. Liew, *Flexural fatigue behavior of ultra-lightweight cement composite and high strength lightweight aggregate concrete*, *Constr. Build. Mater.* 173 (2018) 90–100.

- [23] C. Thomas, I. Sosa, J. Setién, J.A. Polanco, A.I. Cimentada, Evaluation of the fatigue behavior of recycled aggregate concrete, *J. Clean. Prod.* 65 (2014) 397–405.
- [24] J. Ren, D. Li, Y. Xu, J. Huang, W. Liu, Fatigue behaviour of rock asphalt concrete considering moisture, high-temperature, and stress level, *Int. J. Pavement Eng.* 0 (2021) 1–11.
- [25] J.W. Galloway, H.M. Harding, K.D. Raithby, Effects of moisture changes on flexural and fatigue strength of concrete, 1979.
- [26] B.T. Huang, Q.H. Li, S.L. Xu, W. Liu, H.T. Wang, Fatigue deformation behavior and fiber failure mechanism of ultra-high toughness cementitious composites in compression, *Mater. Des.* 157 (2018) 457–468.
- [27] X. Chen, J. Bu, X. Fan, J. Lu, L. Xu, Effect of loading frequency and stress level on low cycle fatigue behavior of plain concrete in direct tension, *Constr. Build. Mater.* 133 (2017) 367–375.
- [28] B. Zhang, D. V. Phillips, K. Wu, Effects of loading frequency and stress reversal on fatigue life of plain concrete, *Mag. Concr. Res.* 48 (1996) 361–375.
- [29] H.K. Hilsdorf, C.E. Kesler, The behavior of concrete in flexure under varying repeated loads, Department of Theoretical and Applied Mechanics. College of Engineering ... , 1960.
- [30] R.B. Tait, Fatigue and fracture of cement mortar, (1984).
- [31] J.K. Kim, Y.Y. Kim, Experimental study of the fatigue behavior of high strength concrete, *Cem. Concr. Res.* 26 (1996) 1513–1523.
- [32] Z. Ding, D.C. Feng, X. Ren, J. Wang, Physically based constitutive modeling of concrete fatigue and practical numerical method for cyclic loading simulation, *Eng. Fail. Anal.* 101 (2019) 230–242.
- [33] S. Arora, S.P. Singh, Fatigue strength and failure probability of concrete made with RCA, *Mag. Concr. Res.* 69 (2017) 55–67.
- [34] M.K. Lee, B.I.G. Barr, An overview of the fatigue behaviour of plain and fibre reinforced concrete, *Cem. Concr. Compos.* 26 (2004) 299–305.
- [35] J.D. Antrim, A study of the mechanism of fatigue in cement paste and plain concrete, Purdue University, 1964.
- [36] Y. Gan, H. Zhang, B. Šavija, E. Schlangen, K. van Breugel, Static and fatigue tests on cementitious cantilever beams using nanoindenter, *Micromachines.* 9 (2018).
- [37] P. Lura, Autogenous deformation and internal curing of concrete, Delft University of Technology, PhD Thesis, 2003.
- [38] K. van Breugel, T.A. van Beek, Ageing of old and modern concrete structures- Observations and research, *Rev. ALCONPAT.* 7 (2017).
- [39] O. Graf, E. Brenner, Versuche zur Ermittlung der Widerstandsfähigkeit von Beton gegen oftmals wiederholte Druckbelastung, *Mitteilungen Der Dtsch. Mater.* (1940) 416.
- [40] J.W. Murdock, A critical review of research on fatigue of plain concrete, *Univ. Illinois Eng. Exp. Stn. Bull.* (1965) 25.
- [41] P.R. Sparks, J.B. Menzies, The effect of rate of loading upon the static and fatigue strengths of plain concrete in compression, *Mag. Concr. Res.* 25 (1973) 73–80.
- [42] Y. Gan, C.R. Rodriguez, E. Schlangen, K. van Breugel, B. Šavija, Assessing strain rate sensitivity of cement paste at the micro-scale through micro-cantilever testing, *Cem. Concr. Compos.* 121 (2021).
- [43] K.D. Raithby, J.W. Galloway, Effects of moisture condition, age, and rate of loading on fatigue of plain concrete, *Spec. Publ. SP-041* (1974) 15–34.
- [44] C. Desmetre, J.P. Charron, Water permeability of reinforced concrete subjected to cyclic tensile loading, *ACI Mater. J.* 110 (2013) 79–88.

- [45] H.A.W. Cornelissen, H.W. Reinhardt, Uniaxial tensile fatigue failure of concrete under constant-amplitude and programme loading, *Mag. Concr. Res.* 36 (1984) 216–226.
- [46] B.H. Oh, Cumulative Damage Theory of Concrete under Variable-Amplitude Fatigue Loadings, *ACI Mater. J.* 88 (1991) 41–48.
- [47] A.J.M. Slemes, Miner's rule with respect to plain concrete variable amplitude tests, *Spec. Publ. SP-075* (1982) 343–372.
- [48] K. Keerthana, J.M. Chandra Kishen, An experimental and analytical study on fatigue damage in concrete under variable amplitude loading, *Int. J. Fatigue.* 111 (2018) 278–288.
- [49] M.A. Miner, Cumulative damage in fatigue, (1945).
- [50] J.O. Holmen, Fatigue of Concrete by Constant and Variable Amplitude Loading, *ACI Spec. Publ.* 75 (1982) 71–110.
- [51] M. Saito, Characteristics of microcracking in concrete under static and repeated tensile loading, *Cem. Concr. Res.* 17 (1987) 211–218.
- [52] Surendra P. Shah, Sushil Chandra, Fracture of Concrete Subjected To Cyclic and Sustained Loading, *J Amer Concr. Inst.* 67 (1970) 816–827.
- [53] A. Toumi, A. Bascoul, A. Turatsinze, Crack propagation in concrete subjected to flexural- cyclic loading, *Mater. Struct.* 31 (1998) 451–458.
- [54] Q. Li, B. Huang, S. Xu, B. Zhou, R.C. Yu, Compressive fatigue damage and failure mechanism of fiber reinforced cementitious material with high ductility, *Cem. Concr. Res.* 90 (2016) 174–183.
- [55] M. Thiele, Experimentelle Untersuchung und Analyse der Schädigungsevolution in Beton unter hochzyklischen Ermüdungsbeanspruchungen, Bundesanstalt für Materialforschung und-prüfung (BAM), 2016.
- [56] N. Oneschkow, T. Scheiden, M. Hüpgen, C. Rozanski, M. Haist, Fatigue-induced damage in high-strength concrete microstructure, *Materials (Basel).* 14 (2021).
- [57] G. Schaan, S. Rybczynski, F. Schmidt-Döhl, M. Ritter, Fatigue of concrete examined on the nanoscale, *TEM Stud. Fatigue-Induced Chang. Cem. Paste UHPC. Imag. Microsc.* 2 (2020) 25–27.
- [58] S. Rybczynski, G. Schaan, M. Dosta, M. Ritter, F. Schmidt-Döhl, Discrete element modeling and electron microscopy investigation of fatigue-induced microstructural changes in ultra-high-performance concrete, *Materials (Basel).* 14 (2021).
- [59] S. Brisard, M. Serdar, P.J.M. Monteiro, Multiscale X-ray tomography of cementitious materials: A review, *Cem. Concr. Res.* 128 (2020).
- [60] Z. Yang, W. Ren, R. Sharma, S. McDonald, M. Mostafavi, Y. Vertyagina, T.J. Marrow, In-situ X-ray computed tomography characterisation of 3D fracture evolution and image-based numerical homogenisation of concrete, *Cem. Concr. Compos.* 75 (2017) 74–83.
- [61] R. Sharma, W. Ren, S. McDonald, Z. Yang, Micro-mechanisms of concrete failure under cyclic compression: X-ray tomographic in-situ observations, *Proc. 9th Int. Conf. Fract. Mech. Concr. Concr. Struct.* (2016).
- [62] Y. Obara, I. Tanikura, J. Jung, R. Shintani, S. Watanabe, Evaluation of Micro-damage of Concrete Specimens under Cyclic Uniaxial Loading by X-ray CT Method, *J. Adv. Concr. Technol.* 14 (2016) 433–443.
- [63] Z. Fan, Y. Sun, Detecting and evaluation of fatigue damage in concrete with industrial computed tomography technology, *Constr. Build. Mater.* 223 (2019) 794–805.
- [64] N. Oneschkow, Fatigue behaviour of high-strength concrete with respect to strain and stiffness, *Int. J. Fatigue.* 87 (2016) 38–49.
- [65] S. V. Kolluru, E.F. O'Neil, J.S. Popovics, S.P. Shah, Crack Propagation in Flexural



- Fatigue of Concrete, *J. Eng. Mech.* 126 (2000) 891–898.
- [66] B. Isojeh, M. El-Zeghayar, F.J. Vecchio, Concrete Damage under Fatigue Loading in Uniaxial Compression, *ACI Mater. J.* 114 (2017).
- [67] M.N. Noorsuhada, An overview on fatigue damage assessment of reinforced concrete structures with the aid of acoustic emission technique, *Constr. Build. Mater.* 112 (2016) 424–439.
- [68] S.G. Shah, J.M. Chandra Kishen, Use of acoustic emissions in flexural fatigue crack growth studies on concrete, *Eng. Fract. Mech.* 87 (2012) 36–47.
- [69] N. Oneschkow, T. Timmermann, S. Löhnert, Compressive Fatigue Behaviour of High-Strength Concrete and Mortar: Experimental Investigations and Computational Modelling, *Materials* (Basel), 15 (2022).
- [70] J. Cao, D.D.L. Chung, Minor damage of cement mortar during cyclic compression monitored by electrical resistivity measurement, *Cem. Concr. Res.* 31 (2001) 1519–1521.
- [71] J. Cao, D.D.L. Chung, Defect dynamics and damage of concrete under repeated compression, studied by electrical resistance measurement, *Cem. Concr. Res.* 31 (2001) 1639–1642.
- [72] A. Shen, S. Lin, Y. Guo, T. He, Z. Lyu, Relationship between flexural strength and pore structure of pavement concrete under fatigue loads and Freeze-thaw interaction in seasonal frozen regions, *Constr. Build. Mater.* 174 (2018) 684–692.
- [73] C. Fu, H. Ye, X. Jin, D. Yan, N. Jin, Z. Peng, Chloride penetration into concrete damaged by uniaxial tensile fatigue loading, *Constr. Build. Mater.* 125 (2016) 714–723.
- [74] W. Schütz, A history of fatigue, *Eng. Fract. Mech.* 54 (1996) 263–300.
- [75] K. Aas-Jakobsen, Fatigue of concrete beams and columns, Division of Concrete Structures, Norwegian Inst. of Technology, University, 1970.
- [76] J.T. McCall, Probability of fatigue failure of plain concrete, in: *J. Proc.*, 1958: pp. 233–244.
- [77] M. Do, O. Chaallal, P. Aïtcin, Fatigue Behavior of High-Performance Concrete, *J. Mater. Civ. Eng.* 5 (1993) 96–111.
- [78] K. Matsumoto, Y. Sato, T. Ueda, L. Wang, Mesoscopic analysis of mortar under high-stress creep and low-cycle fatigue loading, *J. Adv. Concr. Technol.* 6 (2008) 337–352.
- [79] J.L. Le, J. Manning, J.F. Labuz, Scaling of fatigue crack growth in rock, *Int. J. Rock Mech. Min. Sci.* 72 (2014) 71–79.
- [80] Z.P. Bazant, K. Xu, Size effect in fatigue fracture of concrete, *ACI Mater. J.* 88 (1991) 390–399.
- [81] P. Paris, F. Erdogan, A critical analysis of crack propagation laws, *J. Basic Eng.* 85 (1963) 528–533.
- [82] Z.P. Bazant, M.H. Hübner, Theory of cyclic creep of concrete based on Paris law for fatigue growth of subcritical microcracks, *J. Mech. Phys. Solids.* 63 (2014) 187–200.
- [83] M.H. Baluch, A.B. Qureshy, A.K. Azad, Fatigue crack propagation in plain concrete, in: *Fract. Concr. Rock*, Springer, 1989: pp. 80–87.
- [84] K. Kirane, Z.P. Bazant, Size effect in Paris law and fatigue lifetimes for quasibrittle materials: Modified theory, experiments and micro-modeling, *Int. J. Fatigue.* 83 (2016) 209–220.
- [85] T. Sain, J.M. Chandra Kishen, Damage indices for failure of concrete beams under fatigue, *Eng. Fract. Mech.* 75 (2008) 4036–4051.
- [86] A. Mohammadipour, K. Willam, A numerical lattice method to characterize a contact fatigue crack growth and its Paris coefficients using configurational forces and stress-life curves, *Comput. Methods Appl. Mech. Eng.* 340 (2018) 236–252.
- [87] V. Slowik, G.A. Plizzari, V.E. Saouma, Fracture of concrete under variable amplitude

- fatigue loading, *ACI Mater. J.* 93 (1996) 272–283.
- [88] J.-L. Le, Z.P. Bažant, Unified nano-mechanics based probabilistic theory of quasibrittle and brittle structures: II. Fatigue crack growth, lifetime and scaling, *J. Mech. Phys. Solids*. 59 (2011) 1322–1337.
- [89] J.-L. Le, Z.P. Bažant, M.Z. Bazant, Unified nano-mechanics based probabilistic theory of quasibrittle and brittle structures: I. Strength, static crack growth, lifetime and scaling, *J. Mech. Phys. Solids*. 59 (2011) 1291–1321.
- [90] D. Zhaodong, L. Jie, A physically motivated model for fatigue damage of concrete, *Int. J. Damage Mechanics*. 27 (2018) 1192–1212.
- [91] J.G.M. Van Mier, *Concrete fracture: a multiscale approach*, CRC press, 2012.
- [92] Z.P. Bažant, *Concrete fracture models: Testing and practice*, *Eng. Fract. Mech.* 69 (2001) 165–205.
- [93] K.M. Simon, J.M. Chandra Kishen, A multiscale approach for modeling fatigue crack growth in concrete, *Int. J. Fatigue*. 98 (2017) 1–13.
- [94] Y. Wang, Physical stochastic damage model for concrete subjected to fatigue loading, *Int. J. Fatigue*. 121 (2019) 191–196.
- [95] H.W. Reinhardt, *Fracture Mechanics of an Elastic Softening Material Like Concrete*, *Heron*. 29 (1984) 1–42.
- [96] A. Hillerborg, M. Modéer, P.E. Petersson, Analysis of crack formation and crack growth in concrete by means of fracture mechanics and finite elements, *Cem. Concr. Res.* 6 (1976) 773–781.
- [97] J. van Mier, *Classical Fracture Mechanics Approaches*, *Concr. Fract.* (2012) 11–34.
- [98] B. Yang, S. Mall, K. Ravi-Chandar, A cohesive zone model for fatigue crack growth in quasibrittle materials, *Int. J. Solids Struct.* 38 (2001) 3927–3944.
- [99] M. Corrado, J.F. Molinari, Effects of residual stresses on the tensile fatigue behavior of concrete, *Cem. Concr. Res.* 89 (2016) 206–219.
- [100] S.A. Ponnusami, S. Turteltaub, S. van der Zwaag, Cohesive-zone modelling of crack nucleation and propagation in particulate composites, *Eng. Fract. Mech.* 149 (2015) 170–190.
- [101] D.Z. Yankelevsky, H.W. Reinhardt, Uniaxial Behavior of Concrete in Cyclic Tension, *J. Struct. Eng.* 115 (1989) 166–182.
- [102] D. Hordijk, Local approach to fatigue of concrete, PhD Thesis, Delft Univ. Technol. (1991) 216.
- [103] H.W. Reinhardt, H.A.W. Cornelissen, D.A. Hordijk, Tensile Tests and Failure Analysis of Concrete, *J. Struct. Eng.* 112 (1986) 2462–2477.
- [104] W. Ren, Z. Yang, R. Sharma, C. Zhang, P.J. Withers, Two-dimensional X-ray CT image based meso-scale fracture modelling of concrete, *Eng. Fract. Mech.* 133 (2015) 24–39.
- [105] K. Gylltoft, A fracture mechanics model for fatigue in concrete, *Matériaux Constr.* 17 (1984) 55–58.
- [106] F. Gong, T. Ueda, Y. Wang, D. Zhang, Z. Wang, Mesoscale simulation of fatigue behavior of concrete materials damaged by freeze-thaw cycles, *Constr. Build. Mater.* 144 (2017) 702–716.
- [107] E. Papa, A. Taliervo, Anisotropic damage model for the multiaxial static and fatigue behaviour of plain concrete, *Eng. Fract. Mech.* 55 (1996) 163–179.
- [108] J. Lemaitre, How to use damage mechanics, *Nucl. Eng. Des.* 80 (1984) 233–245.
- [109] D. Krajcinovic, Damage mechanics, *Mech. Mater.* 8 (1989) 117–197.
- [110] J. Lemaitre, A continuous damage mechanics model for ductile fracture, *J. Eng. Mater. Technol. Trans. ASME*. 107 (1985) 83–89.
- [111] J.L. Chaboche, Anisotropic Creep Damage in the Framework of Continuum Damage

- Mechanics., Trans. Int. Conf. Struct. Mech. React. Technol. (1983).
- [112] F. Leckie, A course on damage mechanics, Springer Science & Business Media, 1998.
- [113] W. Suaris, C. Ouyang, V.M. Fernando, Damage Model for Cyclic Loading of Concrete, *J. Eng. Mech.* 116 (1990) 1020–1035.
- [114] G.D. Nguyen, A thermodynamic approach to non-local damage modelling of concrete, *Int. J. Solids Struct.* 45 (2008) 1918–1934.
- [115] J. Mazars, G. Pijaudier-Cabot, Continuum Damage Theory – Application to Concrete, *J. Eng. Mech.* 115 (1989) 345–365.
- [116] K.M.P. Fathima, J.M.C. Kishen, A thermodynamic framework for the evolution of damage in concrete under fatigue, *Arch. Appl. Mech.* 85 (2015) 921–936.
- [117] K.M. Pervaiz Fathima, J.M. Chandra Kishen, A thermodynamic framework for fatigue crack growth in concrete, *Int. J. Fatigue.* 54 (2013) 17–24.
- [118] Y.F. Dafalias, Bounding Surface Plasticity. I: Mathematical Foundation and Hypoplasticity, *J. Eng. Mech.* 112 (1986) 966–987.
- [119] J. Liang, X. Nie, M. Masud, J. Li, Y.L. Mo, A study on the simulation method for fatigue damage behavior of reinforced concrete structures, *Eng. Struct.* 150 (2017) 25–38.
- [120] P. Grassl, R. Rempling, A damage-plasticity interface approach to the meso-scale modelling of concrete subjected to cyclic compressive loading, *Eng. Fract. Mech.* 75 (2008) 4804–4818.
- [121] B. Sun, Z. Xu, An efficient numerical method for meso-scopic fatigue damage analysis of heterogeneous concrete, *Constr. Build. Mater.* 278 (2021) 122395.
- [122] B. Wu, Z. Li, K. Tang, K. Wang, Microscopic multiple fatigue crack simulation and macroscopic damage evolution of concrete beam, *Appl. Sci.* 9 (2019).
- [123] H. Zhang, B. Šavija, S.C. Figueiredo, E. Schlangen, Experimentally validated multi-scale modelling scheme of deformation and fracture of cement paste, *Cem. Concr. Res.* 102 (2017) 175–186.
- [124] H. Zhang, Experimentally validated multi-scale fracture modelling scheme of cementitious materials, Delft University of Technology, PhD Thesis, 2019.
- [125] Z. Qian, Multiscale modeling of fracture processes in cementitious materials, Delft University of Technology, PhD Thesis, 2012.
- [126] M. Hlobil, V. Šmilauer, G. Chanvillard, Micromechanical multiscale fracture model for compressive strength of blended cement pastes, *Cem. Concr. Res.* 83 (2016) 188–202.
- [127] V.P. Nguyen, M. Stroeve, L.J. Sluys, An enhanced continuous-discontinuous multiscale method for modeling mode-I cohesive failure in random heterogeneous quasi-brittle materials, *Eng. Fract. Mech.* 79 (2012) 78–102.
- [128] Y. Gan, H. Zhang, M. Liang, E. Schlangen, K. van Breugel, B. Šavija, A numerical study of fatigue of hardened cement paste at the microscale, *Int. J. Fatigue.* 151 (2021) 106401.



# 3

## MICROMECHANICAL AND FATIGUE PROPERTIES OF CEMENT PASTE AT MICROSCALE

*This chapter presents an experimental investigation of fatigue properties of cement paste at the microscale. Micro-cantilever beam (MCB) specimens are prepared using a precision micro-dicing machine. The fatigue bending tests on the MCB specimens are carried out with the help of a nanoindenter. The fatigue properties of cement pastes in terms of fatigue life, stiffness degradation and residual deformation are studied. A comparison of static and fatigue fractured surfaces by means of microscopic observations of these surfaces is performed. X-ray computed tomography (XCT) technique is also used to assess the fatigue damage accumulation of cement paste. General discussions regarding the evolutions of fatigue damage and residual deformation are also provided*

### 3.1 INTRODUCTION

Many concrete structures, such as off-shore structures and bridges, are inevitably subjected to a large number of cyclic loadings [1–3]. Understanding the fatigue behaviour of concrete is of great importance for ensuring the safety and durability of these structures. However, the phenomenon of concrete fatigue is very complex as it inherently involves multiple spatial scales owing to the multiscale heterogeneous nature of concrete [4,5].

Over the past several decades, most research efforts devoted on the concrete fatigue focused on the macroscale [3,6–11]. Nowadays, the use of empirical  $S-N$  curves (stress level versus fatigue life), based on extensive experimental results, remain the primary method to study and describe the macroscopic fatigue performance of concrete due to its convenience for structural design. Some researchers have also modified the  $S-N$  approach by considering the probabilistic nature of concrete fatigue [1,12]. However, this approach fails to achieve a clear and thorough understanding of fatigue fracture process at the lower scales. In a recent theoretical work of Le and Bazant [13], nano-scale crack growth has been related to macroscopic fatigue strength of quasi-brittle materials based on fracture mechanics. The authors assumed that the propagation of nano-scale cracks is governed by thermally activated breakage of atomic bonds or rupture of nano-particle connections [13–15]. The proposed theoretical model yields a power-law relation for the stress-life curve, which agrees with the Basquin's law [16]. As for the scales between the nano- and the macro-scale, micro- and mesostructural mechanisms are believed to play an important role in the fatigue fracture process. At the mesoscale, concrete comprises cement paste, various sizes of aggregates and the interfacial transition zone (ITZ) between them (e.g. Figure 1-2). When subjected to the fatigue loading, it is found that the pre-existing cracks are situated mostly in the regions of the ITZ, will propagate first and then coalesce with the fatigue cracks in the cement paste matrix [17–24]. Even though both the ITZ and matrix are experiencing fatigue damage, fatigue crack growth in ITZ seems to be faster than that in the matrix. The effects of some meso-scale features, such as the aggregate type, air content and properties of pastes, on the fatigue performance of concrete have been investigated by several researchers [6,17–23,25,26]. It is clear that the meso-structure of concrete and local mechanical properties of its constituents, including both static and fatigue properties, have a strong influence on the global fatigue performance. Whereas the mesoscale fatigue behaviour of concrete has been extensively studied in recent years, the available data concerning the fatigue behaviour of cement paste at the microscale is rather scarce. Since cement paste is the binding phase in concrete, knowledge regarding the microscopic changes of cement paste subjected to fatigue loading is considered most important for fatigue analysis of concrete and requires deeper understanding.

This chapter presents an experimental investigation of fatigue properties of cement paste by conducting microscale tests. The miniaturized cement paste specimens are first fabricated and then subjected to both monotonic and cyclic loading to assess

their flexural strength and fatigue properties, respectively. The microscopic observations on the fracture surfaces are also performed to gain a better understanding of the cement paste fracture under different loading conditions. General discussions on the evolution of fatigue damage and residual deformation are also provided.

## 3.2 EXPERIMENTAL APPROACH

### 3.2.1 MATERIALS

Cement pastes with w/c ratio of 0.4 and 0.5 were prepared using standard grade CEM I 42.5 N Portland cement (ENCI, the Netherlands) and deionized water. The Blaine fineness of cement is  $2840 \text{ cm}^2/\text{g}$  (provided by the manufacturer). The pastes were first cast in plastic cylindrical moulds with 24 mm diameter and 39 mm height. The fresh paste was rotated at a speed of 2.5 rpm for 24 hours at room temperature (20 °C) to prevent bleeding. The samples were cured under sealed condition at room temperature for 28 days. After demoulding, the hardened cement paste specimens were cut into slices with the thickness of 3 mm. The slices were then immersed in isopropanol to arrest the hydration [27].

### 3.2.2 PREPARATION OF MICRO-CANTILEVER BEAMS

Micro-cantilever beam (MCB) specimens were prepared using a precision micro-dicing machine (MicroAce Series 3 Dicing Saw), which is generally used to cut semiconductor wafers. Firstly, cement paste slices were ground to obtain two smooth and parallel surfaces using a Struers Labopol-5 thin sectioning machine. In this grinding process, two grinding discs of  $135 \text{ }\mu\text{m}$  and  $35 \text{ }\mu\text{m}$  were used in sequence. The thickness of each slice was controlled at  $2150 \text{ }\mu\text{m}$ . Afterwards, two perpendicular cutting directions with the same cutting spacing were applied on the samples using the micro-dicing machine. In this way, multiple rows of cantilever beams with a square cross section of  $300 \text{ }\mu\text{m} \times 300 \text{ }\mu\text{m}$  were generated. The cutting depth, i.e. the cantilevered length, was approximately  $1650 \text{ }\mu\text{m} \pm 10 \text{ }\mu\text{m}$ . The cutting process is schematically shown in Figure 3-1.

The cross-sections of several beams have been examined by using an Environmental Scanning Electron Microscope (ESEM), see Figure 3-2. No cracking as a consequence of the cutting process has been observed. An overall accuracy of the cross-sectional dimensions of  $\pm 1.5 \text{ }\mu\text{m}$  can be reached with this fabrication process. Precautions have also been taken to minimize the carbonation of the samples before testing by storing the beams in isopropanol. Due to the low surface tension, it is generally agreed that the isopropanol immersion could reduce shrinkage stresses that cause microstructural changes in normal drying [27].

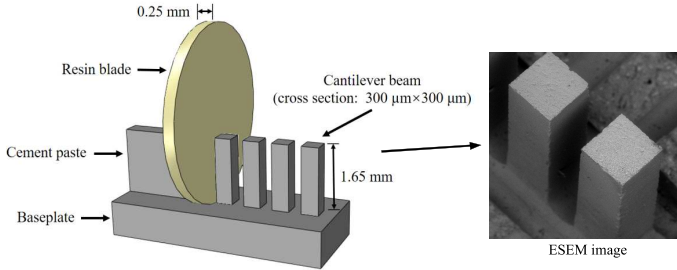


Figure 3-1 Schematic diagram of sample preparation [28]

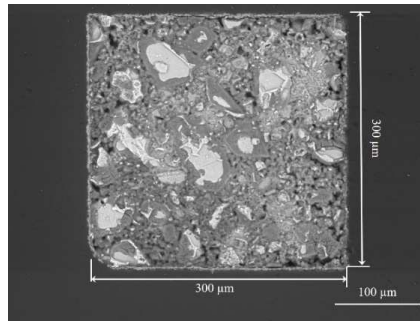


Figure 3-2 Backscattered electron image of the cross-sections of MCB with  $w/c$  0.4

### 3.2.3 EXPERIMENTAL SET-UP

Quasi-static and fatigue tests were performed using a KLA Nano-indenter G200. The Nano-indenter was equipped with a cylindrical wedge indenter tip with a length of 200  $\mu\text{m}$  (Figure 3-3). It was used to apply vertical line loads at the free end of the MCB. Before testing, the angle and centre of the tip were calibrated by probing into a standard aluminium reference sample. Afterwards, the baseplate of MCB was attached on a metal surface using cyanoacrylate adhesive, and the angle of beam was carefully adjusted under the in-situ microscope in the nanoindenter to ensure that the line load is applied perpendicular to the beam's longitudinal axis. The experimental set-up is schematically shown in Figure 3-4. Before starting the test, the coordinates of the loading position and the fixed end were recorded under the microscope to determine the loading length  $L$  of each beam. All tests were conducted in a well-insulated chamber preventing any significant change of temperature and RH. The average temperature and RH during the tests were  $26.1 \pm 0.6$   $^{\circ}\text{C}$  and  $34.4\% \pm 0.7\%$ . Prior to the tests, the samples were kept in



the chamber for temperature equalization until the thermal drift rate was below 0.05 nm/s. It is well known that the size of the specimen indicated by the volume to surface ratio considerably affects the drying process [29]. Due to the extremely thin cross-section with the volume to surface ratio of only 0.07 mm, the MCBs quickly equilibrated to the ambient RH prior to the tests. In consideration of the low RH used in this study, it can be expected that there is little free water in capillary pores [30].

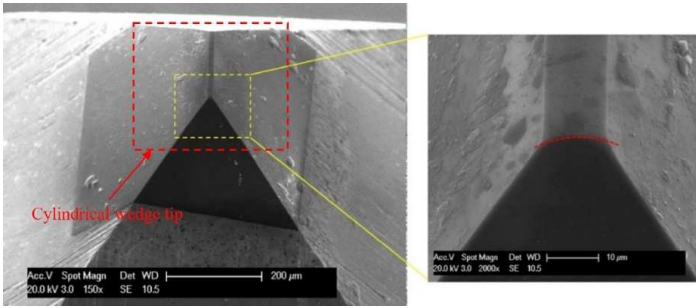


Figure 3-3 Secondary electron image of the diamond cylindrical wedge tip with an enlarged view of the tip head

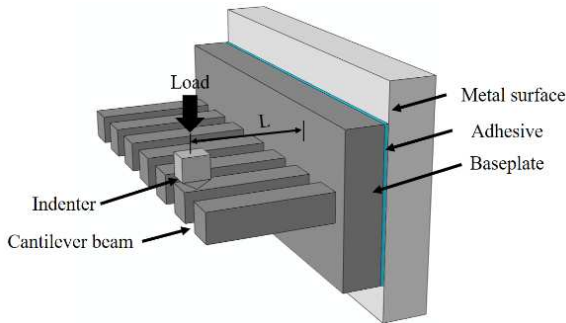


Figure 3-4 Schematic diagram of test set-up

### QUASI-STATIC BENDING TEST

Before fatigue testing, the mechanical properties of MCBs, i.e. flexural strength and static elastic modulus, should be determined. For each w/c ratio, 30 cantilever beams were monotonically loaded to failure. The loading procedure was displacement-controlled with a constant loading rate of 50 nm/s. The load and displacement

responses were measured by the Nano-indenter. In general, a major crack initiates near the fixed end of the beam during loading, which eventually leads to complete fracture of the beam. After the static failure, the coordinates of the fracture point were also recorded to determine the fractured length  $d$  of each beam. The maximum load  $F_{\max}$  and slope of load-displacement curve  $k$  (in the range between 40% and 60% of the maximum load) during loading are used to determine the flexural strength  $f_t$  and static elastic modulus  $E_{\text{static}}$ , respectively, according to the classical beam theory [28,31,32]:

$$f_t = \frac{F_{\max} dh}{2I} \quad (3-1)$$

$$E_{\text{static}} = \frac{kL^3}{3I} \quad (3-2)$$

where  $d$  is the fractured length,  $h$  is the side length of the square beam cross-section, and  $I=h^4/12$  is the moment of inertia. Since the end of the cantilever beam is not perfectly fixed, there may be some additional displacement under loading due to the deformation of baseplate and the adhesive layer. By using the finite element method [28], it was found that the deformations of the baseplate and the adhesive layer account for  $14 \pm 0.2\%$  and  $0.5 \pm 0.1\%$  of the total displacement, respectively. These additional displacements will be excluded from the determination of the elastic modulus. Moreover, in order to validate the experimental protocol, five glass cantilever beams were fabricated and tested. The measured average elastic modulus of glass beams through bending tests is  $69.1 \pm 1.2$  GPa, which has been calibrated by excluding the effects of the baseplate and the adhesive layer. For comparison, the conventional nanoindentation technique equipped with a Berkovich tip was used to measure the indentation modulus of glass. In total, 10 indents were performed, and the measured average indentation modulus is  $70.1 \pm 1.8$  GPa, which is very close to the result obtained with the developed cantilever bending tests. Therefore, the methods of testing and interpretation of the results used in the current paper are considered reliable.

#### FATIGUE BENDING TEST

The fatigue bending tests were carried out under load control. The cyclic loads were applied in the form of triangular loads with a constant amplitude at a loading frequency of 0.55 Hz, see Figure 3-5. For each value of the  $w/c$  ratio, 30 MCBs were tested under different loading levels. For  $w/c$  0.4 series, the maximum loading level ranged from 50 mN to 70 mN, corresponding to around 75-95% of static flexural strength, and the minimum loading level was kept around 1.5-2.1 mN. The maximum loading level of  $w/c$  0.5 series varies from 35 mN to 50 mN, which corresponded to approximately 70-95% of static flexural strength. The minimum loading level for this series was around 1.0-1.5 mN. The stress ratio  $R$  between minimum and maximum cyclic load was kept equal to 0.03. During the fast loading-unloading regime, the loading magnitude was not perfectly controlled by the Nano-indenter. Small disturbances (2-5%

of loading amplitude) for both upper load and lower load were observed. Therefore, the recorded actual loading level was used for the determination of the stress level. Before each fatigue test, the MCB was preloaded to the maximum load and completely unloaded to reduce the possible plastic deformation generated under the indenter tip.

Due to the technical limitation of the testing duration capacity of the used nano-indenter, the fatigue testing procedure was separated into multiple cycle blocks with identical loading procedure. Each cycle block contains 500 loading-unloading cycles and is automatically conducted in succession with a very short rest period (around 100 s). The beam is completely unloaded after finishing one cycle block and then reloaded for the next cycle block. Run-out tests were stopped at the limit of 200,000 cycles. At the end of each cycle block, the nano-indenter will apply a constant low load with around 0.01% of maximum load to measure the drift rate and automatically calibrate the displacement responses. However, most of the measured drift will be affected by the viscoelastic recovery because of the viscoelastic nature of cement paste [33]. Therefore, the calculated drifts were deducted from the calibrated total time-dependent displacements for all tests. Many researchers found that the deformation of cementitious material exhibits a three-stage behaviour, which can be used to evaluate the development of fatigue damage [2,34–37]. Figure 3-6 shows the typical displacement-cycles number curve of MCB. Overall, the displacement evolution can also be divided into three stages: the first stage is unstable and comparatively transient, which accounts for only 1–2% of the total test duration. With the continuation of cyclic loading, the displacement curve turns into a stable stage, which covers around 99% of the whole test duration. In the third stage, the displacement increases rapidly within a few cycles until the MCB suddenly fails, which results in an overshoot of the indenter tip, as is shown in Figure 3-6.

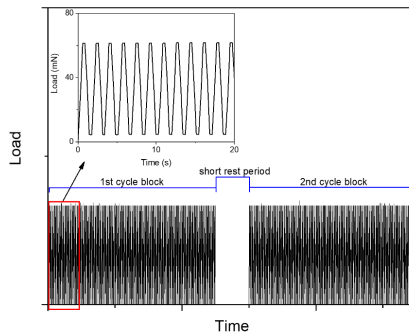


Figure 3-5 Cyclic load history applied in MCB fatigue tests

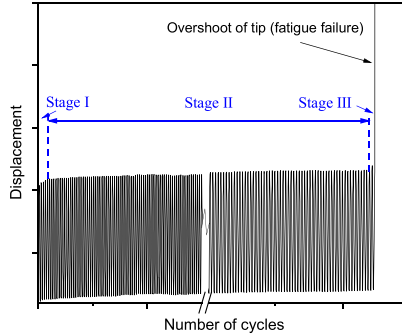


Figure 3-6 Typical displacement-number of cycles curve

Another important characteristic investigated in most fatigue studies is the increase of the strain at the maximum or minimum loading level during the loading cycles [2,34–36,38]. In this study, the change of strain at the maximum loading level is defined as the residual strain, and the fatigue compliance  $C(t)$  was defined by dividing the residual strain by half of the applied maximum stress ( $\sigma_{\max}/2$ ). For each MCB, the time-dependent strain  $\varepsilon(t)$  at the upper fibre at the fixed end of the beam and the corresponding fatigue compliance were calculated based on the classical beam theory:

$$\varepsilon(t) = \frac{3\delta h}{2L^2} \quad (3-3)$$

$$C(t) = \frac{2\varepsilon(t)}{\sigma_{\max}} \quad (3-4)$$

where  $\delta$  is the measured displacement of the indenter tip. Figure 3-7 shows the typical development of residual strain at the upper fatigue load. For each individual cycle block the residual strain development after a few cycles (initial stage) turns into a stable stage. Only in the last cycle block the residual strain starts to increase rapidly before the fatigue failure. For each MCB the residual strain and the corresponding fatigue compliance of each cycle block at the second stage have been calculated and averaged.

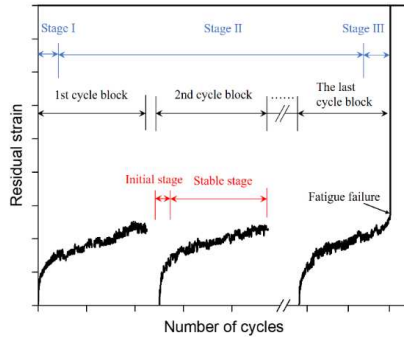


Figure 3-7 Typical development of residual strain at the maximum fatigue load

Attempts have also been made to assess the fatigue damage inside the cement paste by using the non-destructive X-ray computed tomography (XCT) technique [39,40]. As is shown in Figure 3-8, the region of interest (ROI) in the initial microstructure of MCB, i.e. the local region near the fixed end of beam with the size of  $300 \times 300 \times 600 \mu\text{m}^3$ , was first scanned before the fatigue test was performed. The scanned MCB was then subjected to cyclic loadings up to 200,000 cycles with a stress level of 90% of the static strength. Afterwards, the damaged sample was scanned again to evaluate possible fatigue damage. After acquiring the grey-value based XCT images, pore segmentation was conducted using the global threshold method [41]. Three additional intact beams for each w/c ratio were also scanned and segmented to determine the total porosity. The X-ray source tube was set at 90 kV/100  $\mu\text{A}$  during scanning, resulting in a voxel resolution of  $0.5 \times 0.5 \times 0.5 \mu\text{m}^3$ .

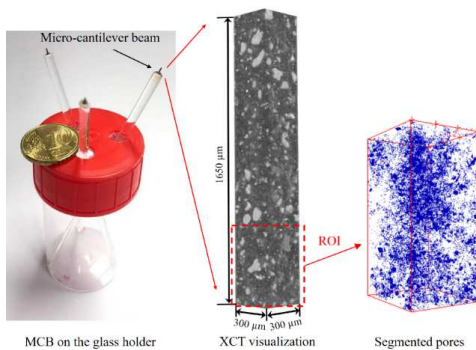


Figure 3-8 The CT scanning of the micro-cantilever beams and segmented pore structure

### 3.3 EXPERIMENTAL RESULTS AND DISCUSSION

#### 3.3.1 MECHANICAL PROPERTIES MEASURED IN QUASI-STATIC TESTS

Figure 3-9 shows the typical load-displacement of MCB under the monotonic loading. The static mechanical properties, as well as porosities of cement pastes measured by XCT for both w/c ratios at the age of 28 days, are summarized in Table 3-1. As was expected, a lower w/c ratio, and hence a lower porosity, leads to higher elastic modulus and strength. Note that pores smaller than the image resolution (i.e. 0.5  $\mu\text{m}$ ) cannot be detected by XCT. Therefore, the porosity measured by XCT is much lower than the result of the mercury intrusion porosimetry (MIP) [42]. Nevertheless, the difference in porosity for different w/c ratios is clear. When the measured elastic moduli are plotted against flexural strengths in Figure 3-10, a general positive correlation between these two properties can be observed for both w/c ratios. Due to the highly heterogeneous nature of cement paste at the microscale, the results exhibit a large scatter, as was expected [28,31]. More specifically, the local spatial distribution of pores and hydration products at the fixed end of the beam may largely affect the strength of MCB, while the global microstructure of MCB accounts for the variation of the elastic modulus. The relationship obtained in Figure 3-10 will be used in the analysis of fatigue results.

Table 3-1. Measured porosities and mechanical properties of MCBs (28d)

w/c ratio	Porosity (XCT results)	$E_{\text{static}}$ (GPa)	$f_i$ (MPa)
0.4	7.40% $\pm$ 0.43%	15.09 $\pm$ 2.06	24.23 $\pm$ 2.90
0.5	12.06% $\pm$ 0.75%	10.19 $\pm$ 2.46	19.47 $\pm$ 4.38

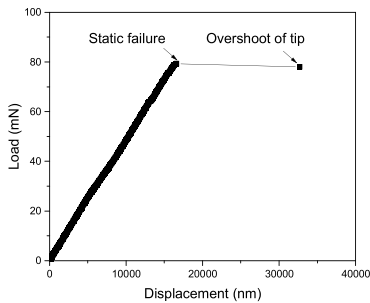


Figure 3-9 Typical load-displacement curve of MCB (w/c 0.4, 28d) under monotonic loading

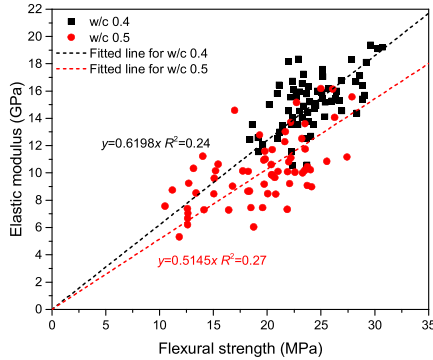


Figure 3-10 The relationship between the elastic modulus and flexural strength (28d)

### 3.3.2 FATIGUE LIFE AND $S-N$ CURVES

Fatigue behaviour of materials, both from a scientific and engineering perspective, are normally described by the so-called  $S-N$  curves. These curves usually present a (linear) relationship between the logarithm of the number  $N$  of cycles and the maximum fraction of the strength, i.e. stress level  $S$ . This relationship is known as the Wöhler fatigue equation [3], and is given by:

$$S = -a \cdot \log(N) + b \quad (3-5)$$

where  $a$  and  $b$  are experimental coefficients. Note that there is another fatigue equation [6,43,44], which considers the ratio of minimum fatigue stress to the maximum fatigue stress. Since this stress ratio was kept low and constant (i.e. 0.03) for each fatigue test, the fatigue equation Eq.(3-5) is adopted in current study. In general, the average strength measured in static tests is used to determine the nominal stress level for fatigue experiments. This engineering approach is used for convenience, as negligible variation of sample strength is expected at the macroscale. However, the large variations of mechanical properties at the microscale may undermine the correctness and practicality of this method. To consider the variation of strength of each MCB, the initial elastic modulus (determined by the slope of the stress-strain curve in the range of 40-60% of strength) was used to predict the strength based on the linear correlation obtained in Figure 3-10. Although the correlation is far from perfect, this allows to reduce the scatter originating from the variation of material properties. One should also note that, in comparison to quasi-static testing at lower strain rates, the accelerated cyclic loading tests with faster loading rates may lead to higher flexural strengths due to the strain rate sensitivity of cementitious materials [45-48]. Consequently, the

calculated stress levels are likely to be artificially higher than ‘true’ stress levels determined as a function of static strengths measured at strain rates equivalent to the loading rate during the fatigue tests. Nevertheless, these stress levels determined in this study are only used as guidelines. For comparison, both the nominal stress levels  $S_{nom}$  using the average strengths measured in previous quasi-static tests and the modified stress levels  $S_{mod}$  considering individual sample strength, which is based on elastic modulus, have been calculated.

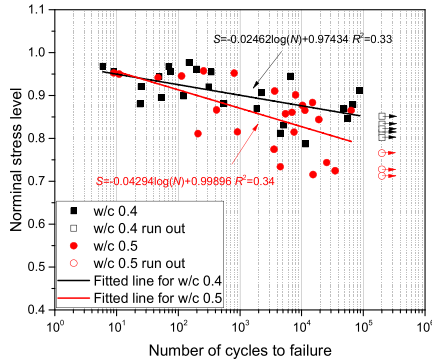


Figure 3-11 The nominal stress level versus number of cycles to failure

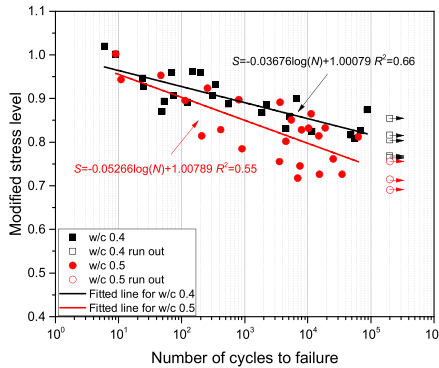


Figure 3-12 The modified stress level versus number of cycles to failure

The  $S-N$  curves using the nominal and modified stress levels are shown in Figure 3-11 and Figure 3-12. Based on the least-squares method, linear regression analyses



were carried out to determine the parameters in the Wöhler equation, i.e. Eq.(3-5). In Figure 3-11, it is difficult to find a clear trend when the nominal stress level is used. The fatigue life for the same nominal stress level is very scattered at the microscale, as illustrated by the low coefficients of determination ( $R^2$ ). The results in Figure 3-12 show higher coefficients of determination when the variation of strength for individual samples is considered. Nevertheless, the value of  $R^2$  is still low. It seems difficult to consider all the sources of scatter. For all modified stress levels ( $S_{mod}$ ), the fatigue life of w/c 0.4 sample is generally higher than that of w/c 0.5 sample.

It has been reported that the fatigue behaviour of quasi-brittle materials in terms of fatigue life and crack growth rate are strongly dependent on the specimen size [13,15,23,49–55]. When the results obtained in this study are compared to the macroscopic fatigue results of cement paste presented in the literature [56,57], it is found that, given the same nominal stress level, the fatigue life of microscopic cement paste specimen is apparently longer. For instance, at the nominal stress level of 80%, the number of cycles to failure for cement paste subjected to compressive cyclic loading at the macroscale lies in the range of  $10^2$ - $10^4$  [56–58], which is almost two orders of magnitude lower than the flexural fatigue life of MCB at the microscale. For stress levels lower than 80%, the difference in fatigue life becomes even larger. Note that the compressive fatigue resistance of cementitious materials is found to be only slightly higher than their tensile fatigue resistances at the same stress levels [59]. It is also suggested by [3] that similar  $S$ - $N$  equations can be used for both compressive and flexural fatigue.

It has been widely reported that the fatigue life of cementitious materials decreases with decreasing loading frequency [34,44,60]. In this study, the MCBs were subjected to cyclic loading with loading frequency of only 0.55 Hz. This is much lower than the commonly used frequency in macroscopic tests (5-10 Hz) [34,44,60,61], but the samples still exhibit longer fatigue life. It should also be pointed out that, if one considers the absolute magnitude of the stress, the number of cycles to failure at a particular stress is much higher for small samples than for large samples [23], as the strength of cement-based specimen is also size-dependent [62,63]. The fatigue size effect of quasi-brittle materials was first demonstrated in the works of Bažant and co-workers [50,51] and has recently been tested and analysed by Kirane et al. in [49]. The fatigue crack growth rate, which is related to the Paris' law coefficient, is found to exhibit a substantial size effect, analogous to the size effect of fracture under monotonic loading [49]. In other words, the fatigue damage evolution becomes slower for smaller samples and, consequently, the fatigue life tends to increase with decreasing sample size [23,49,50]. In contrast to normally used laboratory-scale cement paste samples, the MCBs at the microscale do not contain initial large defects, like meso-cracks and air voids ( $> 300 \mu\text{m}$ ), which could eventually reduce the overall fatigue resistance [64]. Furthermore, due to the extremely thin cross-section of MCB, very low moisture gradients would be expected before and during the testing. This may result in a lower degree of shrinkage-induced eigenstresses compared to larger samples, which could also give rise to the better fatigue performance [18].

### 3.3.3 EVOLUTION OF FATIGUE DAMAGE

It has been recognized that cement-based materials under fatigue loading experience progressive damage accumulation, which is mainly attributed to the initiation and propagation of microcracks [22,65]. In general, the gradual development of fatigue damage causes a steady decrease in the stiffness of the material [66]. Therefore, degradation of stiffness can be used as an indicator of fatigue damage evolution. In addition, direct examination of the microstructure through XCT technique could also help to reveal possible growth of microcracks. In this study, both approaches were attempted to characterize the fatigue damage.

#### CHANGES IN MCB STIFFNESS

The stiffness of MCB is determined by the slope of the ascending load-displacement curve under cyclic loading. For each w/c ratio, the variations of stiffness of 10 MCBs with the highest nominal stress levels were normalized to the initial stiffness ( $k_{in}$ ) and plotted against the normalized number of cycles. The result is shown in Figure 3-13. Despite the small fluctuations, the stiffness of most samples decreased only slightly with the number of cycles during the whole fatigue life, and some of them even remained unchanged before fatigue failure. The average reduction in stiffness before failure is calculated as  $2.76 \pm 1.31\%$  for w/c 0.4 samples and  $4.01 \pm 3.06\%$  for w/c 0.5 samples. Unlike most macroscopic fatigue results obtained from mortar or concrete samples [34,66,67], where distinct stiffness reductions of around 10-40% were observed and damage generated mainly at the interfacial transition zone (ITZ), the cement paste at the microscale seemed to experience very slow and limited damage accumulation during most of the fatigue life. Once nano- or microcracks nucleate and form a major crack under cyclic loading, the MCB fails immediately. It turns out that a very small degree of fatigue damage is sufficient to cause a complete fatigue failure of MCB. Note that slight increases in mechanical properties of concrete samples after fatigue tests have also been reported in the literature [37,67,68]. This phenomenon may be attributed to possible strengthening mechanisms such as the consolidation or compaction of cement paste or relief of eigenstress under cyclic loading in the regions surrounding the cracks. These effects may also account for the observed low stiffness degradations of MCBs. Since the remaining strengths of run-out MCBs were not measured after fatigue tests, these possible strengthening mechanisms could not be verified in the current research.

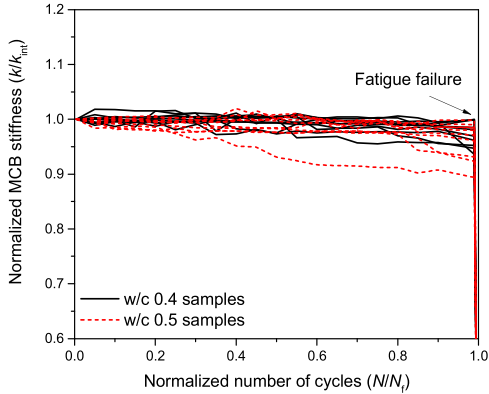


Figure 3-13 Stiffness degradations of 10 MCBs (28d) for each w/c ratio under cyclic loading (note that vertical axis does not start at zero)

#### FATIGUE DAMAGE EVALUATION THROUGH XCT

XCT observations were carried out on a group of MCBs. Owing to the large scatter of fatigue results, accurate prediction of fatigue life and damage monitoring at the microscale are extremely challenging. As a result, several samples have failed before the second scanning (200,000 cycles). Nevertheless, two remaining samples (w/c 0.4) were scanned and analysed. The fatigue damage evaluation through XCT is schematically shown in Figure 3-14. After the pore segmentation, the average porosity of the region of interest (ROI) changed from  $7.72 \pm 0.45\%$  to  $7.80 \pm 0.38\%$ . It appears that the porosities measured by XCT are almost identical for original and damaged samples. This may suggest that most of fatigue damage occurred at much smaller length scale, at least lower than the XCT resolution (i.e.  $0.5 \mu\text{m}$ ), which cannot be detected by the XCT. Note that, for concrete samples the fatigue damage at later stage is often visible and can be clearly identified using XCT [40,66,69,70] when a significant number of cracks with large crack widths is generated near the ITZ. The fatigue damage in cement paste could be in the form of cracking and crack propagation at the nanoscale or associated with separations between nano-gel particles of the calcium silicate hydrate [13]. Therefore, XCT with limited resolutions may not be an appropriate approach to capture minor fatigue damage of cement paste at the microscale. More sensitive non-destructive techniques, such as electrical resistivity measurement [71], dual-CT approach [72] and ultrasonic pulse attenuation [73], could be useful in this case. However, the difficulty in setting up small-scale measurement would become another challenging technical mission.

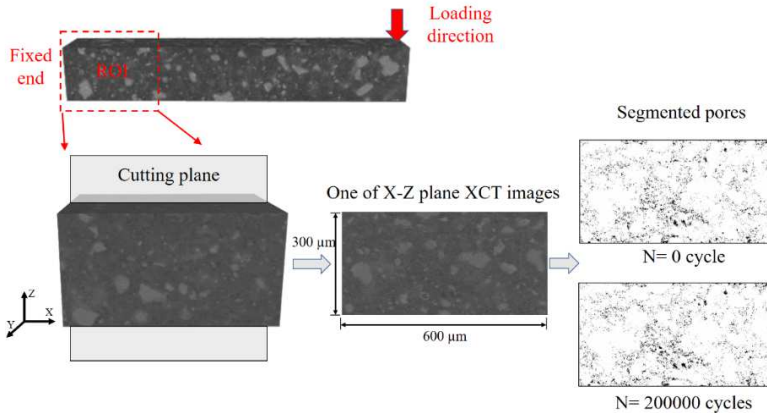


Figure 3-14 XCT examination of fatigue damage in MCBs (w/c 0.4)

### 3.3.4 ESEM ANALYSIS OF FRACTURE SURFACE

For a better insight into the fatigue failure, ESEM image analyses were performed to study the fractured surfaces of MCBs after static and fatigue failure. The fractured beams were examined using both secondary electron (SE) and backscattered electron (BSE) modes in an ESEM. Figure 3-15 compares the BSE and SE images of the typical static and fatigue fracture surfaces of MCBs at the magnification of 500x. At a first glance, the overall difference between the static and fatigue fracture at this magnification is not obvious. It is known that the critical crack under flexural loading is most likely to initiate and propagate in the tensile zone of the cross-section (marked as red box in Figure 3-15). Therefore, particular attention was paid on these areas, as is shown in Figure 3-16 and Figure 3-17.

Based on the BSE and SE images, multiple phases can be identified in the cement paste at the microscale, such as calcium hydroxide (CH), ettringite and calcium-silicate-hydrate (C-S-H). Some small cracks can also be found from these images at higher magnifications. The detected small cracks were marked for static and fatigue fractured surfaces (w/c 0.5) and presented in Figure 3-18 and Figure 3-19, respectively.

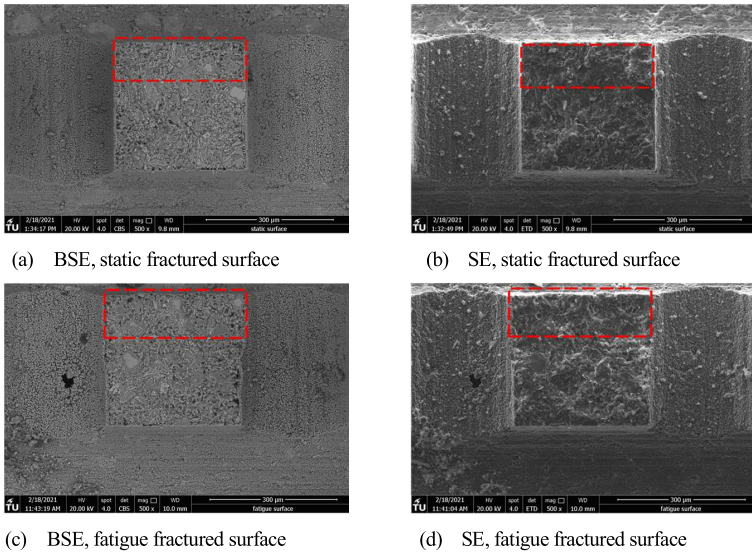


Figure 3-15 The overview of static and fatigue fractured surfaces (w/c 0.5)

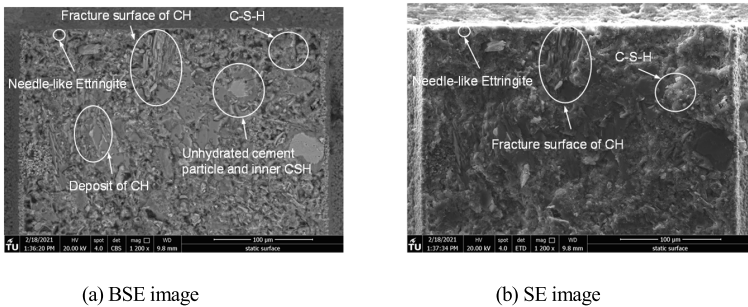


Figure 3-16 The (a) BSE image; (b) SE image of tensile zone of MCB after static failure (w/c 0.5)

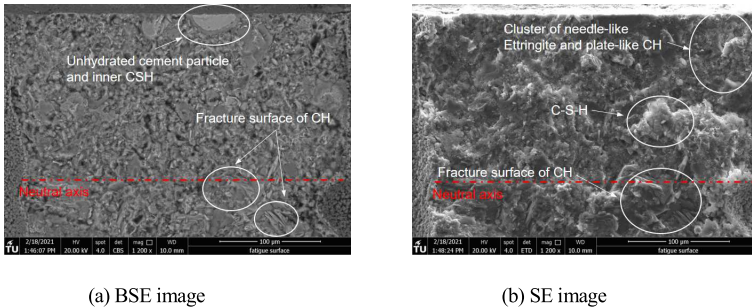
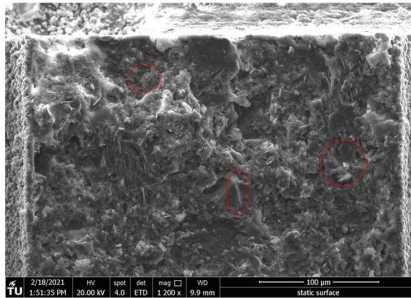


Figure 3-17 The (a) BSE image; (b) SE image of tensile zone of MCB after fatigue failure (w/c 0.5)

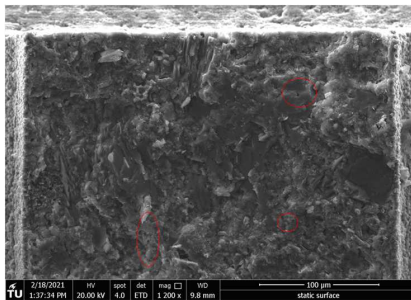
Compared with the static failure samples, a higher density of cracks can be observed in fatigue fracture surfaces. Most of these small cracks are found in the fractured C-S-H phases, which are generally distributed around the stiff particles (e.g. unhydrated cement particle and CH) or near the pores. More importantly, most of them are nano-scale cracks and have a crack width less than 500 nm. Note that a few observed fractures of CH (see Figure 3-17, near the neutral axis of the cross-section of beam) are believed to be caused by unstable cracking behaviour in the final stage of fatigue tests. It is suggested that, under the fatigue flexural loading, fatigue damages in the form of multiple nano-cracks were generated and developed in the tensile zone of the cantilever beam. The fatigue crack growth behaviour at the nanoscale may be associated with the rupture of connections between C-S-H gel particles [13]. The slow stiffness degradation might be attributed to the accumulation of these minor damages. Furthermore, the randomly distributed nano-cracks with a relatively higher crack density could also explain the large scatter of the fatigue life to a certain degree as any small crack has the potential to develop into the primary crack, resulting in final fracture. By contrast, there are much fewer small cracks propagating during the monotonic flexural loading. This is also in accordance with findings reported in [13,15,50], where much larger fracture process zones (FPZ) were measured in fatigue tests than in the static tests. In several fatigue studies [43,74], some traces of “friction” were found on the fatigue fractured surfaces. Several researchers believe that dissipative mechanisms, such as internal sliding and friction between crack surfaces, are the main sources of fatigue damage evolution [75,76]. However, this kind of damage could not be detected in the ESEM images with current magnifications, and is possibly not significant in flexural fatigue tests.

The combined XCT and ESEM observations indicate that apparently sound material was already damaged before the fatigue failure occurred. The nanoscale fatigue crack growths in C-S-H phases could explain the limited stiffness degradation of MCBs. Since it is currently not possible to trace all local sub-microscopic damages, a

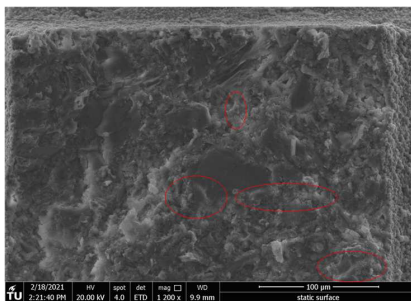
more appropriate approach is to consider fatigue as an essentially statistical effect of events on a nano-scale, as is suggested in [12,77].



(a)



(b)



(c)

Figure 3-18 Three static fractured surfaces of MCBs and marked cracks

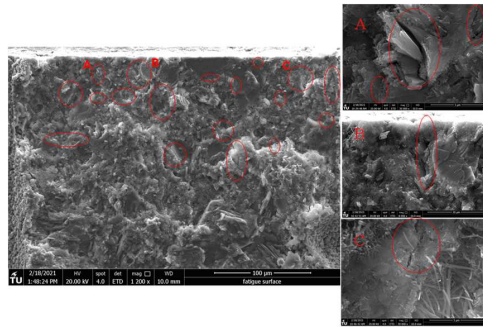
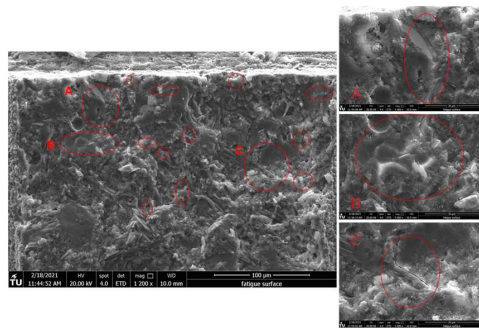
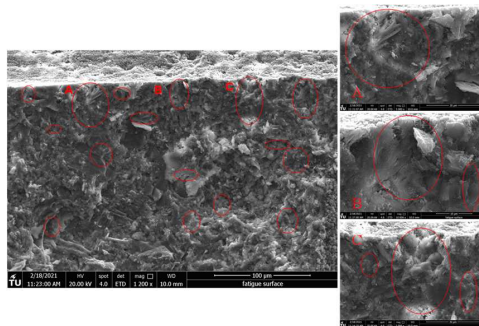
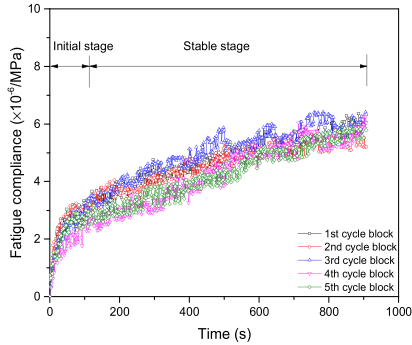
(a)  $N_f = 63544$ (b)  $N_f = 35045$ (c)  $N_f = 10328$ 

Figure 3-19 Three fatigue fractured surfaces of MCBs and marked cracks with (a)  $N_f = 63544$ ; (b)  $N_f = 35045$  and (c)  $N_f = 10328$

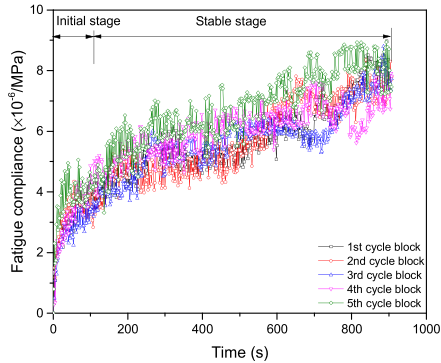


### 3.3.5 DEVELOPMENT OF FATIGUE COMPLIANCE

Figure 3-20 displays the typical fatigue compliance evolution of MCB subjected to multiple cycle blocks. The fatigue compliances increase with the number of cycles, showing two distinct stages, which are similar for different cycle blocks. Despite the discontinuity between each load block, the development of residual displacement shows an overall increasing trend with a nearly identical slope.



(a) w/c 0.4



(b) w/c 0.5

Figure 3-20 The evolution of fatigue compliance for (a) w/c 0.4 and (b) w/c 0.5

It is documented in literature that the first stage is characterised by a rapid increase of deformation, which is generally believed to be caused by the initiation and propagation of initial material defects, like microcracks and pores [34,61,78]. The second stage, presenting an almost linear increase of deformations, is explained by the stable crack growth [61,78]. This stable growth of deformation at the second stage, which occupies almost 95% of fatigue life, depends on the amplitude of the stress intensity factor near the crack tip [13,15,49]. The third stage before fatigue failure, which is shown in Figure 3-7, always shows a dramatic increase in deformation due to an unstable crack growth. However, as has been found previously for the stiffness evolutions and XCT observations of MCBs, the fatigue damage of cement paste at the microscale seems to be very small and slow. The linearly increased deformation at the second stage cannot be explained solely by the minor damage accumulation. The cyclic creep, or so-called fatigue creep, must be included in the fatigue deformation of cement paste due to the visco-elastic/plastic nature of C-S-H [2,31,79–81]. Note that the term ‘creep’ used here is mainly referred to the time-dependent deformation behaviour of C-S-H [82,83]. It has been suggested by Gao et al. in [2] that the residual strain of concrete in the first stage is mainly caused by the cyclic creep effect, while the coupling of cyclic creep and fatigue damage determines the irreversible strain accumulation in the second stage [2,79].

In order to examine the viscoelastic deformation of cement paste under cyclic loading, the Boltzmann superposition principle (BSP) is adopted here [84]. This principle allows the calculation of linear viscoelastic deformation of a material subjected to an arbitrary stress history by assuming an independent response to any given load. The basic creep compliance evolution of cement paste under constant loading can be determined by the combinations of rheological models or experimental data. In this study, the power-law function suggested in [31,85–87] is used. The formulation of the BSP for a multistep viscoelastic strain  $\varepsilon_{ve}$  of cement paste reads:

$$\varepsilon_{ve}(\sigma, t) = \sum_{i=1}^n [\sigma(t_i) - \sigma(t_{i-1})] \left[ \alpha \left( \frac{t - t_i}{t_1} \right)^\beta \right] \quad (3-6)$$

where  $\sigma(t_i) - \sigma(t_{i-1})$  is the actual stress increment in time interval  $(t_i - t_{i-1})$ .  $\alpha$  and  $\beta$  are two creep parameters, where the inverse of  $\alpha$  is the so-called creep modulus [85]. These two parameters may slightly differ for each individual sample because of the heterogeneity of cement paste at the microscale. If the w/c 0.4 samples are considered here, the average creep parameters, which have been experimentally measured in the author’s previous work [33], are 1.47 and 0.203 for  $\alpha$  and  $\beta$ , respectively. By inserting the real cyclic loading history (Figure 3-5) in the equation, the viscoelastic deformation is obtained. Figure 3-21 presents the comparison of fatigue compliance for w/c 0.4 samples, obtained from experiments and the BSP-based calculation. As shown in Figure 3-21, the viscoelastic deformation based on BSP seems to account for most of the residual deformation of cement paste under cyclic loading, especially in the first stage.

With the increase of the number of cycles, the viscoelastic deformation seems to account for most of the measured fatigue compliance, whereas a slight deviation from the experimental results is observed at the later stage. This deviation could probably be explained by the coupled effect of fatigue crack growth and intrinsic viscoelastic deformation [2,79]. Overall, the major portion of the measured residual strain can be attributed to the viscoelastic deformation of cement paste. In addition, the numerical work of Corrado and Molinari [18] indicates that eigenstresses locally released around the cracks may induce a mismatch between the crack surfaces, which inhibits a perfect crack re-closure and contributes to the observed residual strain. However, their numerical results show that the simulated values of residual deformation due to eigenstresses are only a small portion of the experimentally measured residual deformations. The possible concomitant effect of another mechanism suggested by the authors [18] is the formation of small debris, which may further prevent the crack closure [26]. Despite the complex deformation behaviour of cement paste in the second stage, the increase of the density of fatigue cracks and crack width along with the propagation of fatigue cracks are the main reasons for the development of residual fatigue compliance at the final stage.

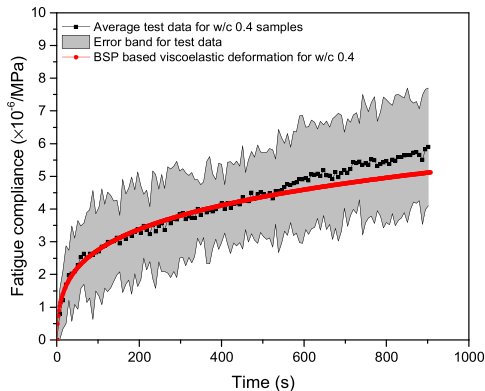


Figure 3-21 The comparison of fatigue compliance curves for w/c 0.4 between test data and BSP based calculations

### 3.4 CONCLUSIONS

In this chapter, micro-cantilever cyclic bending tests have been performed to investigate the fatigue properties of cement paste at the microscale. The following conclusions can be drawn from the experimental results:

- (1) Given the same stress level, the fatigue life of microscopic cement paste specimen is almost two orders of magnitude longer than that of macroscopic cement paste specimen, indicating a strong size dependency of fatigue behaviour for the paste specimen.
- (2) The microscopic fatigue damage evolution in cement paste is found to be very slow, indicated by the longer fatigue life as well as the little generated damage compared to macroscopic fatigue of concrete.
- (3) The fatigue damage accumulation in cement paste specimens, in the form of nano-scale crack propagation, is very small, even under high stress levels (70-95%). Compared to the static fracture, a higher density of nano-scale cracks can be observed in fatigue fractured samples. Most of these cracks are a result of the fractured C-S-H phases, which are generally found at stress concentrations. This suggests that, under fatigue loading, multiple nano-cracks propagate simultaneously inside the C-S-H gel particles and coalesce into a major crack before failure.
- (4) Three distinct stages of the development of residual deformation can be identified. The residual deformation of cement paste measured at the microscale is not caused only by the growth of fatigue crack. Assuming linear viscoelastic behaviour, the viscoelastic deformation under cyclic loading seems to account for most of the measured residual deformation, especially in the initial stage of fatigue tests. In a later stage, the residual deformation could be explained by coupling of fatigue crack growth and viscoelastic deformation.

The knowledge regarding the fatigue properties of cement paste at the microscale will help to gain insights on the fatigue behaviour of concrete. However, in order to fully understand this behaviour, the fatigue properties of other components in concrete, i.e. ITZ, also need to be studied. The next chapter will focus on the fatigue behaviour of ITZ at the microscale.

## REFERENCES

- [1] T.T.C. Hsu, Fatigue and microcracking of concrete, *Matériaux Constr.* 17 (1984) 51–54.
- [2] L. Gao, C.T.T. Hsu, Fatigue of concrete under uniaxial compression cyclic loading, *ACI Mater. J.* 95 (1998) 575–581.
- [3] T.T.C. Hsu, Fatigue of Plain Concrete, *ACI J. Proc.* 78 (1981) 292–304.
- [4] K.M. Simon, J.M. Chandra Kishen, A multiscale approach for modeling fatigue crack growth in concrete, *Int. J. Fatigue.* 98 (2017) 1–13.
- [5] C. Pichler, R. Lackner, Identification of logarithmic-type creep of calcium-silicate-hydrates by means of nanoindentation, *Strain.* 45 (2009) 17–25.
- [6] K.M.A. Sohel, K. Al-Jabri, M.H. Zhang, J.Y.R. Liew, Flexural fatigue behavior of ultra-lightweight cement composite and high strength lightweight aggregate concrete, *Constr. Build. Mater.* 173 (2018) 90–100.
- [7] J.K. Kim, Y.Y. Kim, Experimental study of the fatigue behavior of high strength concrete, *Cem. Concr. Res.* 26 (1996) 1513–1523.
- [8] Z. Ding, D.C. Feng, X. Ren, J. Wang, Physically based constitutive modeling of concrete fatigue and practical numerical method for cyclic loading simulation, *Eng. Fail. Anal.* 101 (2019) 230–242.
- [9] S. Arora, S.P. Singh, Fatigue strength and failure probability of concrete made with RCA, *Mag. Concr. Res.* 69 (2017) 55–67.
- [10] M.K. Lee, B.I.G. Barr, An overview of the fatigue behaviour of plain and fibre reinforced concrete, *Cem. Concr. Compos.* 26 (2004) 299–305.
- [11] S. Müller, V. Mechtcherine, Fatigue behaviour of strain-hardening cement-based composites (SHCC), *Cem. Concr. Res.* 92 (2017) 75–83.
- [12] J.J. Ortega, G. Ruiz, R.C. Yu, N. Afanador-García, M. Tarifa, E. Poveda, X. Zhang, F. Evangelista, Number of tests and corresponding error in concrete fatigue, *Int. J. Fatigue.* 116 (2018) 210–219.
- [13] J.-L. Le, Z.P. Bažant, Unified nano-mechanics based probabilistic theory of quasibrittle and brittle structures: II. Fatigue crack growth, lifetime and scaling, *J. Mech. Phys. Solids.* 59 (2011) 1322–1337.
- [14] J.-L. Le, Z.P. Bažant, M.Z. Bazant, Unified nano-mechanics based probabilistic theory of quasibrittle and brittle structures: I. Strength, static crack growth, lifetime and scaling, *J. Mech. Phys. Solids.* 59 (2011) 1291–1321.
- [15] J.L. Le, J. Manning, J.F. Labuz, Scaling of fatigue crack growth in rock, *Int. J. Rock Mech. Min. Sci.* 72 (2014) 71–79.
- [16] O.H. Basquin, The exponential law of endurance tests, in: *Proc Am Soc Test Mater*, 1910: pp. 625–630.
- [17] F. Gong, T. Ueda, Y. Wang, D. Zhang, Z. Wang, Mesoscale simulation of fatigue behavior of concrete materials damaged by freeze-thaw cycles, *Constr. Build. Mater.* 144 (2017) 702–716.
- [18] M. Corrado, J.F. Molinari, Effects of residual stresses on the tensile fatigue behavior of concrete, *Cem. Concr. Res.* 89 (2016) 206–219.
- [19] L.P. Guo, A. Carpinteri, R. Roncella, A. Spagnoli, W. Sun, S. Vantadori, Fatigue damage of high performance concrete through a 2D mesoscopic lattice model, *Comput. Mater. Sci.* 44 (2009) 1098–1106.
- [20] K. Matsumoto, Y. Sato, T. Ueda, L. Wang, Mesoscopic analysis of mortar under high-stress creep and low-cycle fatigue loading, *J. Adv. Concr. Technol.* 6 (2008) 337–352.
- [21] K.M. Simon, J.M.C. Kishen, Influence of aggregate bridging on the fatigue behavior of concrete, *Int. J. Fatigue.* 90 (2016) 200–209.

- [22] M. Saito, Characteristics of microcracking in concrete under static and repeated tensile loading, *Cem. Concr. Res.* 17 (1987) 211–218.
- [23] J. Zhang, V.C. Li, H. Stang, Size effect on fatigue in bending of concrete, *J. Mater. Civ. Eng.* 13 (2001) 446–453.
- [24] A. Toumi, A. Bascoul, A. Turatsinze, Crack propagation in concrete subjected to flexural- cyclic loading, *Mater. Struct.* 31 (1998) 451–458.
- [25] F.W. Klaiber, D.Y. Lee, The effects of air content, water-cement ratio, and aggregate type on the flexural fatigue strength of plain concrete, *Am. Concr. Institute, ACI Spec. Publ. SP-075* (1982) 111–131.
- [26] P. Grassl, R. Rempling, A damage-plasticity interface approach to the meso-scale modelling of concrete subjected to cyclic compressive loading, *Eng. Fract. Mech.* 75 (2008) 4804–4818.
- [27] J. Zhang, G.W. Scherer, Comparison of methods for arresting hydration of cement, *Cem. Concr. Res.* 41 (2011) 1024–1036.
- [28] Y. Gan, H. Zhang, B. Šavija, E. Schlangen, K. van Breugel, Static and fatigue tests on cementitious cantilever beams using nanoindenter, *Micromachines.* 9 (2018).
- [29] J.A. Almudaiheem, W. Hansen, Effect of Specimen Size and Shape on Drying Shrinkage of Concrete., *ACI Mater. J.* 84 (1987) 130–135.
- [30] Y. Gan, M. Vandamme, Y. Chen, E. Schlangen, K. van Breugel, B. Šavija, Experimental investigation of the short-term creep recovery of hardened cement paste at micrometre length scale, *Cem. Concr. Res.* 149 (2021).
- [31] Y. Gan, M. Vandamme, H. Zhang, Y. Chen, E. Schlangen, K. van Breugel, B. Šavija, Micro-cantilever testing on the short-term creep behaviour of cement paste at micro-scale, *Cem. Concr. Res.* 134 (2020) 1–26.
- [32] G.R. Cowper, The Shear Coefficient in Timoshenko’s Beam Theory, *J. Appl. Mech.* 33 (1966) 335.
- [33] Y. Gan, M. Vandamme, Y. Chen, E. Schlangen, K. van Breugel, B. Šavija, Experimental investigation of creep recovery of cement paste at the microscale, *Cem. Concr. Res.* (n.d.).
- [34] X. Chen, J. Bu, X. Fan, J. Lu, L. Xu, Effect of loading frequency and stress level on low cycle fatigue behavior of plain concrete in direct tension, *Constr. Build. Mater.* 133 (2017) 367–375.
- [35] M. Saito, H. Ishimori, Chloride permeability of concrete under static and repeated compressive loading, *Cem. Concr. Res.* 25 (1995) 803–808.
- [36] C. Jiang, Q. Huang, X. Gu, W. Zhang, Experimental investigation on carbonation in fatigue-damaged concrete, *Cem. Concr. Res.* 99 (2017) 38–52.
- [37] R.B. Tait, *Fatigue and fracture of cement mortar*, (1984).
- [38] E.O.L. Lantsoght, *Fatigue of concrete under compression: Database and proposal for high strength concrete*, Rep. Nr. 25.5-14-04. (2014).
- [39] M.A. Vicente, D.C. González, J. Mínguez, M.A. Tarifa, G. Ruiz, R. Hindi, Influence of the pore morphology of high strength concrete on its fatigue life, *Int. J. Fatigue.* 112 (2018) 106–116.
- [40] M.A. Vicente, G. Ruiz, D.C. Gonzalez, J. Mínguez, M. Tarifa, X. Zhang, CT-Scan study of crack patterns of fiber-reinforced concrete loaded monotonically and under low-cycle fatigue, *Int. J. Fatigue.* 114 (2018) 138–147.
- [41] H. Zhang, B. Šavija, S.C. Figueiredo, M. Lukovic, E. Schlangen, Microscale testing and modelling of cement paste as basis for multi-scale modelling, *Materials (Basel).* 9 (2016).
- [42] Y. Guang, *Experimental Study and Numerical Simulation of the Development of the Microstructure and Permeability of Cementitious Materials*, 2003.

- [43] Q. Li, B. Huang, S. Xu, B. Zhou, R.C. Yu, Compressive fatigue damage and failure mechanism of fiber reinforced cementitious material with high ductility, *Cem. Concr. Res.* 90 (2016) 174–183.
- [44] B. Zhang, D. V. Phillips, K. Wu, Effects of loading frequency and stress reversal on fatigue life of plain concrete, *Mag. Concr. Res.* 48 (1996) 361–375.
- [45] L. Zhaoxia, H. Yaoping, Effect of strain rate on the compressive strength surface cracking and failure mode of mortar, *ACI Mater. J.* 95 (1998) 512–518.
- [46] I. Fischer, B. Pichler, E. Lach, C. Terner, E. Barraud, F. Britz, Compressive strength of cement paste as a function of loading rate : Experiments and engineering mechanics analysis, *Cem. Concr. Res.* 58 (2014) 186–200.
- [47] Y. Gan, C.R. Rodriguez, E. Schlangen, K. van Breugel, B. Šavija, Assessing strain rate sensitivity of cement paste at the micro-scale through micro-cantilever testing, *Cem. Concr. Compos.* 121 (2021).
- [48] I. Vegt, *Concrete in dynamic tension: the fracture process*, Delft University of Technology, 2016.
- [49] K. Kirane, Z.P. Bazant, Size effect in Paris law and fatigue lifetimes for quasibrittle materials: Modified theory, experiments and micro-modeling, *Int. J. Fatigue.* 83 (2016) 209–220.
- [50] Z.P. Bazant, K. Xu, Size effect in fatigue fracture of concrete, *ACI Mater. J.* 88 (1991) 390–399.
- [51] Z.P. Bazant, W.F. Schell, Fatigue fracture of high-strength concrete and size effect, *ACI Mater. J.* 90 (1993) 472.
- [52] A. Carpinteri, A. Spagnoli, S. Vantadori, An approach to size effect in fatigue of metals using fractal theories, *Fatigue Fract. Eng. Mater. Struct.* 25 (2002) 619–627.
- [53] A. Carpinteri, A. Spagnoli, S. Vantadori, Size effect in S – N curves : A fractal approach to finite-life fatigue strength, *Int. J. Fatigue.* 31 (2009) 927–933.
- [54] A. Carpinteri, A. Spagnoli, A fractal analysis of size effect on fatigue crack growth, *Int. J. Fatigue.* 26 (2004) 125–133.
- [55] A. Carpinteri, A. Spagnoli, S. Vantadori, A multifractal analysis of fatigue crack growth and its application to concrete, *Eng. Fract. Mech.* 77 (2010) 974–984.
- [56] N.K. Raju, *Comparative Study of the Fatigue Behavior of Concrete , Mortar , and Paste in uniaxial compression*, (1970).
- [57] J.D. Antrim, The mechanism of fatigue in cement paste and plain concrete, *A Symp. Concr. Strength; 5 Reports.* (1967) 95–107.
- [58] A. Alliche, D. François, Fatigue behavior of hardened cement paste, *Cem. Concr. Res.* 16 (1986) 199–206.
- [59] A.D. Morris, G.G. Garrett, A comparative study of the static and fatigue behaviour of plain and steel fibre reinforced mortar in compression and direct tension, 3 (1981) 73–91.
- [60] J.W. Murdock, A critical review of research on fatigue of plain concrete, *Univ. Illinois Eng. Exp. Stn. Bull.* (1965) 25.
- [61] N. Oneschkow, Fatigue behaviour of high-strength concrete with respect to strain and stiffness, *Int. J. Fatigue.* 87 (2016) 38–49.
- [62] V. Bindiganavile, N. Banthia, Size effects and the dynamic response of plain concrete, *J. Mater. Civ. Eng.* 18 (2006) 485–491.
- [63] Z.P. Bazant, J. Planas, *Fracture and size effect in concrete and other quasibrittle materials*, CRC press, 1997.
- [64] K. V. Anderson, S.R. Daniewicz, Statistical analysis of the influence of defects on fatigue life using a Gumbel distribution, *Int. J. Fatigue.* 112 (2018) 78–83.
- [65] B. Zhang, Relationship between pore structure and mechanical properties of ordinary

- concrete under bending fatigue, *Cem. Concr. Res.* 28 (1998) 699–711.
- [66] Z. Fan, Y. Sun, Detecting and evaluation of fatigue damage in concrete with industrial computed tomography technology, *Constr. Build. Mater.* 223 (2019) 794–805.
- [67] B. Isojeh, M. El-Zeghayar, F.J. Vecchio, Concrete Damage under Fatigue Loading in Uniaxial Compression, *ACI Mater. J.* 114 (2017).
- [68] M.E. Awad, Strength and deformation characteristics of plain concrete subjected to high repeated and sustained loads, University of Illinois Engineering Experiment Station. College of Engineering. University of Illinois at Urbana-Champaign., 1971.
- [69] Y. Huang, Z. Yang, W. Ren, G. Liu, C. Zhang, 3D meso-scale fracture modelling and validation of concrete based on in-situ X-ray Computed Tomography images using damage plasticity model, *Int. J. Solids Struct.* 67–68 (2015) 340–352.
- [70] Y. Obara, I. Tanikura, J. Jung, R. Shintani, S. Watanabe, Evaluation of Micro-damage of Concrete Specimens under Cyclic Uniaxial Loading by X-ray CT Method, *J. Adv. Concr. Technol.* 14 (2016) 433–443.
- [71] J. Cao, D.D.L. Chung, Minor damage of cement mortar during cyclic compression monitored by electrical resistivity measurement, *Cem. Concr. Res.* 31 (2001) 1519–1521.
- [72] H. Zhang, C.R. Rodriguez, H. Dong, Y. Gan, E. Schlangen, B. Šavija, Elucidating the effect of accelerated carbonation on porosity and mechanical properties of hydrated Portland cement paste using X-ray tomography and advanced micromechanical testing, *Micromachines.* 11 (2020).
- [73] W. Suaris, V. Fernando, Ultrasonic Pulse Attenuation As a Measure of Damage Growth During Cyclic Loading of Concrete., *ACI Mater. J.* 84 (1987) 185–193.
- [74] L. Susmel, A unifying methodology to design un-notched plain and short-fibre/particle reinforced concretes against fatigue, *Int. J. Fatigue.* 61 (2014) 226–243.
- [75] J. Lemaitre, R. Desmorat, Background on continuum damage mechanics, *Eng. Damage Mech. Ductile, Creep, Fatigue Brittle Fail.* (2005) 1–76.
- [76] F.. Leckie, A course on damage mechanics, Springer Science & Business Media, 1998.
- [77] H. Mihashi, F.H. Wittmann, Stochastic Approach To Study the Influence of Rate of Loading on Strength of Concrete., *Heron.* 25 (1980).
- [78] C. Gaedicke, J. Roesler, S. Shah, Fatigue crack growth prediction in concrete slabs, *Int. J. Fatigue.* 31 (2009) 1309–1317.
- [79] Z.P. Bazant, M.H. Hubler, Theory of cyclic creep of concrete based on Paris law for fatigue growth of subcritical microcracks, *J. Mech. Phys. Solids.* 63 (2014) 187–200.
- [80] P. Suwanmaneechot, A. Aili, I. Maruyama, Creep behavior of C-S-H under different drying relative humidities: Interpretation of microindentation tests and sorption measurements by multi-scale analysis, *Cem. Concr. Res.* 132 (2020) 106036.
- [81] M. Wyrzykowski, A.M. Gajewicz-Jaromin, P.J. McDonald, D.J. Dunstan, K.L. Scrivener, P. Lura, Water Redistribution-Microdiffusion in Cement Paste under Mechanical Loading Evidenced by <sup>1</sup>H NMR, *J. Phys. Chem. C.* 123 (2019) 16153–16163.
- [82] R. Alizadeh, J.J. Beaudoin, L. Raki, Viscoelastic nature of calcium silicate hydrate, *Cem. Concr. Compos.* 32 (2010) 369–376.
- [83] M. Vandamme, F.J. Ulm, Nanoindentation investigation of creep properties of calcium silicate hydrates, *Cem. Concr. Res.* 52 (2013) 38–52.
- [84] M.E. Gurtin, E. Sternberg, On the linear theory of viscoelasticity, *Arch. Ration. Mech. Anal.* 7 (1961) 402–411.
- [85] M. Irfan-Ul-Hassan, B. Pichler, R. Reihnsner, C. Hellmich, Elastic and creep properties of young cement paste, as determined from hourly repeated minute-long quasi-static tests, *Cem. Concr. Res.* 82 (2016) 36–49.



- [86] B.T. Tamsia, J.J. Beaudoin, Basic creep of hardened cement paste. A re-examination of the role of water, *Cem. Concr. Res.* 30 (2000) 1465–1475.
- [87] K. Van Breugel, Relaxation of young concrete, (1980) 144.



# 4

## MICROMECHANICAL AND FATIGUE PROPERTIES OF ITZ AT MICROSCALE

*In this chapter the flexural strength and fatigue properties of the interfacial transition zone (ITZ) are experimentally investigated at the microscale. Hardened cement paste cantilevers ( $150\ \mu\text{m} \times 150\ \mu\text{m} \times 750\ \mu\text{m}$ ) attached to a quartzite aggregate surface are prepared and tested under monotonic and cyclic load. The mechanical and fatigue properties of the ITZ are obtained and compared with the results of cement paste specimen (Chapter 3). The microscopic observations on the fracture surfaces are also performed to gain a better understanding of ITZ fracture under different loading conditions. The possible size effect of ITZ bonding strength is examined by comparing it with the macroscopic test results reported in literature. Discussions on the nature of ITZ bonding strength and the fatigue behaviour of ITZ at the microscale are provided.*

## 4.1 INTRODUCTION

Concrete is generally considered as a three-phase composite at the mesoscale (millimeter to centimeter scale), comprising aggregate, cement paste matrix and the interfacial transition zone (ITZ) – a highly porous zone between the aggregate particles and the cement paste matrix. The ITZ plays an important role in the mechanical performance of concrete. Numerous studies have been devoted to the microstructure and the mechanical properties of ITZ [1–6]. The ITZ is generally characterized by a high porosity, deposition of crystals with preferential orientations and fewer cement particles than in the bulk cement matrix. The major origin of this porous ITZ is due to the so-called ‘wall effect’, which disrupts the packing of the cement grains against the relatively flat aggregate surface [1]. Moreover, a water film which forms around aggregate particles in fresh concrete also leads to a higher local w/c ratio in the vicinity of aggregate particles. Another important microstructural feature of ITZ is the excess content of large ettringite (AFt) and calcium hydroxide (CH) crystals with preferential orientations deposited in the vicinity of aggregate, which forms the porous framework of ITZ at the early age of hydration [6]. With ongoing hydration, the remaining space is further filled with calcium silicate hydrate (C-S-H) gel and smaller crystals of AFt and CH.

In general, the porous ITZ is considered to be the weakest link in conventional concretes and is prone to microcracking under loading. Knowledge of the mechanical properties of ITZ is essential for understanding the fracture behaviour of concrete. In the literature, various testing approaches have been developed to investigate the mechanical properties of ITZ [1–7]. While most studies focus on the macroscopic behaviour of ITZ, the typical thickness of the ITZ is at the microscale, i.e. 20–100  $\mu\text{m}$ . Recent application of indentation techniques provide valuable information on the hardness and indentation modulus of the ITZ [8,9]. Unfortunately, the strength of ITZ cannot be measured directly by conventional indentation techniques. This can be overcome by fabricating small cement paste cantilevers attached on the aggregate and performing bending tests with the aid of a nanoindenter, as described in [10]. Zhang et al. [10] performed micro-bending tests on small ITZ cantilever beams with the dimension of  $200 \times 100 \times 100 \mu\text{m}^3$ . The measured load-displacement curves were then used to calibrate and validate the micromechanical model and set the basis for multiscale modelling of mortar. In this study, the method developed by Zhang et al. [10] is modified by increasing the size of specimens to  $750 \times 150 \times 150 \mu\text{m}^3$ , which allows direct measurement of flexural strength of ITZ with negligible shear effect.

Unlike the static mechanical properties, the fatigue properties of ITZ have never been examined directly *at any length scale*. It is known that the fatigue-induced damage may severely affect the macroscopic mechanical properties of concrete [11–13]. The fatigue loading can also cause acceleration of unavoidable ageing phenomena resulting in a decay of performance of a system with elapsed time [14]. Therefore, a clear understanding of fatigue behaviour of ITZ is of great importance for predicting the fatigue of concrete structures. According to fatigue tests of cement paste presented in

Chapter 3, the stiffness degradation of cement paste was very limited, even after a large number of loading cycles. However, the fatigue damage accumulation in concrete is more noticeable [15,16]. This indicates that most of the fatigue damage occurs in the ITZ. Maybe the pre-existing cracks and pores situated in the ITZ promote the development of fatigue cracks in concrete when subjected to cyclic loading [15,16].

This chapter aims to study the flexural strength and fatigue properties of ITZ at the microscale. The miniaturized ITZ specimens are first fabricated using a method similar to that developed by Zhang et al. [10]. The specimens are then subjected to both monotonic and cyclic loading to assess their flexural strength and fatigue properties, respectively. The microscopic observations on the fracture surfaces are also performed to gain a better understanding of the ITZ fracture under different loading conditions. The possible size effect of ITZ bonding strength is examined by comparing measured results with macroscopic test results reported in literature. Discussions on the nature of ITZ bonding strength and the fatigue behaviour of ITZ at the microscale are also provided.

## 4.2 EXPERIMENTAL APPROACH

### 4.2.1 MATERIALS AND SAMPLE PREPARATION

Standard CEM I 42.5 N Portland cement (ENCI, the Netherlands) was mixed with deionized water to prepare the cement pastes. Two w/c ratios (0.3 and 0.4) were used in this study. The Blaine fineness of cement (provided by the manufacturer) is 2840 cm<sup>2</sup>/g. Before sample preparation, a chemically inert quartzite aggregate was cut and ground to obtain a thin slice with the thickness of 1 mm, see Figure 4-1(a). This was achieved by using a Minitom low-speed cutting machine and a Struers Labopol-5 thin sectioning machine, respectively. Both sides of aggregate were ground using two grinding discs with grit sizes of 135 μm and 35 μm in sequence. Each grinding step lasted for about 5 minutes. The prepared aggregate slices were then dried in an oven (60°C) for 48 hours. The surface texture of the aggregate is an important factor affecting the mechanical properties of ITZ [4,17,18]. By means of mechanical interlocking with the aggregate surface at different length scales, the bonding strength of ITZ is higher for rough surface than for a smooth surface [5]. The microscopic mechanical interlocking is mainly caused by the epitaxial growth of cement hydration products (mostly CH and AFt) on the aggregate surface. The surface roughness of the ground aggregate was examined using a digital microscope (Keyence VHX-7000) with a z-axis resolution of 1 μm. The 3D contour map of surface roughness is shown in Figure 4-1(b). Note that the height is calculated using an averaging technique in between two focal lengths. Two areas of 1000 × 1500 μm<sup>2</sup> were examined and the arithmetic mean height ( $S_a$ ) and the root mean square height ( $S_q$ ) are calculated as  $4.5 \pm 0.1$  μm and  $5.6 \pm 0.1$  μm. Clearly, the measured roughness in this study is much lower (almost 1 to 3 orders of magnitude) than the surfaces of natural aggregate and crushed aggregate reported in literature

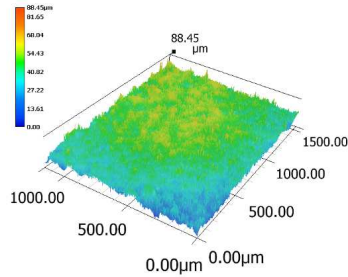
[19,20], but similar to the ground and polished aggregates [7]. In addition, the surfaces of slices were examined by using backscattered electron images (BSE), secondary electron (SE) images and energy dispersive spectrometer (EDS) analysis, see Figure 4-1(c). The accelerating voltage for EDS was chosen at 15 kV. It is confirmed from EDS analysis that the used aggregate mainly contains silica. Therefore, the chemical bonding is not the major source of the bonding strength between the cement paste and aggregate surface in the prepared ITZ sample. However, the electrostatic attraction between solid surfaces could possibly play a role, which will be further discussed in Section 4.2.3. Moreover, it can be seen from SE images of aggregate in Figure 4-1(d) that the typical crystal size of quartz used in current study is around 7~15  $\mu\text{m}$ .

The next step is to cast the fresh cement pastes on the top surface of aggregate slice. Note that the casting procedure also affects the formation of ITZ [21]. The slice needs to be placed at the bottom of the plastic mould in order to avoid possible micro-bleeding effect [22]. The prepared samples were then cured under sealed conditions at room temperature for 28 days.

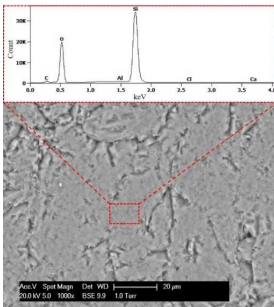
For the fabrication of micro-cantilever beams containing the ITZ, a precision micro-dicing machine (MicroAce Series 3 Dicing Saw) equipped with a resin blade was used. To meet the required cutting depth of this machine, the hardened cement paste-aggregate samples were further ground to reach the total thickness of around 1.75 mm (with approximately 1.00 mm aggregate + 0.75 mm cement paste). For more details regarding the sample preparation, the reader is referred to [10]. Only a brief description is given here: two perpendicular cutting directions with the same cutting spacing were applied on the cement paste side of the sample using the micro-dicing machine. In this way, multiple rows of cement paste cantilever beams with a square cross section of the beam of  $150 \times 150 \mu\text{m}^2$ , which are attached on the aggregate surface, were fabricated. The cutting depth was set to 0.85 mm to ensure that the resin blade has cut into the aggregate. Hence, a clear boundary between the cement paste beam and the aggregate was generated, see Figure 4-2(a). The resin blade may experience some attrition and damage with time especially when cutting into the hard aggregate, which may undermine the quality of cutting. In this case, the replacement of new resin blade is required.



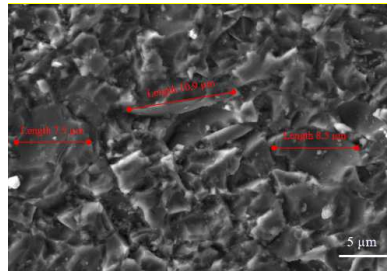
(a) Quartzite aggregate slice



(b) 3D contour map of surface roughness



(c) BSE image and EDS of aggregate surface

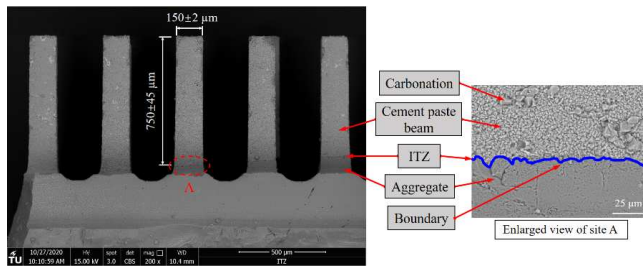


(d) SE image of quartz crystals

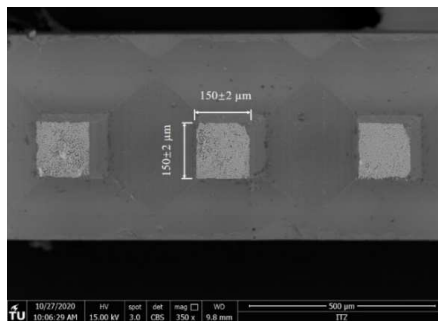
Figure 4-1 (a) A slice of quartzite aggregate with the thickness of around 1 mm; (b) 3D contour map of surface roughness; (c) BSE image and EDS of aggregate surface and (d) SE image of quartz crystals

Note that the number of successfully prepared ITZ bond specimens is lower than that of prepared pure cement paste specimen fabrication. This is mainly because the ITZ is more heterogeneous than the bulk paste and tends to exhibit a larger variation of bond strength, which is in general much lower than the average strength of the bulk paste [10–12,23,24]. Since the ITZ bond specimens will inevitably experience some minor damage and shrinkage during the grinding and cutting procedure, an ITZ beam may be damaged or even fail before testing due to the high local porosity or the presence of shrinkage-induced cracks. Nevertheless, in successfully fabricated ITZ beams, no apparent cracking was observed in cement paste beam or ITZ region as a consequence of the cutting process. An overall accuracy of the cross-sectional dimensions of  $\pm 2 \mu\text{m}$  can be reached with this fabrication process. The distance between the free end of cement paste and the edge of aggregate surface is defined as

the effective cantilever length. In general, it is difficult to obtain a perfectly flat and smooth surface of aggregate with the employed manual grinding procedure. Therefore, a slightly inclined aggregate surface is obtained, see Figure 4-2(b). This results in variations in effective cantilever lengths of the samples. The length of all samples were measured and recorded under the in-situ microscope before testing. Even though precautions were taken to minimize carbonation of the samples by storing the beams in isopropanol [25], the surfaces of the small cement paste beams were slightly carbonated when exposed to the ambient air, as can be seen in Figure 4-2(a). Moreover, a relative rough boundary between the cement paste and aggregate can be observed at the higher magnification. This relatively rough surface at the smaller scale along with the filling of carbonation products in pores could potentially enhance the mechanical interlocking behaviour of ITZ to a certain extent [26].



(a) Side view of ITZ sample



(b) Cross-sections of ITZ sample

Figure 4-2 Backscattered electron images of (a) the side view of ITZ and (b) the cross-sections of ITZ samples with w/c 0.4, 28 days



The microstructures of four ITZ samples were examined using X-ray computed tomography (XCT) [27]. The X-ray source tube was set at 90 kV/170  $\mu$ A during scanning, resulting in a voxel resolution of  $0.5 \times 0.5 \times 0.5 \mu\text{m}^3$ . After acquiring the grey-scale based XCT images, pore segmentation was conducted using the global threshold method [28,29]. The segmented XCT images were used to determine the porosity distribution along the beam. In Figure 4-3, it is clear that the local porosity near the aggregate surface is larger than that of bulk paste [10]. The average porosity of the bulk paste, which is around 150  $\mu\text{m}$  away from the edge of aggregate surface, is detected as  $5.31 \pm 1.08\%$  for two samples with w/c ratio of 0.3. For two samples with w/c 0.4, the average porosity of bulk paste is  $8.42 \pm 1.63\%$ . Note that pores smaller than the image resolution in XCT (i.e. 0.5  $\mu\text{m}$ ) cannot be detected. Therefore, a lower porosity is detected using the XCT compared to the mercury intrusion porosimetry method [30]. It is generally accepted that the ITZ is not a definite zone, but rather a region of transition. The microstructure of ITZ varies with the mix composition, hydration degree and casting procedure, etc [1,21]. Moreover, the local ITZ microstructures around one aggregate particle can significantly differ even in the same concrete sample [1]. Due to the ambiguous boundary with the bulk paste, it becomes extremely difficult to determine the 'average' effective width of ITZ. Therefore, the approximation of ITZ width instead of the accurate quantification of ITZ width is performed here.

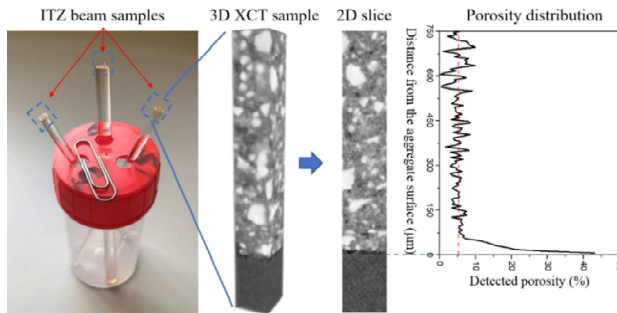


Figure 4-3 The 3D XCT results of w/c 0.3 ITZ beam samples and the detected porosity distribution calculated based on segmented 2D slices

For demonstration, the region of interest (ROI) with a length of 400  $\mu\text{m}$  cement paste + 100  $\mu\text{m}$  aggregate was extracted from the XCT obtained samples, see Figure 4-4. It is found that the changes in porosity in the regions, which are approximately 30-100  $\mu\text{m}$  from the aggregate surface, are most significant. Herein, these regions are roughly considered as the ITZ. It should also be noted that, in some cases, the local porosity in ITZ is even similar to the bulk cement paste. As a result of the so-called wall effect [1,2], the unhydrated cement particles tend to be fewer and smaller in the ITZ.

This effect can also be observed in Figure 4-4. Due to the limited resolution and similar density, other components, such as CH, AFt and monosulfate (AFm), cannot be distinguished from the CT images owing to their densities similar to those of the main hydration product, i.e. C-S-H.

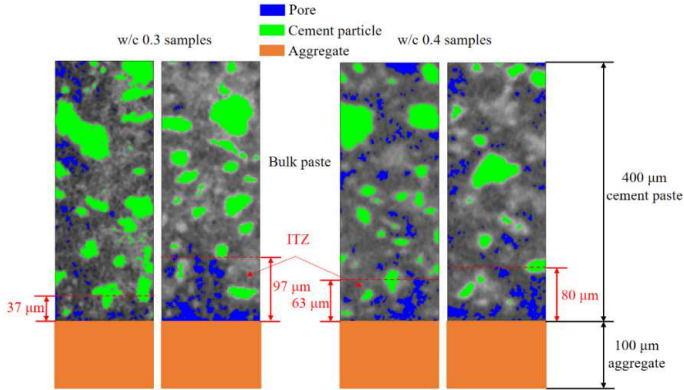


Figure 4-4 The segmented pores and unhydrated cement particles in the ROI of two ITZ samples per w/c ratio (grey represents hydration products)

#### 4.2.2 QUASI-STATIC AND FATIGUE BENDING TEST

Quasi-static and fatigue bending tests were performed on the fabricated ITZ cantilever beams using the same test set-up developed in the previous chapter. A KLA Nano-indenter G200 equipped with a cylindrical wedge indenter tip was used to apply vertical line loads at the free end of the cantilever beams. Before testing, the angle and centre of the indenter tip were calibrated by probing into a standard aluminum reference sample. One side of aggregate was attached on a metal surface using cyanoacrylate adhesive, and the angle of the cement paste beam was carefully adjusted under the in-situ microscope to ensure that the line load is applied perpendicular to the longitudinal axis of the beam. The experimental set-up is schematically shown in Figure 4-5. For each test, the coordinates of the loading position and the edge of aggregate surface were recorded under the microscope to determine the loading distance  $d$ , see Figure 4-5. All tests were conducted in a well-insulated chamber preventing any significant change of temperature and RH. The average temperature and RH during the tests were  $26.5 \pm 0.5$  °C and  $34.1\% \pm 0.8\%$ , respectively. Prior to the tests, the samples were kept in the chamber for temperature equalization until the thermal drift rate was below 0.05 nm/s.

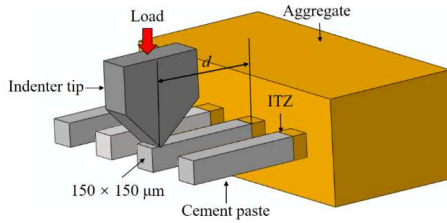


Figure 4-5 Schematic diagram of test set-up ( $d$  is the distance between the load point and the boundary of the aggregate)

### QUASI-STATIC BENDING TEST

The static mechanical properties of ITZ cantilever beams, i.e. flexural strength and static elastic modulus, were determined before performing fatigue tests. For each w/c ratio, 20 cantilever beams were monotonically loaded to failure. The static test was displacement-controlled with a constant loading rate of 50 nm/s. The measured load-displacement curves for two w/c ratios are shown in Figure 4-6. Generally, these curves can be divided into two parts: the pre-peak region and the catastrophic failure region. In the pre-peak region, the load increases with the displacement until a critical load is reached. Despite some discontinuities, the pre-peak load-displacement curve is almost linear. Afterwards, a rapid burst of displacement is observed due to the catastrophic failure of the specimen. This is probably because the nanoindenter is not fast enough to capture the post-peak behaviour of the specimen and the ITZ sample is intrinsically brittle.

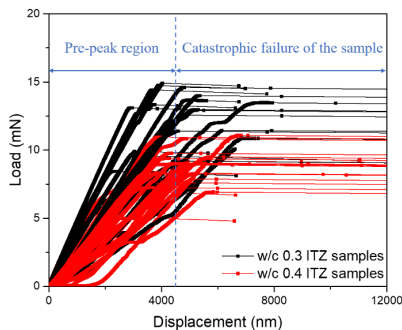


Figure 4-6 Load-displacement curves for ITZ samples with two w/c ratios

In order to determine the flexural strength  $f_t$  and static elastic modulus  $E_{\text{static}}$  of the ITZ sample, the maximum static load  $P_{\text{max}}$  and the loading slope of the load-displacement curve  $k$  (in the loading range between 40% and 60% of the maximum load) are used according to the classical beam theory [12,23,31]:

$$f_t = \frac{P_{\text{max}}dh}{2I} \quad (4-1)$$

$$E_{\text{static}} = \frac{kd^3}{3I} \quad (4-2)$$

where  $d$  is the measured effective cantilever length,  $h$  is the side length of the square beam cross-section, and  $I=h^4/12$  is the moment of inertia. After failure of the sample, the fracture location is examined to check whether the fracture occurs at the ITZ region. The fractured surfaces of specimens on the aggregate side were also examined using the scanning electron microscope.

#### FATIGUE BENDING TEST

Fatigue flexural tests of ITZ samples were carried out under load control. In total 15 ITZ specimens for each w/c ratio were tested under different cyclic loading ranges (maximum fatigue force  $F_{\text{max}}$  and minimum force  $F_{\text{min}}$ ). The cyclic load was applied with a constant amplitude ( $F_{\text{max}} - F_{\text{min}}$ ) at a loading frequency of 0.55 Hz, the same as in Chapter 3. The loading protocol is schematically shown in Figure 4-7. The pattern of cyclic loading controlled by the nano-indenter is approximately a triangular load, but with a very short dwelling time (0.2 s) at the maximum and minimum loads. The corresponding maximum flexural stress at the upper fibre of the ITZ sample under the maximum fatigue force was calculated using Eq.(4-1). Note that even under the same magnitude of the load the calculated stress may be different due to the small variation of the effective cantilever length. The corrected maximum stress level  $S$  ( $\sigma_{\text{max}}/f_t$ ) for the fatigue test varies between 60% and 90% of the static flexural strength for both w/c ratios. At the same time, the minimum stress level for fatigue stress ratio  $R$  ( $\sigma_{\text{min}}/\sigma_{\text{max}}$ ) was maintained at a constant level of 0.07 throughout the test. The number of loading cycles at failure of the specimen was denoted as the fatigue life,  $N$ . During the fast loading-unloading regime, small disturbances (2-5% of loading amplitude) for both maximum and minimum fatigue load may occur. Therefore, the recorded average load level was used to determine the stress level. Before each fatigue test, the ITZ sample was preloaded to the maximum load and completely unloaded to reduce the possible plastic deformation generated under the indenter tip [11].

Due to the limited test duration in the nano-indenter, the fatigue loading protocol was separated into multiple cycle blocks with identical load history. Each cycle block contains 500 loading-unloading cycles. Two cycle blocks are connected with a short rest period (around several minutes), see Figure 4-7. The beam is completely unloaded after finishing one cycle block and then reloaded for the next cycle block, as shown Figure 4-

8. The so-called run-out tests are stopped at the limit of 200,000 cycles. At the end of each fatigue test, the nano-indenter will apply a constant low load at around 0.01% of the maximum load to measure the drift rate and calibrate the displacement responses. However, most of the measured drift may be affected by creep recovery because of the viscoelastic nature of cement paste [32]. Therefore, the calculated drifts were deducted from the total time-dependent displacements.

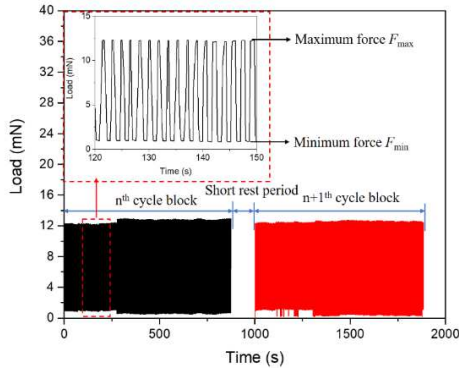


Figure 4-7 Illustration of cyclic load history applied in MCB fatigue tests

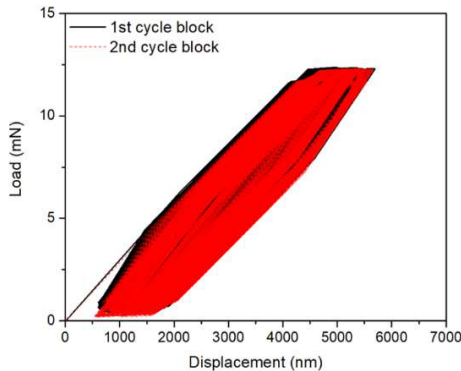


Figure 4-8 Examples of load-displacement curves for two cycle blocks

Two major characteristics of fatigue of cementitious materials are the evolution of residual deformations and sample stiffness [11]. A MATLAB code was developed to extract both quantities from the recorded load-displacement curve in each cycle block.

Figure 4-9 illustrates the calculation of residual deformation and loading stiffness during the fatigue test. The load amplitude and the displacement during the loading stage  $\delta_{load}$  were used to determine the stiffness of sample at the  $i$ -th cycle. The residual displacement  $\delta_{res}$  is defined as the change of displacement at the maximum load level relative to the corresponding displacement at the first cycle. The corresponding residual strain is calculated as the strain  $\epsilon(t)$  at the upper fibre of the fixed end of the beam based on the classical beam theory [31]. The fatigue compliance  $C(t)$  is determined by dividing the residual strain by half of the applied maximum stress ( $\sigma_{max}/2$ ). For each ITZ specimen, the residual strain and the corresponding fatigue compliance were calculated according to the Eq.(3-3) and Eq.(3-4).

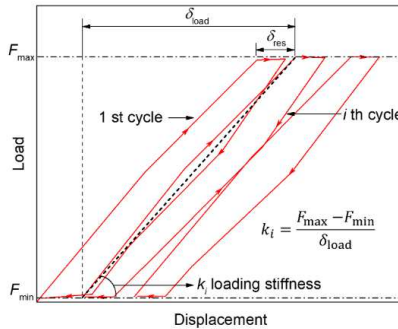


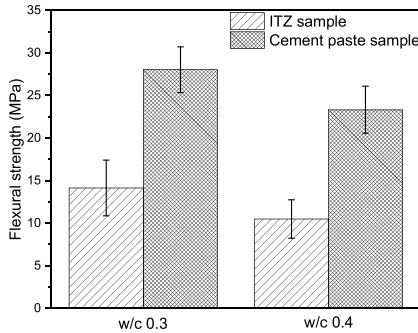
Figure 4-9 Illustration of residual displacement and loading stiffness calculation

### 4.3 EXPERIMENTAL RESULTS AND DISCUSSION

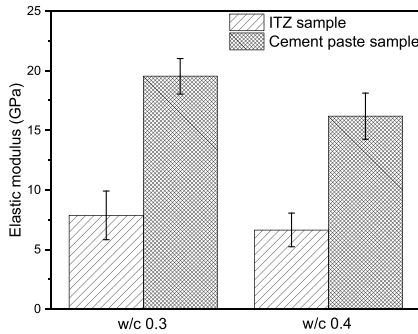
#### 4.3.1 MECHANICAL PROPERTIES MEASURED IN QUASI-STATIC TESTS

Figure 4-10 shows the flexural strength and elastic modulus of ITZ samples. In general, the mechanical properties increase with the decreasing  $w/c$  ratio. For comparison, flexural strengths and elastic moduli of cantilever beams made of pure cement paste (28 days) at similar length scale ( $300 \times 300 \times 1650 \mu\text{m}^3$ ) in Chapter 3 and Ref.[33] are also presented in Figure 4-10. As is expected, the mechanical properties of ITZ samples are lower than that of pure cement paste samples, mainly due to the higher porosity of the ITZ. The average flexural strength of ITZ samples for both  $w/c$  ratios is approximately 44-50% of the paste matrix, while the elastic modulus is around 40-41%. However, there are large variations of flexural strength and elastic modulus indicated by the calculated coefficient of variation i.e. 21-25% for both  $w/c$  ratios. Note that the average flexural strength of the microscopic ITZ specimen is significantly higher than

the bonding strength (0.75-3.9 MPa) of macroscopic laboratory-scale specimens [3,4,34]. This aspect is further discussed in Section 4.2.6.



(a) Flexural strength



(b) Elastic modulus

Figure 4-10 The comparison of (a) the flexural strength and (b) elastic modulus of ITZ sample (28 d) and the cement paste sample obtained in [23]

### 4.3.2 FATIGUE PROPERTIES

The relationship between the fatigue life  $N$  of ITZ specimens and the stress level  $S$  is plotted in Figure 4-11. For comparison, the fatigue results of cement paste beams in Chapter 3 were also included. The figure shows that the fatigue life data exhibit a considerable scatter, which is typical for fatigue tests [35]. Consequently, a clear trend for the  $S$ - $N$  relation is difficult to be discerned for any of the investigated w/c ratios. The

observed scatter of fatigue results may arise from the microstructural heterogeneity of the material, the variation in specimen size, as well as assumptions made in the fatigue analysis [11]. During most of the fatigue life, the fatigue fracture is characterized by diffuse microcracking. Instead of instantly turning to the localization of microcracking, the fatigue microcracks gradually propagate at numerous randomly distributed weak spots, e.g. pores and pre-existing cracks [13]. Therefore, the moment of final fatigue fracture depends on a series of time-dependent processes during the loading and unloading cycles. These processes could be related to the stress redistribution, friction process, shrinkage, self-healing and ageing, etc. This is completely different from the static fracture and could also be the reason for the pronounced scatter observed in fatigue data. Nevertheless, it is clear from Figure 4-11 that the fatigue strengths of ITZ specimens for both w/c ratios are apparently lower than the strength of pure cement paste beams at the microscale. This indicates that the ITZ is more vulnerable to the fatigue loading and is most likely to provide locations promoting crack propagation in concrete, which is in accordance with the findings reported in [15,16]. To the best of the authors' knowledge, there is currently no available data for the direct fatigue testing of the ITZ, either at the microscale or the macroscale. Therefore, the possible size effect on the fatigue of ITZ cannot be verified here. Further studies on the macroscopic fatigue behaviour of ITZ are needed.

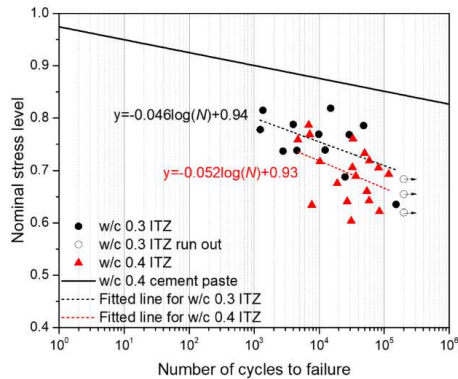


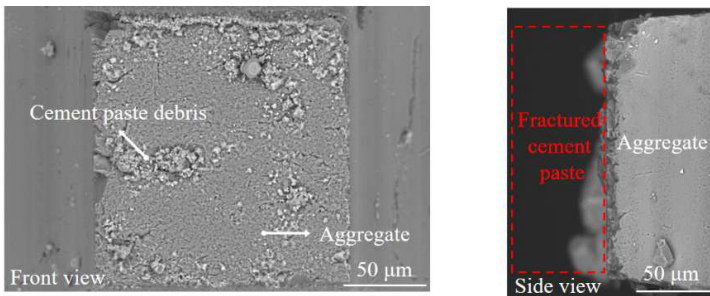
Figure 4-11 The  $S-N$  curves for ITZ samples and the comparison with the results of pure cement paste samples

### 4.3.3 FRACTURE SURFACE

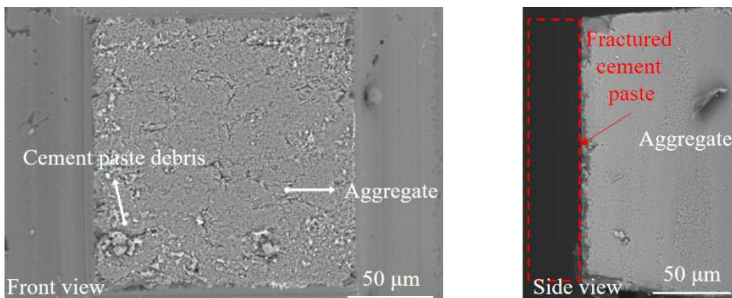
In general, the fracture occurs at the ITZ of the specimen regardless of the loading protocol, i.e. both in static and fatigue conditions. Figure 4-12(a) and (b) show the front and side views of several fractured surfaces of ITZ specimens under monotonic and



cyclic loading, respectively. No apparent difference between the static and fatigue fractures is found as the critical crack always occurs at the interfacial zone. It should also be noted that the fracture surface might be different from case to case, reflecting the high heterogeneity of the ITZ. One common characteristic for some fracture surfaces is that the cement paste beam including the ITZ is completely detached from the aggregate surface except for a few remaining cement paste debris. This indicates that the major part of the critical crack is formed along the surface of the aggregate and only a small portion of the cracking path penetrates into the ITZ. This failure mode is mainly caused by the weak bond between the hydration products and the aggregate.



(a) Fractured ITZ samples subjected to static loading



(b) Fractured ITZ samples subjected to cyclic loading

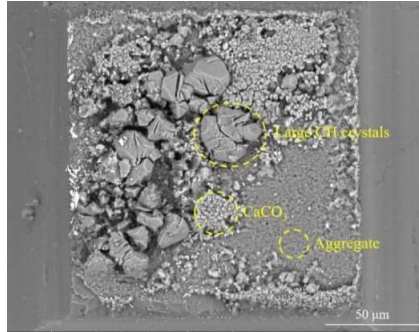
Figure 4-12 The front views and side views of fractured ITZ samples subjected to (a) monotonic loading and (b) cyclic loading

Another failure mode is observed in some fractured beams, as shown in Figure 4-13(a). The major part of the critical crack passes through the porous ITZ and exposes a

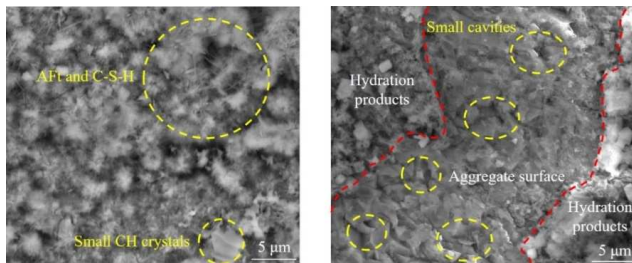
lot of debris on the aggregate surface. The debris mainly consist of amorphous C-S-H gel, CH crystals and some calcium carbonate ( $\text{CaCO}_3$ ) cubes formed after the air exposure of the fractured surface. In addition, some minor ettringite (AFt) needles are detected on the aggregate surface. It can be seen in Figure 4-13(a) that some large CH crystals (around 10-40  $\mu\text{m}$ ) with preferential orientations are anchored in the aggregate surface and surrounded by other hydration products. Similar observations have also been reported in [2,36]. Note that the preferential orientation of large CH crystal plates may result in different behaviours for direct tensile and flexural tests.

It is suggested by several researchers [8,27] that the epitaxial growth of hydration products (e.g. CH and AFt) and their precipitation in small cavities on the aggregate surface, e.g. Figure 4-13(b), contribute to the mechanical interlocking effect. This mechanical interlocking effect can be observed at different length scales depending on the roughness of the aggregate surface. Figure 4-13(c) illustrates the microscopic mechanical interlock mechanism at the ground aggregate surface. Even though the aggregate has been ground to a certain extent, numerous cavities remain on the surface and facilitate the deposition of hydration products. Zimbelmann [4] suggested that the transfer of load from the cement paste to the aggregate is mainly done by the anchored CH crystals and, to a smaller extent, by the AFt and C-S-H. It is also believed that large CH crystals formed in the highly porous ITZ would favour the formation and propagation of microcracks under mechanical load [37,38]. It is clear that the ITZ contains more CH compared to the bulk paste, but the distribution of CH is not connected around the aggregate surface, especially in real concrete samples [2]. This highly heterogeneous microstructure further complicates the fracture behaviour of ITZ at the microscale.

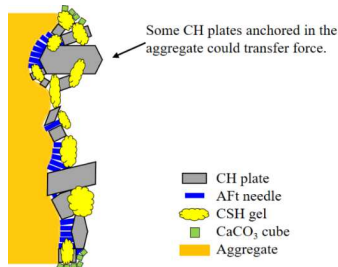
Besides this mechanical effect, the relatively weak electrostatic interaction between reaction products and aggregate could also play a role in developing the bond strength [39,40]. With reference to the zeta-potential measurements and microscopic observations, Ouyang et al. [39] suggested that the adhesion mechanism between C-S-H particles and silicate filler is driven by an attractive ion-ion force. Since the C-S-H and silicate particles have similar surface charge properties, the electric interaction between the C-S-H surface and the silicate surface is similar to that between two C-S-H surfaces. The ion-ion correlations between C-S-H particles have been confirmed in the molecular dynamics simulations and direct-force measurements by atomic force microscopy [41,42]. The authors [39] suggested that two surfaces (silica and C-S-H) are separated by a dielectric continuum, in which  $\text{Ca}^{2+}$  ions are free to move. The attractive ion-ion correlation force is generated due to the charges of the excess of  $\text{Ca}^{2+}$  ions on one side resulting in an overall positive charge, and the deficit on the other side resulting in an overall negative charge. It can be seen in Figure 4-13(b) that many C-S-H particles directly precipitate on the aggregate surface. Moreover, this electrostatic interaction effect on the bonding strength may be different for other crystal phases on the aggregate surface. Therefore, in addition to the distribution of pores, the deposition of different hydration products may also affect the final failure mode.



(a) Fracture surface after static failure



(b) Images of hydration products and small cavities



(c) Schematic presentation of the hydration products distribution on the aggregate surface

Figure 4-13 (a) Some large CH crystals with preferred orientation observed on the aggregate surface after static fracture; (b) the images of hydration products and small cavities at higher magnifications and (c) schematic presentation of the hydration products distribution on the aggregate surface (Note that the sketch is used for illustration purposes only and the shape and sizes of hydration products are not exact)

### 4.3.4 RESIDUAL DEFORMATION

The measured residual displacement curves for different w/c ratio specimens are shown in Figure 4-14. There are large variations in these curves, mainly due to the microstructural heterogeneity. In general, the curves can be divided into two stages: the initial stage and the subsequent stable stage. In the initial stage, the residual deformation increases with a decreasing rate and then reaches to the stable stage with a constant growth rate. Before the fatigue failure, the evolution curves increase sharply within a few cycles. The fatigue compliance evolutions in the first two stages are calculated based on Eq.(3-4) and shown in Figure 4-15. The average fatigue compliance seems to increase with increasing w/c ratio. It is suggested that the residual deformation in cement paste is mainly caused by the fatigue crack growth and the viscoelastic nature of C-S-H [11]. By increasing the w/c ratio, the porosity and the probability of drying shrinkage-induced cracking also increase [44]. Therefore, the fatigue crack growth of the pre-existing microcrack as well as the creep deformation increase in higher w/c ratio ITZ and cement paste samples [15,29]. Figure 4-15 also shows a comparison of the fatigue compliance evolution between the ITZ and cement paste test results. It appears that for the same w/c ratio (0.4), the fatigue compliance of the ITZ specimen is slightly higher than that of pure cement paste specimen, which could mainly be explained by the higher local porosity and microcrack density. Note that the viscoelastic deformation may be affected by the relatively higher amount of non-creeping CH crystals in the local area of ITZ specimens [38]. These two deformation mechanisms observed in fatigue tests are very complicated and, therefore, they are mostly treated separately without considering their coupled effects [13,45]. Neville and Hirst [46] indicated that cyclic creep can be considered as an accelerated and irrecoverable static creep. The acceleration effect is explained using Ruetz's model [47]. In that model the applied cyclic stress would disrupt the movement of the adsorbed water layer in C-S-H gel and thus promote the creep deformation. However, the creep effect on the fatigue cracking behaviour is still not clearly understood and should be further investigated.

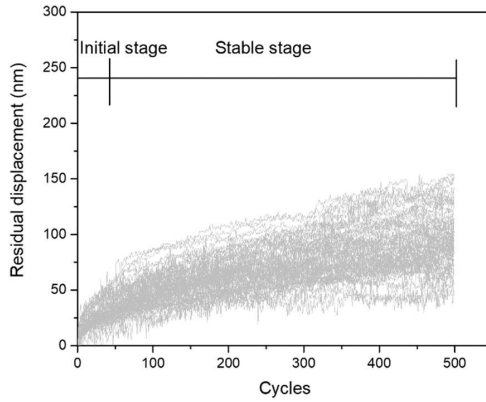
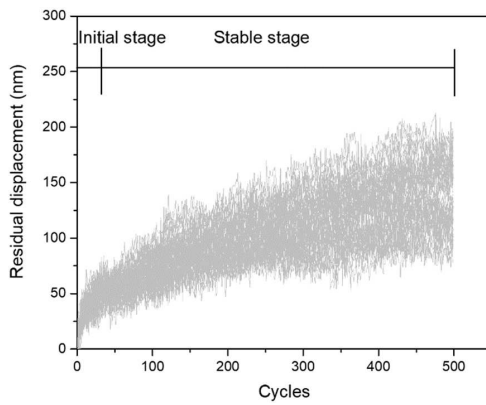
(a)  $w/c = 0.3$ (b)  $w/c = 0.4$ 

Figure 4-14 The evolution curves of residual displacement for (a)  $w/c = 0.3$  and (b)  $w/c = 0.4$  ITZ specimens

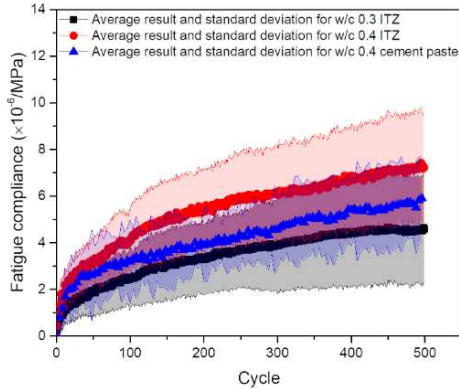
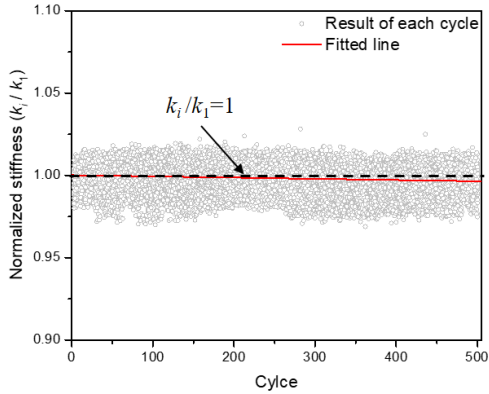


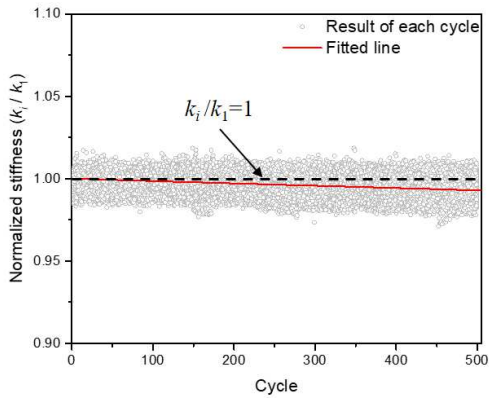
Figure 4-15 Comparison of fatigue compliance curves for ITZ and cement paste specimens from Chapter 3

#### 4.3.5 STIFFNESS VARIATION

The normalized loading stiffness evolutions of ITZ specimens are examined and presented in Figure 4-16 and Figure 4-17. It can be seen in Figure 4-16 that the change of stiffness with increasing number of cycles is very small. However, at the final cycle block of the test, see Figure 4-17, the loading stiffness of beams decreased fast in a few cycles before failure. It is worth mentioning that in some fatigue tests the loading stiffness was almost constant and even some slight increases were also observed. Similar observations have also been reported in literature [48,49]. This may indicate some possible strengthening mechanisms during the fatigue tests, such as carbonation [26], consolidation or compaction of cement paste or the relief of eigenstress in the regions surrounding the cracks under cyclic loading [50]. The stiffness degradation of microscopic ITZ specimens seems to be slow and limited, which is similar to the findings for cement pastes in Chapter 3. When a critical crack is formed as a result of the propagation and coalescence of multiple nano-scale cracks, a sudden fatigue failure occurs. In comparison to the pure cement paste specimens, the extent of damage needed for fatigue failure is much less in ITZ specimens than in cement paste specimen, as indicated by the lower fatigue strength (Figure 4-11). Due to the higher porosity and density of microcracking in the ITZ region of ITZ samples, the formation and propagation of the critical fatigue crack is easier.



(a) w/c 0.3



(b) w/c 0.4

Figure 4-16 The evolutions of normalized stiffness during multiple cycle blocks for (a) w/c 0.3 ITZ samples, and (b) w/c 0.4 ITZ samples. Note that the  $k_1$  is the loading stiffness of the first cycle in a cycle block and  $k_i$  is the  $i$ -th cycle loading stiffness

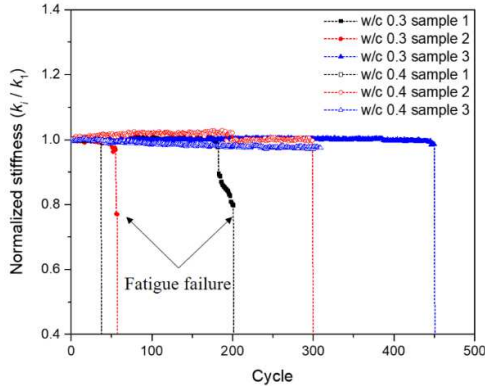


Figure 4-17 Normalized stiffness evolution at the final cycle block

#### 4.3.6 GENERAL DISCUSSION

It is well known that the strength of quasi-brittle materials is size-dependent [51]. The flexural strength of the ITZ (10.49-14.15 MPa) obtained in this study is significantly higher than the bond strengths measured in conventional laboratory-scale samples using polished aggregate. For instance, Hsu and Slate [52] found that the bond strengths between polished aggregates (sandstone and granite) and cement pastes (w/c 0.265-0.36, age 30 d) were only 1.54-2.39 MPa, which is about 40-61% of the tensile strength of cement matrix. Similar results have also been found in the work of Jebli et al. [5], in which the bond strength (around 1.6 MPa) is around 60% of the strength of bulk paste (w/c 0.5, age 28 d). A relatively high tensile bond strength of around 2.3-3.9 MPa between ground quartzite aggregate surface ( $R_a=3.0\ \mu\text{m}$ ) and cement paste (w/c 0.37, age 26-28 d) has also been found in an experimental study conducted by Tasong et al. [3,7]. Furthermore, these authors also tested the bond strength of ITZ specimen using much higher surface roughness aggregates (e.g. fractured surfaces with  $R_a$  equals to 103.8  $\mu\text{m}$ ), which is around 3.25 MPa. Zimbelmann [4], on the contrary, observed a much lower bond strength (around 0.75 MPa) between the polished quartz and the cement paste (w/c 0.35, age 28 d), which is only 16% of the tensile strength of bulk paste. Gu et al. [53] also examined the bond strength between the aggregate and mortar (w/c 0.4) using similar surface roughness ( $R_a=2.3-4.7\ \mu\text{m}$ ) and found that the bond strength was around 1.9 MPa. It is worth mentioning that the strength of ITZ also depends on how the sample is prepared. The shrinkage of the paste, which might introduce eigenstresses in the ITZ [54], could be relieved to a certain extent if the ITZ specimen is cut from a larger sample as in this study. Slightly different strength may be obtained if the ITZ sample is directly cast in the mold, e.g. in [3,7,52]. Despite the small differences in the size of macroscopic specimens (i.e. centimeter sized) and mix



composition, the bond strength of ITZ reported in the literature is almost one order of magnitude lower than the measured flexural strength of ITZ at the microscale.

It is interesting to note that similar size effect in the splitting strength of cement paste measured on paste cubes with a size range from 0.1 to 40 mm has also been studied experimentally by Zhang et al. [55]. They found that the average splitting strength of a micro-cube (100  $\mu\text{m}$ ) sample is also one order of magnitude larger than the strength of the laboratory (40 mm) cement paste sample [55]. Even though the compositions and microstructures of ITZ and bulk cement paste are different, they both exhibit similar quasi-brittle fracture behaviour to some extent. Moreover, large capillary pores and air voids that are equivalent to or larger than the dimension of the ITZ specimen are completely excluded during the cutting process. Hence, the significantly higher flexural strength of ITZ measured at the microscale seems reasonable.

It is worth mentioning that the success ratio of preparing the miniaturized ITZ sample is lower than that of pure cement paste sample, mainly due to the weak bonding strength. As a result, there could be possible *survival bias* in the measured strength as the remaining samples subjected to the destructive cutting and grinding process would originally exhibit stronger bonding properties, while the weak samples with high local porosities or shrinkage-induced cracks would have been eliminated during the sample preparation process. Therefore, the obtained 'average' results may not be fully representative for the true mechanical and fatigue properties. More advanced and nondestructive experimental techniques may be needed. One should always be careful when interpreting the testing results of ITZ specimens, especially considering the strong microstructural heterogeneity at the microscale.

It is clear that the ITZ is the weakest link in ordinary concrete [6]. The much lower strength and lower fatigue resistance of ITZ promote the development of multiple microcracking in concrete samples under monotonic and cyclic loading. However, to further investigate the effect of local ITZ properties on the macroscopic performance of concrete, a multi-scale modelling approach is required. All mesoscopic features, such as aggregate shape, ITZ and paste matrix properties, should be considered to provide a reliable quantitative prediction. The measured ITZ properties in this study could serve as the important basis for the multiscale modelling scheme [13,56].

#### 4.4 CONCLUSIONS

In this chapter, the flexural mechanical and fatigue properties of ITZ were investigated for the first time at the micrometre length scale using micro-cantilever ITZ specimens. The flexural strength of ITZ obtained in current study was compared with results in literature. The following conclusions can be drawn:

- (1) The strength of ITZ at the micrometre length scale is almost one order of magnitude higher than that of centimeter sized specimens in macroscopic tests

reported in literature. In addition, the measured mechanical properties of ITZ, i.e. the strength and stiffness, are much lower than that of bulk cement paste at similar length scale. The flexural strength of ITZ is around 44-50% of the cement paste, while the elastic modulus is around 40-41%.

- (2) The origin of the bond strength between siliceous aggregate and cement paste is discussed. From experimental results it is inferred that the mechanical interlocking at different length scales helps to transfer load. Besides, the electrostatic interaction effect is assumed to play a role in contributing the bond strength.
- (3) A lower fatigue resistance was observed for ITZ compared to that of bulk cement paste. This may indicate that, when the concrete is subjected to the cyclic loading, multiple microcracks accumulate preferably in the ITZ and then coalesce with the cracks in paste matrix leading to the fatigue failure. Relatively higher fatigue residual deformation has been observed in ITZ tests than in tests on cement paste samples with the same w/c ratios and ages. The complex residual deformation development is believed to be caused by the combined effect of creep and fatigue crack propagation. However, their coupled effects remain unclear and need further investigation.

Both the static and the fatigue properties of ITZ investigated at the microscale are useful for the validation of the microscopic model, which can be further used in the multiscale modelling scheme to predict the fatigue fracture behaviour of concrete at the macroscale. A numerical approach will be developed in the next chapter to simulate the fatigue behaviour of cementitious materials.

## REFERENCES

- [1] K.L. Scrivener, A.K. Crumbie, P. Laugesen, The interfacial transition zone (ITZ) between cement paste and aggregate in concrete, *Interface Sci.* 12 (2004) 411–421.
- [2] S. Diamond, J. Huang, The ITZ in concrete - A different view based on image analysis and SEM observations, *Cem. Concr. Compos.* 23 (2001) 179–188.
- [3] W.A. Tasong, C.J. Lynsdale, J.C. Cripps, Aggregate-cement paste interface Part I. Influence of aggregate geochemistry, *Cem. Concr. Res.* 28 (1998) 1453–1465.
- [4] R. Zimbelmann, A contribution to the problem of cement-aggregate bond, *Cem. Concr. Res.* 15 (1985) 801–808.
- [5] M. Jebli, F. Jamin, E. Malachanne, E. Garcia-Diaz, M.S. El Youssoufi, Experimental characterization of mechanical properties of the cement-aggregate interface in concrete, *Constr. Build. Mater.* 161 (2018) 16–25.
- [6] K. Wu, H. Shi, L. Xu, G. Ye, G. De Schutter, Microstructural characterization of ITZ in blended cement concretes and its relation to transport properties, *Cem. Concr. Res.* 79 (2016) 243–256.
- [7] W.A. Tasong, C.J. Lynsdale, J.C. Cripps, Aggregate-cement paste interface. II: Influence of aggregate physical properties, *Cem. Concr. Res.* 28 (1998) 1453–1465.
- [8] I.F. Sáez del Bosque, W. Zhu, T. Howind, A. Matías, M.I. Sánchez de Rojas, C. Medina, Properties of interfacial transition zones (ITZs) in concrete containing recycled mixed aggregate, *Cem. Concr. Compos.* 81 (2017) 25–34.
- [9] J. Xiao, W. Li, Z. Sun, D.A. Lange, S.P. Shah, Properties of interfacial transition zones in recycled aggregate concrete tested by nanoindentation, *Cem. Concr. Compos.* 37 (2013) 276–292.
- [10] H. Zhang, Y. Gan, Y. Xu, S. Zhang, E. Schlangen, B. Šavija, Experimentally informed fracture modelling of interfacial transition zone at micro-scale, *Cem. Concr. Compos.* 104 (2019).
- [11] Y. Gan, H. Zhang, Y. Zhang, Y. Xu, E. Schlangen, K. van Breugel, B. Šavija, Experimental study of flexural fatigue behaviour of cement paste at the microscale, *Int. J. Fatigue.* 151 (2021).
- [12] Y. Gan, H. Zhang, B. Šavija, E. Schlangen, K. van Breugel, Static and fatigue tests on cementitious cantilever beams using nanoindenter, *Micromachines.* 9 (2018).
- [13] Y. Gan, H. Zhang, M. Liang, E. Schlangen, K. van Breugel, B. Šavija, A numerical study of fatigue of hardened cement paste at the microscale, *Int. J. Fatigue.* 151 (2021) 106401.
- [14] K. van Breugel, D. Koleva, T. van Beek, *The ageing of materials and structures: Towards scientific solutions for the ageing of our assets*, 2017.
- [15] A. Toumi, A. Bascoul, A. Turatsinze, Crack propagation in concrete subjected to flexural- cyclic loading, *Mater. Struct.* 31 (1998) 451–458.
- [16] M. Saito, Characteristics of microcracking in concrete under static and repeated tensile loading, *Cem. Concr. Res.* 17 (1987) 211–218.
- [17] T. Akçaoğlu, M. Tokyay, T. Çelik, Effect of coarse aggregate size and matrix quality on ITZ and failure behavior of concrete under uniaxial compression, *Cem. Concr. Compos.* 26 (2004) 633–638.
- [18] P.J.M. Monteiro, J.C. Maso, J.P. Ollivier, The aggregate-mortar interface, *Cem. Concr. Res.* 15 (1985) 953–958.
- [19] P.H.F. Loz, J.P. Monticelli, M.M. Futai, E. Tutumluer, D.A. Lange, S.C. Angulo, Roughness of natural aggregates by interferometry and its microstructure, *Constr. Build. Mater.* 297 (2021) 123646.
- [20] S. Caliskan, B. Karihaloo, Effect of surface roughness, type and size of model

- aggregates on the bond strength of aggregate / mortar, *Interface Sci.* 12 (2004) 361–374.
- [21] Y. Gao, G. De Schutter, G. Ye, Z. Tan, K. Wu, The ITZ microstructure, thickness and porosity in blended cementitious composite: Effects of curing age, water to binder ratio and aggregate content, *Compos. Part B Eng.* 60 (2014) 1–13.
- [22] K.L. Scrivener, P.L. Pratt, Quantitative characterization of the transition zone in high strength concretes, 1 (1988).
- [23] Y. Gan, M. Vandamme, H. Zhang, Y. Chen, E. Schlangen, K. van Breugel, B. Šavija, Micro-cantilever testing on the short-term creep behaviour of cement paste at micro-scale, *Cem. Concr. Res.* 134 (2020) 1–26.
- [24] H. Zhang, B. Šavija, E. Schlangen, Combined experimental and numerical study on micro-cube indentation splitting test of cement paste, *Eng. Fract. Mech.* 199 (2018) 773–786.
- [25] J. Zhang, G.W. Scherer, Comparison of methods for arresting hydration of cement, *Cem. Concr. Res.* 41 (2011) 1024–1036.
- [26] H. Zhang, C.R. Rodriguez, H. Dong, Y. Gan, E. Schlangen, B. Šavija, Elucidating the effect of accelerated carbonation on porosity and mechanical properties of hydrated Portland cement paste using X-ray tomography and advanced micromechanical testing, *Micromachines*. 11 (2020).
- [27] M.A. Vicente, D.C. González, J. Mínguez, M.A. Tarifa, G. Ruiz, R. Hindi, Influence of the pore morphology of high strength concrete on its fatigue life, *Int. J. Fatigue*. 112 (2018) 106–116.
- [28] H. Zhang, B. Šavija, S.C. Figueiredo, M. Lukovic, E. Schlangen, Microscale testing and modelling of cement paste as basis for multi-scale modelling, *Materials (Basel)*. 9 (2016).
- [29] Y. Gan, C. Romero Rodriguez, H. Zhang, E. Schlangen, K. van Breugel, B. Šavija, Modeling of microstructural effects on the creep of hardened cement paste using an experimentally informed lattice model, *Comput. Civ. Infrastruct. Eng.* 36 (2021) 560–576.
- [30] G. Ye, Experimental study and numerical simulation of the development of the microstructure and permeability of cementitious materials, (2003).
- [31] G.R. Cowper, The Shear Coefficient in Timoshenko's Beam Theory, *J. Appl. Mech.* 33 (1966) 335.
- [32] Y. Gan, M. Vandamme, Y. Chen, E. Schlangen, K. van Breugel, B. Šavija, Experimental investigation of creep recovery of cement paste at the microscale, *Cem. Concr. Res.* (n.d.).
- [33] Y. Gan, C.R. Rodriguez, E. Schlangen, K. van Breugel, B. Šavija, Assessing strain rate sensitivity of cement paste at the micro-scale through micro-cantilever testing, *Cem. Concr. Compos.* 121 (2021).
- [34] G.A. Rao, B.K.R. Prasad, Influence of the roughness of aggregate surface on the interface bond strength, *Cem. Concr. Res.* 32 (2002) 253–257.
- [35] J.J. Ortega, G. Ruiz, R.C. Yu, N. Afanador-García, M. Tarifa, E. Poveda, X. Zhang, F. Evangelista, Number of tests and corresponding error in concrete fatigue, *Int. J. Fatigue*. 116 (2018) 210–219.
- [36] P. Vargas, O. Restrepo-Baena, J.I. Tobón, Microstructural analysis of interfacial transition zone (ITZ) and its impact on the compressive strength of lightweight concretes, *Constr. Build. Mater.* 137 (2017) 381–389.
- [37] G. Prokopski, J. Halbiniak, Interfacial transition zone in cementitious materials, *Cem. Concr. Res.* 30 (2000) 1–5.
- [38] K. Liao, P. Chang, Y. Peng, C. Yang, A study on characteristics of interfacial transition

- zone in concrete, *Cem. Concr. Res.* 34 (2004) 977–989.
- [39] X. Ouyang, D.A. Koleva, G. Ye, K. van Breugel, Understanding the adhesion mechanisms between C-S-H and fillers, *Cem. Concr. Res.* 100 (2017) 275–283.
- [40] R.J.M. Pellenq, H. Van Damme, Why does concrete set?: The nature of cohesion forces in hardened cement-based materials, *MRS Bull.* 29 (2004) 319–323.
- [41] A. Gmira, M. Zabab, R.J.M. Pellenq, H. Van Damme, Microscopic physical basis of the poromechanical behavior of cement-based materials, *Mater. Struct. Constr.* 37 (2004) 3–14.
- [42] C. Plassard, E. Lesniewska, I. Pochard, A. Nonat, Nanoscale experimental investigation of particle interactions at the origin of the cohesion of cement, *Langmuir.* 21 (2005) 7263–7270.
- [43] L. Armelao, A. Bassan, R. Bertoncello, G. Biscontin, S. Daolio, A. Glisenti, Silica glass interaction with calcium hydroxide: A surface chemistry approach, *J. Cult. Herit.* 1 (2000) 375–384.
- [44] W. HANSEN, Drying Shrinkage Mechanisms in Portland Cement Paste, *J. Am. Ceram. Soc.* 70 (1987) 323–328.
- [45] Z.P. Bazant, M.H. Hubler, Theory of cyclic creep of concrete based on Paris law for fatigue growth of subcritical microcracks, *J. Mech. Phys. Solids.* 63 (2014) 187–200.
- [46] A.M. Neville, G.A. Hirst, Mechanism of cyclic creep of concrete, *Spec. Publ.* 55 (1978) 83–102.
- [47] W. Ruetz, A hypothesis for the creep of hardened cement paste and the influence of simultaneous shrinkage, *Proc. Struct. Concr. Its Behav. under Load.* (1968) 365–387.
- [48] B. Isojeh, M. El-Zeghayar, F.J. Vecchio, Concrete Damage under Fatigue Loading in Uniaxial Compression, *ACI Mater. J.* 114 (2017).
- [49] M.E. Awad, Strength and deformation characteristics of plain concrete subjected to high repeated and sustained loads, University of Illinois Engineering Experiment Station. College of Engineering, University of Illinois at Urbana-Champaign, 1971.
- [50] M. Corrado, J.F. Molinari, Effects of residual stresses on the tensile fatigue behavior of concrete, *Cem. Concr. Res.* 89 (2016) 206–219.
- [51] Z.P. Bazant, Size Effect in Blunt Fracture: Concrete, Rock, Metal, *J. Eng. Mech.* 110 (1984) 518–535.
- [52] T.T.C. Hsu, F.O. Slate, Tensile Bond Strength Between Aggregate and Cement Paste or Mortar, *ACI J. Proc.* 60 (1963) 465–486.
- [53] X. Gu, L. Hong, Z. Wang, F. Lin, Experimental study and application of mechanical properties for the interface between cobblestone aggregate and mortar in concrete, *Constr. Build. Mater.* 46 (2013) 156–166.
- [54] J. Bisschop, P. Lura, J.G.M. Van Mier, Shrinkage microcracking in cement-based materials with low water-cement ratio, *Concr. Sci. Eng.* 3 (2001) 151–156.
- [55] H. Zhang, B. Šavija, Y. Xu, E. Schlangen, Size effect on splitting strength of hardened cement paste: Experimental and numerical study, *Cem. Concr. Compos.* 94 (2018) 264–276.
- [56] H. Zhang, Y. Xu, Y. Gan, E. Schlangen, B. Šavija, Experimentally validated meso-scale fracture modelling of mortar using output from micromechanical models, *Cem. Concr. Compos.* 110 (2020).



# 5

## LATTICE MODELLING OF FATIGUE RESPONSE OF CEMENT PASTE AT MICROSCALE

*In this chapter a numerical model using a 2D lattice network is developed for investigating the fatigue behaviour of cement paste at the microscale. Images of 2D microstructures of cement pastes obtained from XCT tests are used as input and mapped to the lattice model. Different local mechanical and fatigue properties are assigned to different phases of the cement paste. A constitutive law considering the fatigue damage evolution under cyclic loading is proposed. Flexural fatigue experiments performed at the same length scale are used to calibrate and validate the model. The proposed model can reproduce well the flexural fatigue experimental results, in terms of S-N curve, stiffness degradation and residual deformation. The validated model is then used to predict the uniaxial tensile fatigue fracture of cement paste. The effects of microstructure and stress level on the fatigue fracture are studied using the proposed model. This model forms a basis for the multiscale analysis of concrete fatigue.*

## 5.1 INTRODUCTION

As we have seen in previous chapters, concrete is a complex system with the multiscale heterogeneity ranging from nanometres to centimeters [1–3]. The phenomenon of concrete fatigue inherently involves multiple spatial scales. Nowadays, there is an increasing interest for multiscale modelling [4], which could connect the heterogeneous material structure and properties at finer scales with the macroscopic behaviour of concrete. Several attempts have been made to investigate the effect of mesostructure of concrete on the global fatigue behaviour [5–7]. The content and shape of aggregate and the local fatigue properties of the paste matrix and the interfacial transition zone (ITZ) can be properly considered in these mesostructure-informed models. However, no model has been developed to date for fatigue of cement paste at the microscale. At this scale, the cement paste is mainly composed of calcium hydroxide (CH), unhydrated cement (UHC), calcium-silicate-hydrate (C-S-H) and pores of various sizes. For a complete and sophisticated multiscale modelling scheme, the model has to be established and validated at different subsequent scales. Therefore, the present study aims to develop and validate a microstructure-informed model for investigating the fatigue behaviour of cement paste at the microscale.

Since the presence of heterogeneities at different levels of observation complicates fatigue fracture, the first challenge is to choose an appropriate model to consider the heterogeneity. From the perspective of statistical physics, lattice type models have shown to be quite useful in dealing with the disorder in quasi-brittle materials [8]. Lattice models have been successfully used for simulating the fracture and deformation behaviour of cementitious materials [9–15]. In these models, the material is discretized into a network (i.e. lattice) of elements. Different properties of interest, e.g. mechanical and transport properties, could be assigned to these elements [14,16,17]. The material heterogeneity at various levels of observations can be directly implemented into the model by adjusting the local properties of lattice elements [18,19]. When the fracture of cement-based material under monotonic loading is examined, the cracks simulated by lattice fracture are very realistic and resemble the experimentally observed cracks [4,20,21]. In the current study, the lattice fracture model is extended to simulate the fatigue fracture process of cement paste at the microscale.

In this chapter the fatigue lattice model is first established by considering the microstructure of cement paste and local fatigue damage evolution. Microscale flexural fatigue test results from the Chapter 3 are used to directly calibrate and validate the model. Then uniaxial tensile fatigue simulations are performed to investigate the effects of microstructure and stress level on the global fatigue fracture behaviour. The fatigue simulations are also compared with static simulations to better understand the fatigue fracture process.



## 5.2 NUMERICAL APPROACH

### 5.2.1 EXPERIMENTALLY-OBTAINED 2D VIRTUAL SPECIMENS

In general, the heterogeneous microstructure of cement paste can be obtained by either experimental methods, e.g. scanning electron microscopy (SEM) [7] and X-ray computed micro-tomography (XCT) [13,18], or computer-generated approaches, e.g. HYMOSTRUC [22],  $\mu\text{c}$  [23] and CEMHYD3D [24]. In this study, miniature cement paste specimens fabricated in Chapter 3 are scanned by XCT to obtain the realistic microstructure. Three beams for each w/c ratio are then scanned using XCT to obtain greyscale-based 2D images, see Figure 5-1(a). The segmentation procedure using the global thresholding method [15,25] is performed on these CT images. Three threshold values are defined to segment different components in the cement paste based on the grey-scale histogram. These threshold values are determined by using either the inflection point of the cumulative grey-scale value curve or the change of the tangent slope [15,25].

The hydration degree and w/c ratio are also used as inputs to segment the main hydration products [26]. As is shown in Figure 5-1(b), four main phases, i.e. unhydrated cement (UHC), high-density (HD) C-S-H, low-density (LD) C-S-H and pores, can be distinguished after the segmentation. It should be mentioned that other hydration products, e.g. calcium hydroxide (CH), ettringite (AFt) and monosulfate (AFm), are not segmented in this study, but embedded in other segmented phases. More details on the segmentation procedure can be found in [15,17,25]. Before the construction of the lattice network, the spatial resolution of XCT images is reduced to  $5\ \mu\text{m}/\text{pixel}$  using the bilinear interpolation algorithm to save computational time. Note that, if a different resolution would be used in the model, the calibration process should be repeated.

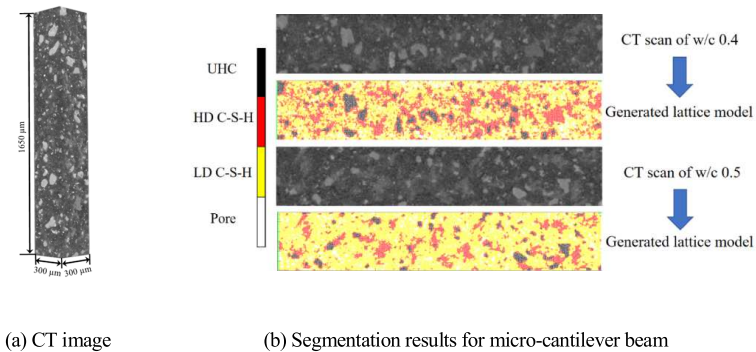
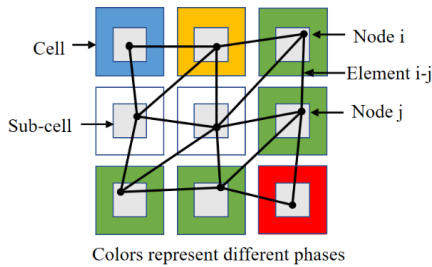


Figure 5-1 (a) the CT image of a micro-cantilever beam; (b) segmentation results for different w/c ratios

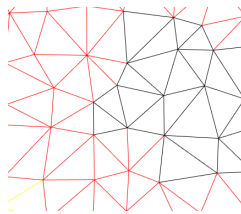
## 5.2.2 GENERAL DESCRIPTION OF LATTICE MODEL

### DOMAIN DISCRETIZATION

The first step of lattice model construction is to discretize the material structure by a lattice network. A group of cells is generated based on the pixel images obtained from XCT tests, and each cell coincides with a single pixel. In each pixel, a sub-cell is created and the length ratio of the sub-cell to the cell, which is defined as the randomness, is set to be 0.5 here [27]. Subsequently, a node is randomly created inside each sub-cell by using a pseudo-random number generator. Delaunay triangulation of the domain is then performed on these nodes as is described in [16,28,29]. The neighboring nodes are connected to form the lattice network, see Figure 5-2. The reason for using irregular lattice networks is to introduce local heterogeneity and disorder and avoid mesh dependence of crack paths [9]. By assigning these beams with different properties, the microstructure of the material can be mapped on the lattice network. Figure 5-2(b) shows the generated lattice models for two w/c ratios based on the segmented 2D virtual specimens, which are 2D slices randomly selected from the 3D CT-scanned specimen.



(a) Schematic diagram of lattice network generation



(b) Generated lattice network

Figure 5-2 Lattice element generation procedure

## MECHANICAL CONSTITUTIVE LAW

In the lattice model, the cement paste is discretized as a set of Timoshenko beam elements. All beam elements are assumed to exhibit linear elastic brittle behaviour with different elastic modulus and maximum strength, depending on the XCT images. Under pre-defined boundary conditions, a linear elastic analysis is performed and the node displacement of each element is calculated. Details about the numerical algorithms can be found in [15,29,30]. To simulate the fracture process, removing (or partially removing) of lattice beams is done step-by-step upon reaching a certain criterion [9,12]. For the determination of fracture criterion in the case of monotonic loading, the comparative stress  $\sigma_c$  is calculated as the combination of normal force and bending moment [9], as follows:

$$\sigma_c = \alpha_N \frac{N}{A} + \alpha_M \frac{M}{W} \quad (5-1)$$

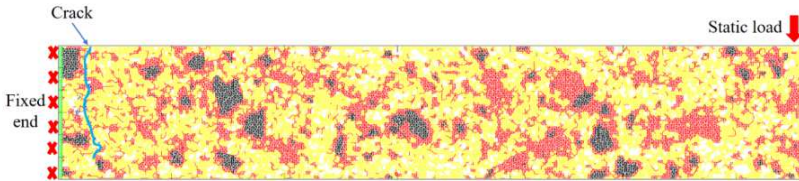
where  $A$  denotes the cross-section area of the beam element;  $W$  is the cross-sectional moment of resistance;  $N$  and  $M$  are the local normal force and bending moment, respectively.  $\alpha_N$  and  $\alpha_M$  represent the normal force influence factor and the bending influence factor, which are generally chosen as 1.0 and 0.05, respectively [27,29,31]. The effect of these factors on the overall fracture behaviour is discussed elsewhere [32]. The stress level in each element is calculated by dividing the comparative stress with the defined local tensile strength  $f_t$  of the element. The critical element, which has the highest stress level, is then partly removed from the system following the softening cyclic constitutive law described in Section 5.2.3 to represent the cracking. The local elastic moduli  $E_n$  and tensile strengths  $f_t$  of different phases, obtained in the author's previous work [15], are summarized in Table 5-1. The strain at the peak stress  $\varepsilon_0$  for each phase is also given. Note that, for interface elements between two different phases, lower values of mechanical properties among these two phases are assigned [15].

Table 5-1. Local properties for different phases of hydrated cement paste [15]

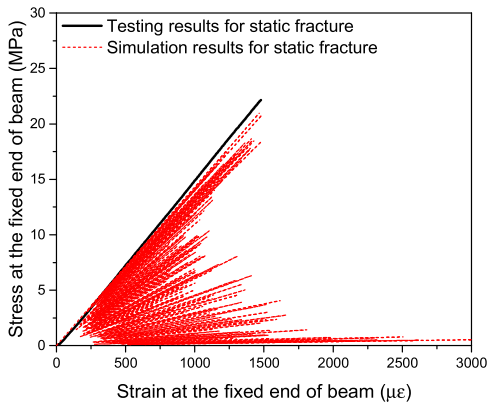
Phases	$f_t$ (MPa)	$E_n$ (GPa)	$\varepsilon_0$ ( $\mu\epsilon$ )
UHC	614.7	84.2	7300
LD C-S-H	52.2	21.3	2451
HD C-S-H	82.8	26.4	3136

The experimental results of bending tests on cement paste beams in Chapter 3 are used here to calibrate and validate the model. In the simulations, the same boundary condition with the experiments is applied on virtual samples, as is illustrated in Figure 5-3(a): the static load is imposed on one side of the virtual sample and the other end of

the sample is fixed. A typical simulated stress-strain curve as well as the fracture pattern for a flexural static test is shown in Figure 5-3. Generally, the major crack will initiate at the weakest locations near the fixed end and propagate into the beam, leading to complete fracture. The red zig-zag lines observed in the post-peak response can be explained by the fact that after a beam element is removed, much less load is required to break the next beam in the system, after which again a higher load is needed to continue further. Such local snap-backs, which are difficult to be measured experimentally, can be simulated since the solution algorithm of lattice model allows the system to relax and be reloaded afterwards. This behaviour demonstrates the local instabilities during the crack formation and propagation in quasi-brittle materials. The local mechanical properties will serve as the initial properties in the following fatigue simulations.



(a) w/c 0.4 sample



(b) Stress-strain curve

Figure 5-3 Simulation results of one w/c 0.4 sample ( $1650 \mu\text{m} \times 300 \mu\text{m}$ ): (a) the fracture pattern under static loading; (b) the comparison of the stress-strain curve with experimental results

### 5.2.3 FATIGUE LATTICE MODEL

#### CONSTITUTIVE LAW FOR CYCLIC LOADING

If the model is subjected to the cyclic stress with the magnitude lower than the macroscopic strength, the lattice system will never fail. Therefore, a constitutive law incorporating the fatigue damage evolution is used here to consider the degradation of mechanical properties under fatigue loading. In reality, the fatigue damage of cementitious material mainly consists of the progressive growth of internal microcracks [33,34]. The growth of a microcrack manifests itself through degradation of macroscopic properties, such as stiffness. To account for this behaviour, the cyclic constitutive law for a lattice beam element is proposed, as is shown in Figure 5-4. The cyclic stress-strain curve for describing the mesoscopic fatigue behaviour is originally developed by Nagai et al. [35], and further modified by Gong et al. [5]. This cyclic law is similar to the continuous-function model developed by Hordijk [36] for simulating the post-peak cyclic behaviour of the crack in concrete.

At each analysis step of the fatigue fracture simulation, the maximum fatigue load is imposed on the system. The comparative stress and corresponding stress level in each lattice element are calculated. Based on the stress levels and the number of cycles, the calculated fatigue damage in the form of mechanical degradation is assigned to all damaged beams. For the unloading stage it is assumed that the unloading process will not generate any damage such that the reloading curve (blue arrow) will overlap with the previous unloading curve (red arrow). Moreover, based on experimental observations [5,37,38], there are always residual strains under cyclic loading. Therefore, the unloading curve in each loading cycle will not pass through the origin (see Figure 5-4). More details regarding the determination of residual strain will be discussed later. After unloading, the system will be updated due to the new stiffness matrix and the remaining strength of each element. If the global stiffness of the system falls below 20% of its original stiffness, the simulation is stopped and the system is considered to have failed. Otherwise, another analysis step is executed. Note that an analysis step does not always represent one loading cycle, as explained in the next paragraph.

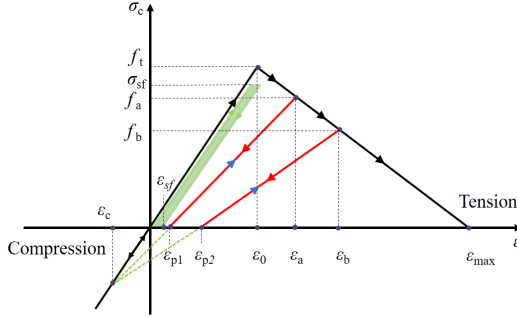


Figure 5-4 The constitutive law of individual lattice elements subjected to cyclic loading

As is shown in Figure 5-4, the beam is assumed to be purely linear elastic in compression and neither compressive failure nor compressive fatigue damage will occur. Only the mechanical properties of beams subjected to comparative tensile stress, see Eq.(5-1), will gradually decrease depending on the stress level and number of cycles. When in tension, the pre-peak regime is characterized by the initial strength  $f_t$  and elastic modulus ( $f_t/\varepsilon_0$ ) of the beam element, which are identical to the static mechanical properties (Table 5-1).

There are two scenarios for the implementation of fatigue damage at the microscale. Firstly, if the calculated highest comparative stress is lower than its remaining strength (i.e.  $\sigma_{sf} < f_t$ ), the mechanical properties of all the beams will be reduced based on the current stress level (green lines in Figure 5-4. Each phase in cement paste is assigned with a fatigue property following the phenomenological  $S-N$  approach [39,40], which reads as:

$$S_i = -a \cdot \log(N_i) + b \quad (5-2)$$

where  $S_i$  is the stress level of the element at the  $i$ -th analysis step;  $N_i$  is the corresponding fatigue life;  $a$  and  $b$  are two parameters deciding the fatigue properties of hydration product phases. In this study, the parameters  $a$  and  $b$  for different phases, namely LD C-S-H and HD C-S-H, will be determined by fitting the simulation results to experimental results. Based on Eq. (5-2) the fatigue life can be calculated if the stress level is known, and vice versa.

Another important parameter is the fatigue damage index  $D$ , defined as the reduction percentage of strength with respect to the initial strength of the element. The remaining strength of the damaged element is calculated as  $(1-D)f_t$ . When  $D=0$ , the element is assumed to be undamaged, and when  $D=1$  the element will be removed from the mesh. Note that the same fatigue damage index is used for the elastic modulus of a damaged element in the current scenario. Generally, the fatigue damage  $D$  for each

element should be accumulated with increasing number of cycles, and a higher stress level results in a higher degree of fatigue damage. Since the stiffness matrix is always updated due to the fatigue damage, the stress in the element will be redistributed in each loading cycle. Therefore, in order to consider the effect of redistribution of stress during the cyclic loading, the fatigue damage  $D_i$  at the  $i$ -th step is calculated based on the Miner's rule [41] and the fatigue damage in the previous step  $D_{i-1}$ :

$$D_i = \frac{n_c}{N_i} + D_{i-1} \quad (5-4)$$

where  $n_c$  is defined as the cycle block for each analysis step and  $N_i$  is the fatigue life calculated from Eq.(5-2) based on the  $i$ -th step of stress level. It should be mentioned that, even though the Miner's law may not precisely reflect the actual fatigue damage evolution of cementitious materials and may lead to non-conservative results, this law is widely used for its simplicity [36,42–44]. An alternative would be to consider the fatigue damage evolution using thermodynamic concepts under the damage mechanics framework, as proposed in [45,46].

In general, a high-cycle fatigue test of cement paste under a moderate stress level involves tens of thousands of cycles. It is inefficient to explicitly simulate every loading cycle. Therefore, a proper strategy is preferred for fatigue damage simulation. To this end, the "block cycle jump" technique, in which a certain number of cycles are packaged as one block loading case, is usually adopted [47]. Similarly, an appropriate number of cycles is chosen as the cycle block defined in Eq.(5-4) to speed up the fatigue simulation in this study. The effect of cycle block size on the simulated fatigue life and computational time is shown in Figure 5-5. It can be seen that the increasing of cycle block size from 10 to 1000 leads to a slightly higher fatigue life. However, the computational time is reduced significantly. In this study, a pre-defined number of 1000 cycles is used for the cycle block. This means that the fatigue damage for 1000 cycles can be considered in one analysis step. It should also be noted that, if the cycle block value is very close to or even higher than the final fatigue life, the simulation may generate unrealistic results. Therefore, the value of a cycle block will be adjusted for each simulation until it is at least ten times lower than the final fatigue life.

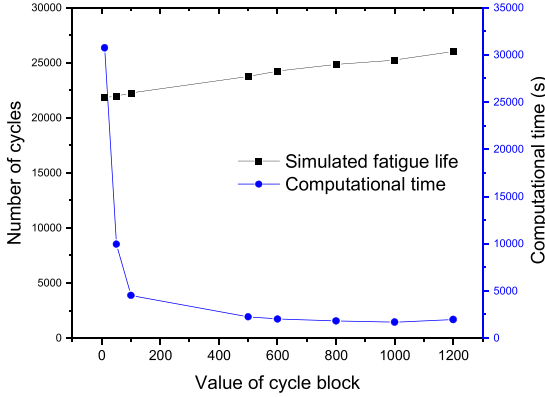


Figure 5-5 The effect of cycle block value on the simulated fatigue life and computational time

The second case for considering the fatigue damage is that when the calculated highest stress level for the critical element exceeds 1 (i.e.  $\sigma_{st}/f_t > 1$ ), a post-peak cyclic softening behaviour is assumed for this element, see Figure 5-4. In this case the remaining strength of the element is gradually reduced following a linear softening curve [35,36,48]. For simplicity, it is assumed that only four softening steps are required for an element to reach the final fracture. At each softening step a certain percentage of reduction  $d_{\text{soft}}$  in strength is assumed for this element, e.g.  $f_a = (1 - d_{\text{soft}})f_t$  and  $f_b = (1 - d_{\text{soft}})^2 f_t$ . Therefore, the fatigue damage index of this element at the  $i$ -th step should be  $D_i = 1 - (1 - d_{\text{soft}})(1 - D_{i-1})$ . Following the approach described in [5], a constant strain ( $\varepsilon_c = -400 \mu\epsilon$ ) at the compression branch is introduced for all phases to determine the percentage of reduction for elastic moduli and the residual strains (e.g.  $\varepsilon_{p1}$  and  $\varepsilon_{p2}$ ). When the maximum strain  $\varepsilon_{\text{max}}$  is also known, the residual strain  $\varepsilon_{p1}$  and the corresponding damaged elastic modulus  $E_{d1}$  of the element can be calculated with the following equations:

$$\varepsilon_{p1} = \frac{d_{\text{soft}}\varepsilon_c(\varepsilon_0 - \varepsilon_{\text{max}})}{\varepsilon_0 - \varepsilon_c} \quad (5-4)$$

$$E_{d1} = \frac{(1 - D_i)f_t}{\varepsilon_a - \varepsilon_{p1}} \quad (5-5)$$

Note that the unhydrated cement (UHC) phase is assumed to have infinite fatigue life without any fatigue damage accumulation. Only the two C-S-H phases in the cement paste are assumed to experience fatigue damage. The calibration of parameters for



characterizing the fatigue damage evolution and residual deformation will be performed in the next section.

## RESIDUAL DEFORMATION

Another important characteristic of fatigue test is the residual deformation. It has been suggested that the residual deformation is mainly attributed to the creep deformation and fatigue crack growth [39,49]. For each analysis step in the fatigue simulation, the local residual deformation of each element will be determined and then imposed on the lattice elements to calculate the macroscopic residual deformation through the approach described in [15]. In this study, the change of strain at the maximum fatigue load is defined as the residual strain and the fatigue compliance is defined by dividing the residual strain by half of the applied maximum stress.

For the case of  $\sigma_{st}/f_t > 1$ , the residual deformation of the critical element is determined based on the post-peak cyclic behaviour as is depicted in Figure 5-4. If the stresses in all elements are lower than their strengths, the residual deformation of each element will be calculated considering the creep and fatigue crack growth. In this case the cycle block is also used to accelerate the fatigue analysis in one analysis step. Bazant and Hubler [49] developed a theoretical model to relate the macroscopic deformation of concrete with the microscopic fatigue crack growth based on the Paris's law. According to Bazant et al. [49], the total material compliance  $J_{tot}$  under cyclic loading is:

$$J_{tot} = J(t, t_0) + \Delta J_f \quad (5-6)$$

$$J(t, t_0) = \alpha_c \left( \frac{t - t_0}{t_1} \right)^{\beta_c} \quad (5-7)$$

$$\Delta J_f = C_t \cdot t \cdot f_{Hz} \left( \frac{\Delta \sigma}{f_t} \right)^\gamma \quad (5-8)$$

where  $J(t, t_0)$  is the basic creep compliance given in [50,51]. It is defined as the creep strain at time  $t$  caused by a unit stress applied at the beginning time  $t_0$ .  $t_1$  is the time unit.  $\alpha_c$  and  $\beta_c$  are two creep parameters for each phase and  $\Delta J_f$  is the fatigue compliance due to crack growth under cyclic loading [49]. The exponent  $\gamma$  is a constant with the value of 4 [5,49] and  $C_t$  is a fitting parameter [5].  $\Delta \sigma$  is the fatigue stress amplitude of the element and  $f_{Hz}$  is the loading frequency. The time needed for one complete cycle equals the inverse of loading frequency, i.e.  $1/f_{Hz}$ . Therefore, the number of cycles  $N$  can be calculated as  $t \cdot f_{Hz}$ . Note that the current model is only applicable for the fatigue loading with a low loading frequency. When a higher loading frequency is used, the inertia effect of fatigue loading begins to play a role and should be taken into account [52,53].

### 5.3 MODEL CALIBRATION AND VALIDATION

The flexural fatigue tests on the MCBs are performed in Chapter 3. The experimental results in terms of  $S-N$  curves, stiffness degradations and residual deformation evolutions of MCBs have been used to calibrate the 2D flexural fatigue lattice model. As there is almost no other available experimental data for the fatigue of cement paste at the microscale in literature, the validation is carried out by simulating samples that have not been used in the calibration phase. These samples differ in microstructures and w/c ratios. In the validation phase, parameter adjustment is not permitted. The calibration is first conducted on the sample with the w/c of 0.4. The calibrated parameters for two C-S-H phases are summarized in Table 5-2.

For the calibration of parameters determining the fatigue compliance evolution at the free end of the beam, the same loading protocols as the experiments described in Chapter 3, in terms of loading frequency (0.55Hz), number of cycles (500) and stress level (80%), are used in the simulation. The value cycle block is chosen as 1 for this case. It means that each of the 500 cycles is explicitly simulated. The creep parameters for two C-S-H phases are calibrated using the recently obtained basic creep compliance results [54]. From a trial-and-error method, the parameters responsible for the fatigue crack growth are obtained (Table 5-2). Since it is currently impossible to measure the strain capacity of each phase at this scale, both C-S-H phases are assumed to have the same maximum strain  $\varepsilon_{\max}$  (3200  $\mu\varepsilon$ ), which is slightly larger than the strain at the peak stress  $\varepsilon_0$  (3136  $\mu\varepsilon$ ). In Figure 5-6, the fatigue compliance curves of different virtual samples are compared with the experimentally measured fatigue compliance (average values with standard deviations). The figure shows that most of the simulated fatigue compliance curves using calibrated parameters lie in the range of the experimental results. Large scatter still exists in the magnitudes of simulated fatigue compliance for different virtual samples. This large scatter is mainly due to the 2D heterogeneous microstructures.

Table 5-2 Calibrated parameters for the fatigue simulation

Phases	$a$	$b$	$\alpha_c$ ( $10^{-6}/\text{MPa}$ )	$\beta_c$	$C_t$ ( $10^{-6}/\text{MPa}$ )	$\varepsilon_{\max}$ ( $\mu\varepsilon$ )	$d_{\text{soft}}$ (%)
HD C-S-H	0.02	1.1	0.23	0.20	$5 \times 10^{-6}$	3200	20
LD C-S-H	0.04	1.1	0.34	0.20	$1.2 \times 10^{-5}$	3200	20

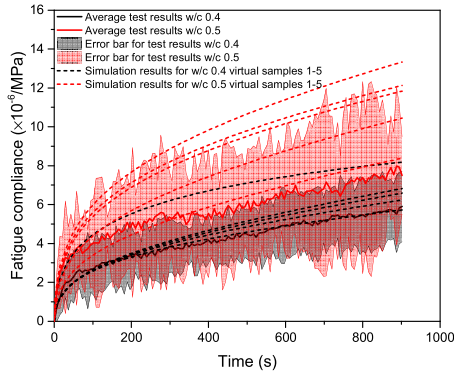


Figure 5-6 The comparison of experimentally measured fatigue compliances and simulation results (w/c 0.4 and 0.5, 28 days)

Meanwhile, the parameters for describing the fatigue damage evolution have been calibrated using experimentally obtained  $S$ - $N$  relationships. Firstly, the effect of the fatigue parameter  $b$  on the simulated  $S$ - $N$  curve is investigated and shown in Figure 5-7. In general, the global fatigue life increases with increasing value of  $b$ . To simplify the calibration process,  $b$  is chosen as 1.1 for both C-S-H phases.

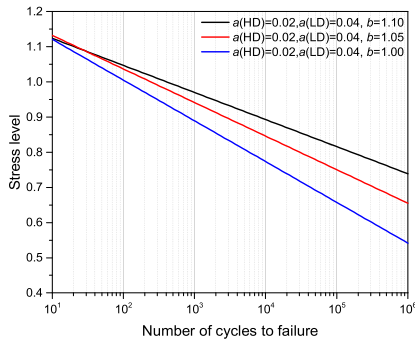


Figure 5-7 The effect of  $b$  on the simulated  $S$ - $N$  curves

Before determination of the fatigue parameter  $a$ , several pairs of values for the two phases, i.e. LD C-S-H and HD C-S-H, have been used for trial simulations. The simulated  $S$ - $N$  curves for one virtual specimen ( $w/c$  0.4), using different fatigue parameters, are compared with experimental results [37] and shown in Figure 5-8. At a given stress level, the global fatigue life decreases with increasing magnitude of fatigue parameters (or decreasing of local fatigue properties). For the virtual sample used in the simulation, the two parameters with values  $a(\text{HD})=0.02$  and  $a(\text{LD})=0.04$  seem to fit well with the experimental results in terms of the slope of the  $S$ - $N$  curve. Therefore, these two values are adopted in the simulations for other  $w/c$  0.4 virtual samples and  $w/c$  0.5 virtual samples with different microstructures. For each virtual sample, three different stress levels are applied. The simulated  $S$ - $N$  curves are compared with experimental results and shown in Figure 5-9. A wide variation of simulated fatigue life for different virtual samples can be observed. However, it should be pointed out that each virtual sample follows a unique linear  $S$ - $N$  curve on the semi-log scale. This indicates that the major source of scatter in the fatigue simulation originates from the heterogeneous material microstructure. Another source of uncertainty for fatigue results comes from the determination of the true static strength, which is used to determine the nominal stress level. This problem can also be tackled by performing the static simulation. Despite the large variation between individual samples, it has been clearly demonstrated that there is a significant difference in fatigue life for two  $w/c$  ratios, see Figure 5-9.

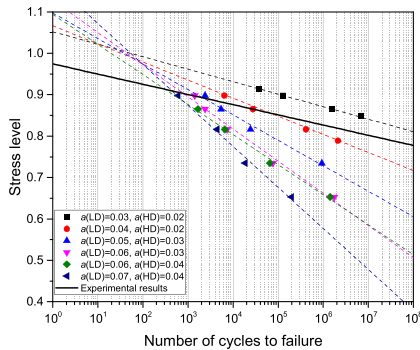


Figure 5-8 Simulated  $S$ - $N$  curves for one virtual sample ( $w/c$  0.4, 28 days) using different fatigue parameters

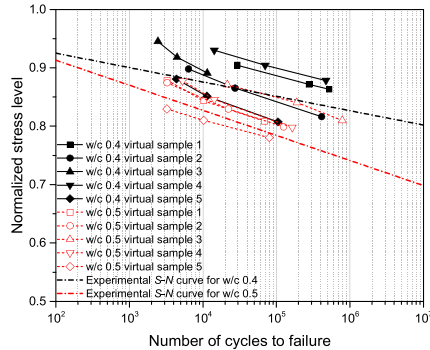


Figure 5-9 The simulated  $S-N$  curves for different virtual samples

Two examples of simulated fatigue fracture patterns are shown in Figure 5-10. Interestingly, multiple cracks have been observed for some fatigue flexural simulations (see the  $w/c$  0.4 virtual sample in Figure 5-10). Similar findings have been found in experimental results reported in literature [55–58]. Besides, the  $w/c$  0.4 sample is more heterogeneous than the  $w/c$  0.5 specimen. Therefore, the possibility for multiple cracking can also be higher. In general, the crack initiates at the weakest locations, e.g. LD C-S-H phases, under both static and fatigue loadings. It is clear that the mechanical properties of each phase are important for the fatigue fracture behaviour. The major difference is that, when one propagating crack is impeded by other phases with higher fatigue resistances, i.e. HD C-S-H or UHC, this crack may branch or continue to propagate depending on the stress level, number of cycles as well as the accumulated fatigue damage in the surrounding phases. Since all C-S-H phases are simultaneously experiencing some degree of fatigue damage in previous loading cycles and the fatigue damage evolution for HD C-S-H is much slower than that of LD C-S-H, some cracks may also initiate in LD C-S-H at other locations. Due to the updated global stiffness according to the fatigue damage accumulation, the stress redistribution will occur under each flexural cyclic loading and may lead to the presence of multiple cracks. However, it should be mentioned that this situation may only apply at the low stress level, as the difference in fatigue life for two C-S-H phases is significant. When the stress in an element is slightly lower than its strength, the fatigue life for two phases is very close and only differs by some cycles. This may indicate different fatigue fracture behaviour at different stress levels. If the stress level is high, the fatigue fracture tends to be identical with the static fracture behaviour. For instance, the fatigue fracture pattern of the  $w/c$  0.5 virtual sample in Figure 5-10 is similar to its static fracture. One can also envision that, by manipulating the difference between fatigue properties of two C-S-H phases, the fatigue fracture pattern will change. Therefore, the quantification of the fatigue properties of two C-S-H phases is crucial for the fatigue fracture simulation of

cement paste. In addition, the fatigue cracks in the simulations are dependent on the degree of heterogeneity and the distributions of different phases. This aspect will be further illustrated using the uniaxial tensile fatigue simulations in Section 5.4.

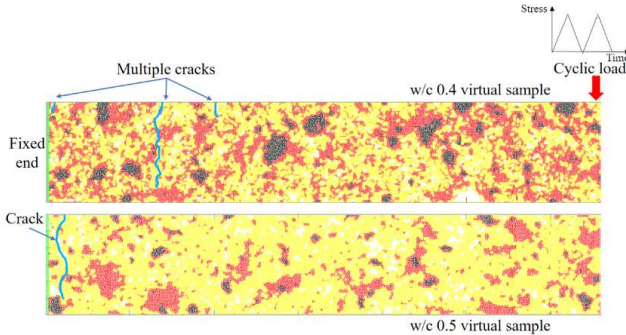


Figure 5-10 Examples of the fatigue fracture patterns for w/c 0.4 and 0.5 virtual samples

Typical stress-strain curves under the cyclic loading are presented in Figure 5-11. With the increasing number of cycles, the slope of the loading cycle gradually decreases. To monitor the stress evolutions of beam elements under flexural cyclic loading, the comparative stresses of beams at two locations have been extracted from the simulations, see Figure 5-12(a). It can be seen that at the location 1, which is at the fixed end of beam, both stresses in LD C-S-H and HD C-S-H beams increase slowly before the unstable cracking is reached. The UHC seems to remain constant during most of the fatigue life. On the contrary, the stresses of LD C-S-H and HD C-S-H beams at the location 2, which is at the vicinity of the major fatigue crack instead of the cracking tip, appear to gradually decrease with the increasing number of cycles. Similarly, the stresses in UHC elements remain almost constant before the unstable cracking. Note that the highest stress is always at the tip of the major crack due to the stress concentration. This would result in a higher degree of fatigue damage accumulated in these elements near the cracking tip. The beam elements at the location 2 are supposed to experience significant change of stress during the stress redistribution process, while the beam stresses at the location 1 would show a gradual increase before the unstable cracking due to a relatively slower fatigue damage accumulation. It is also found that in both locations the stresses in UHC elements change much slower than those in HD C-S-H and LD C-S-H beams, while the stresses in HD C-S-H also change slightly slower than those in LD C-S-H elements. This could be explained by less fatigue damage generated in these elements.

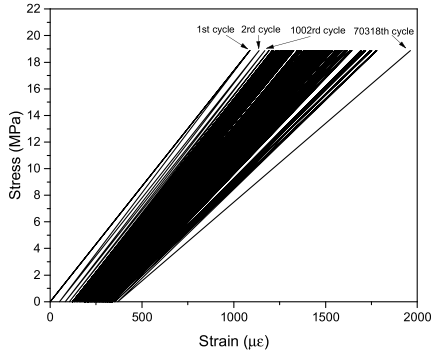
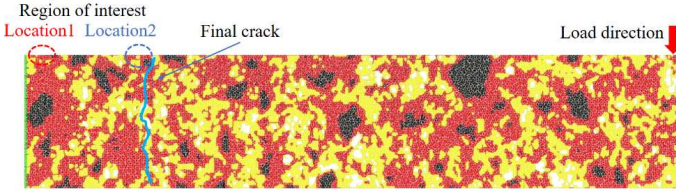
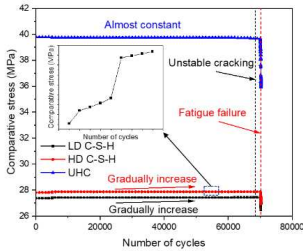


Figure 5-11 A typical simulated stress-strain curve for one w/c 0.4 sample under cyclic loading with the upper stress level of 90%

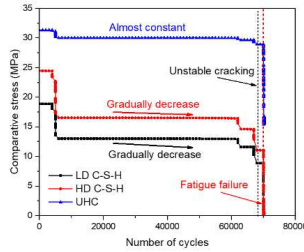
The changes of the global elastic moduli for virtual samples, which represent the stiffness degradations under fatigue loading, are shown in Figure 5-13, along with the results of measurements. It can be seen that in most of the fatigue life the reduction of elastic modulus is very small. Overall, both the numerical and experimental results suggest a slow and limited flexural fatigue damage evolution process for cement paste at the microscale. Another important feature of fatigue fracture is that the fatigue crack becomes unstable when the total damage has accumulated to a certain degree. This is primarily because the remaining cross-section of the specimen can no longer sustain the external fatigue loading. It is manifested as a sudden drop of stiffness, as is shown in Figure 5-13 (marked as blue lines).



(a) Fracture pattern



(b) Location 1



(c) Location 2

Figure 5-12 The stress evolutions of different types of upper fiber beam elements in the region of interest under cyclic loading: (a) fracture pattern; (b) location 1 and (c) location 2

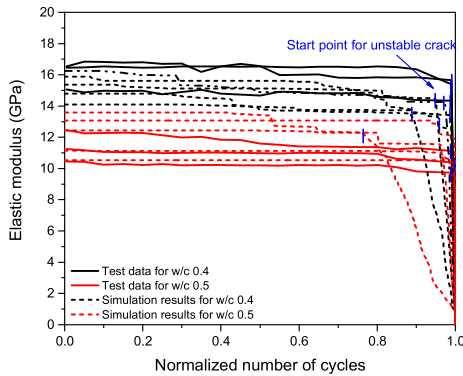


Figure 5-13 The simulated elastic modulus degradation along with the experimental results



## 5.4 2D UNIAXIAL TENSILE FATIGUE LIFE AND FRACTURE BEHAVIOUR

By using the calibrated lattice fatigue model, it is now possible to simulate the uniaxial tensile fatigue behaviour of cement paste at the microscale. The output of the uniaxial tensile fatigue simulations could also be used as input for multiscale analysis of concrete [13,19]. The calibrated parameters from the previous section are adopted here to predict the uniaxial tensile fatigue life and fracture pattern of cement pastes. Images of the microstructure of cement pastes (w/c 0.4) with the size of  $500 \times 500 \mu\text{m}^2$  are extracted from the segmented CT results, see Figure 5-14. In the uniaxial fatigue simulations, 8 virtual samples are generated, and each virtual sample is subjected to three different loading levels. Hence, in total 24 simulations are performed.

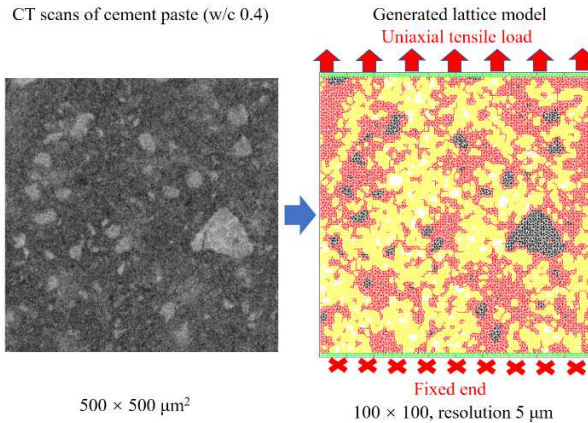


Figure 5-14 The generated lattice model from CT scans for uniaxial tensile fatigue simulation

The simulated uniaxial tensile fatigue results for all virtual samples are summarized in Table 5-3. The obtained  $S-N$  curves of virtual samples and also the assumed local  $S-N$  curves for both C-S-H phases are shown in Figure 5-15.

Table 5-3 The simulation results for 8 virtual samples under uniaxial tensile fatigue

Virtual sample No.	Static tensile strength (MPa)	Stress level (%)	Fatigue life
1	16.01	82.45	532462
		84.95	131474
		87.42	37470
2	16.10	86.97	237598
		89.46	66614
		91.94	22574
3	10.84	81.17	462306
		84.86	56306
		88.55	9302
4	20.48	85.96	28553
		87.92	11553
		89.87	5553
5	17.79	85.43	104534
		87.68	35502
		89.93	13518
6	18.45	84.55	238509
		86.72	74521
		88.88	27501
7	17.56	86.54	191526
		88.82	56518
		91.09	17526
8	19.18	85.53	40522
		87.61	15518
		91.78	3526

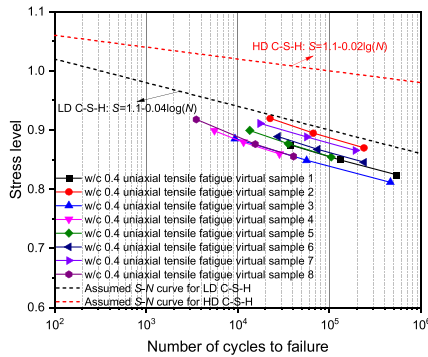


Figure 5-15 Simulated uniaxial tensile fatigue  $S-N$  curves for w/c 0.4 virtual samples

It is clear from both Table 5-3 and Figure 5-15 that the fatigue life decreases with increasing stress level. Similar to flexural fatigue, each virtual sample subjected to uniaxial tensile fatigue also exhibits a unique  $S-N$  relationship and the difference in  $S-N$  curves between each sample is caused by the heterogeneity of the microstructures. Moreover, at a given stress level the uniaxial tensile fatigue life of cement paste is always lower than that of pure C-S-H phases as is shown in Figure 5-15. This is attributed to the presence of pores and stiff particles (UHC), which introduce stress concentrations into the system.

To gain more insight into the fatigue fracture behaviour, the fatigue cracks at different loading cycles are illustrated in Figure 5-16. The loading cycles have been normalized to the final fatigue life. Note that the 3D features of fracture behaviour in heterogeneous materials cannot be reflected by the current 2D model. All analyses are performed based on 2D results. At the beginning of the fatigue simulations, the upper load of fatigue will sometimes generate a few cracks in the system, mostly distributed in LD C-S-H near the pores, see Figure 5-16. Before the fatigue failure, the fatigue crack will always propagate following the weakest link in the system, which is similar to the static fracture behaviour. Therefore, for most simulation results, the fatigue fracture patterns are similar to the static fracture patterns. For example, Figure 5-16 shows that both the major static crack and fatigue crack pass through the disconnected pores and result in the final failure. This could also be attributed to the high stress levels used in these simulations, i.e. around 81-92% of static strength. However, it should be borne in mind that the fatigue fracture also depends on the local stress fields and fatigue damage evolution rates of different phases.

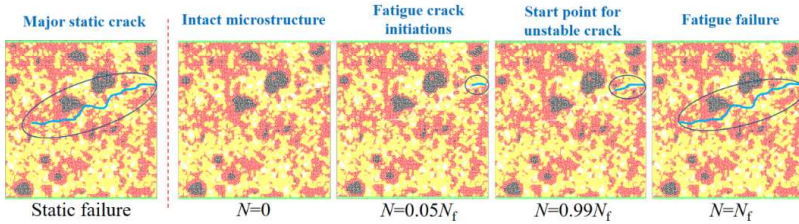
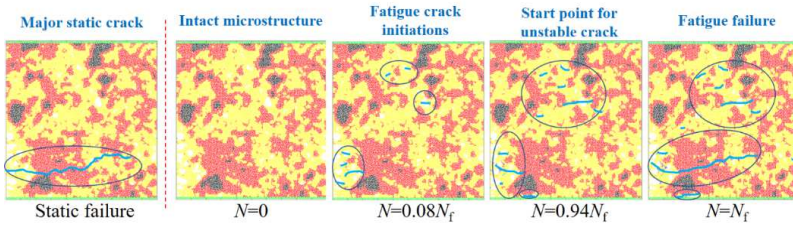


Figure 5-16 One example of fatigue crack development in cement paste (w/c 0.4) under uniaxial tensile fatigue loading at the stress level of 87.4% and the simulated fatigue life  $N_f$  is 37470

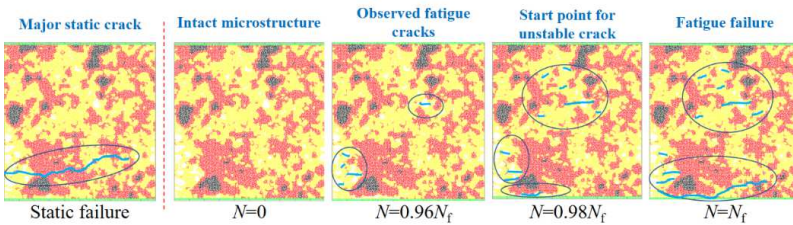
In order to demonstrate the different fatigue fracture behaviour at different stress levels using the developed fatigue lattice model, two stress levels, i.e. 85% and 50%, are applied on the same virtual sample. Due to the high fatigue resistance of cement paste at the microscale, the simulated fatigue life at the low stress level (50%) will be at least  $10^{14}$ - $10^{15}$  cycles. Therefore, for the purpose of demonstration, lower fatigue properties are assigned to the two C-S-H phases, i.e.  $a(\text{LD})=0.09$  and  $a(\text{HD})=0.04$ . It is worth mentioning that, for macroscopic fatigue simulation of concrete, the interface transition zone (ITZ) between the aggregate and cement paste is generally expected to have much lower fatigue resistance compared to the paste matrix. In this case, lower fatigue properties may be used [5,6,43,58–62]. The simulated fatigue fracture patterns are shown in Figure 5-17.

Figure 5-17(a) shows that several cracks initiate at the early stage of fatigue loading (marked in blue circles) when the stress level is 85%. At this stress level, the local stresses near the crack tip are also high, such that the rates of local fatigue damage evolution are at the same magnitude for both C-S-H phases, as have been explained before. As a result, the crack will propagate into both C-S-H phases alike. When the loading cycles reach the starting point for the unstable crack, this stage of cracking behaviour is similar to the static fracture. Therefore, the final fatigue crack resembles the static fracture in this high stress level. However, in Figure 5-17(b), where a lower stress level (50%) is applied, almost no crack is observed in the model until the number of loading cycles reaches 96% of fatigue life. Note that the crack initiation actually happens at the beginning of fatigue loading. However, these cracks occur at much smaller scales (e.g.  $< 5 \mu\text{m}$ ) and cannot be shown in the model. Therefore, these cracks manifest themselves as strength and stiffness reductions in individual lattice element instead of being explicitly shown in the model. At the moment the cracks are observed in the model, significant damage has already been accumulated in the system. In addition, it can also be seen that some initial cracks are impeded by the HD C-S-H at the bottom-left corner of the sample. With the increasing number of loading cycles, the fatigue crack tends to propagate following the edge of the HD C-S-H and UHC. This is because at the low stress level the fatigue damage evolution rates for two C-S-H phases

are significantly different. The damage accumulates much faster in the LD C-S-H phase and, consequently, most of this phase has already been damaged before the fatigue failure. It is also found that the number of completely damaged elements ( $D=1$ ) in this fatigue simulation is almost 1.62 times higher than that in static fracture simulations. Therefore, different degrees of damage in the microstructure pattern lead to the final fatigue fracture pattern, which is different from the static fracture pattern.



(a) Stress level of 85%



(b) Stress level of 50%

Figure 5-17 Different fatigue fracture behaviours of cement pastes (w/c 0.4) under the (a) stress level of 85% (fatigue life  $N_f=3053$ ); and (b) the stress level of 50% (fatigue life  $N_f=3572216$ )

Normally, the output of microscopic simulation results of cement pastes, e.g.  $S-N$  curves and fatigue damage evolutions, could be used as inputs for macroscopic fatigue simulation of concrete. Similar to the static fracture multiscale modelling scheme [18,19], different fatigue properties should be assigned to different components in concrete. Since another major component of concrete, i.e. ITZ, is also crucial for its macroscopic fatigue behaviour, the microscopic fatigue behaviour of ITZ will be simulated in Chapter 6.

## 5.5 CONCLUSIONS

In this chapter, a 2D lattice fatigue model has been used to investigate the fatigue behaviour of cement paste at the microscale. The experimental results for flexural fatigue of cement paste specimens of the same size ( $300 \times 300 \times 1650 \mu\text{m}^3$ ) as considered in Chapter 3 are used to calibrate and validate the model. The following conclusions can be drawn:

- (1) In the current model the pre-peak fatigue damage evolution is applied to local elements based on the combined phenomenological  $S-N$  approach and Miner's law. The post-peak fatigue damage is considered using a cyclic constitutive law. Different fatigue damage evolution rates are assumed for various microscopic constituents of cement paste. In addition, the development of residual deformation can also be simulated by considering the creep and fatigue compliance of C-S-H phases. Overall, the proposed model can reproduce the experimental results quite well in terms of  $S-N$  curve, stiffness degradation and residual deformation.
- (2) The validated model is then utilized to predict the uniaxial tensile fatigue fracture process of cement paste. The effects of stress level and heterogeneity of the microstructure on the fatigue fracture pattern can be properly studied with the model. The major source of scatter of fatigue results originated from the heterogeneity of the microstructure can be demonstrated clearly with the simulations. Combined with static fracture simulations, the simulations offer the opportunity to directly compare the static and fatigue fracture behaviour. It is found that the concurrent propagation of multiple cracks, other than a single crack in 2D static fracture simulation, is possible for the 2D fatigue simulation.
- (3) A major limitation of the current model is its 2D nature, which is unable to consider the 3D features of fatigue fracture behaviour in heterogeneous materials. Therefore, it is necessary to extend the current model to 3D simulations in a future study. Another limitation is the inherent empirical nature for the estimation of fatigue damage evolution, which lacks sufficient physical justification. A clear physical explanation for the microscopic fatigue fracture may only exist on the atomic scale, where the propagation of the fatigue crack is assumed to be governed by the thermally activated breakage of atomic bonds [56]. Nevertheless, the current model has successfully demonstrated the effect of heterogeneity of the microstructure on the fatigue behaviour of cement paste in a very efficient way and provides some valuable insights into the microscopic fatigue fracture phenomenon.

With the aid of the developed model, it is possible to predict the fatigue life of the cement paste for a given microstructure. The next chapter will focus on the fatigue

simulation of ITZ using the proposed model. Moreover, the output of simulation results at the microscale could be used as input for the prediction of the mesoscopic fatigue of mortar, which will be performed in Chapter 7.

## REFERENCES

- [1] K.M. Simon, J.M. Chandra Kishen, A multiscale approach for modeling fatigue crack growth in concrete, *Int. J. Fatigue*. 98 (2017) 1–13.
- [2] C. Pichler, R. Lackner, Identification of logarithmic-type creep of calcium-silicate-hydrates by means of nanoindentation, *Strain*. 45 (2009) 17–25.
- [3] K. Van Breugel, Concrete: A material that barely deserves that qualification, in: *Int. RILEM Conf. Mater. Sci.*, RILEM Publications SARL, 2010: pp. 13–32.
- [4] H. Zhang, Y. Xu, Y. Gan, Z. Chang, E. Schlangen, B. Šavija, Microstructure informed micromechanical modelling of hydrated cement paste: Techniques and challenges, *Constr. Build. Mater.* 251 (2020) 118983.
- [5] F. Gong, T. Ueda, Y. Wang, D. Zhang, Z. Wang, Mesoscale simulation of fatigue behavior of concrete materials damaged by freeze-thaw cycles, *Constr. Build. Mater.* 144 (2017) 702–716.
- [6] M. Corrado, J.F. Molinari, Effects of residual stresses on the tensile fatigue behavior of concrete, *Cem. Concr. Res.* 89 (2016) 206–219.
- [7] L.P. Guo, A. Carpinteri, A. Spagnoli, W. Sun, Experimental and numerical investigations on fatigue damage propagation and life prediction of high-performance concrete containing reactive mineral admixtures, *Int. J. Fatigue*. 32 (2010) 227–237.
- [8] H.J. Herrmann, S. Roux, *Statistical models for the fracture of disordered media*, Elsevier, 2014.
- [9] E. Schlangen, E.J. Garboczi, Fracture simulations of concrete using lattice models: computational aspects, *Eng. Fract. Mech.* 57 (1997) 319–332.
- [10] E. Schlangen, J.G.M. van Mier, Simple lattice model for numerical simulation of fracture of concrete materials and structures, *Mater. Struct.* 25 (1992) 534–542.
- [11] J.G.M. Van Mier, *Concrete fracture: a multiscale approach*, CRC press, 2012.
- [12] H.K. Man, J.G.M. Van Mier, Damage distribution and size effect in numerical concrete from lattice analyses, *Cem. Concr. Compos.* 33 (2011) 867–880.
- [13] H. Zhang, Y. Gan, Y. Xu, S. Zhang, E. Schlangen, B. Šavija, Experimentally informed fracture modelling of interfacial transition zone at micro-scale, *Cem. Concr. Compos.* 104 (2019).
- [14] M. Luković, B. Šavija, E. Schlangen, G. Ye, K. van Breugel, A 3D lattice modelling study of drying shrinkage damage in concrete repair systems, *Materials (Basel)*. 9 (2016) 9–13.
- [15] Y. Gan, C. Romero Rodriguez, H. Zhang, E. Schlangen, K. van Breugel, B. Šavija, Modeling of microstructural effects on the creep of hardened cement paste using an experimentally informed lattice model, *Comput. Civ. Infrastruct. Eng.* 36 (2021) 560–576.
- [16] B. Šavija, M. Luković, E. Schlangen, Lattice modeling of rapid chloride migration in concrete, *Cem. Concr. Res.* 61–62 (2014) 49–63.
- [17] H. Zhang, B. Šavija, S.C. Figueiredo, M. Lukovic, E. Schlangen, Microscale testing and modelling of cement paste as basis for multi-scale modelling, *Materials (Basel)*. 9 (2016).
- [18] H. Zhang, B. Šavija, M. Luković, E. Schlangen, Experimentally informed micromechanical modelling of cement paste: An approach coupling X-ray computed tomography and statistical nanoindentation, *Compos. Part B Eng.* 157 (2019) 109–122.
- [19] H. Zhang, B. Šavija, S.C. Figueiredo, E. Schlangen, Experimentally validated multi-scale modelling scheme of deformation and fracture of cement paste, *Cem. Concr. Res.* 102 (2017) 175–186.



- [20] H. Zhang, B. Šavija, Y. Xu, E. Schlangen, Size effect on splitting strength of hardened cement paste: Experimental and numerical study, *Cem. Concr. Compos.* 94 (2018) 264–276.
- [21] H. Zhang, B. Šavija, E. Schlangen, Combined experimental and numerical study on micro-cube indentation splitting test of cement paste, *Eng. Fract. Mech.* 199 (2018) 773–786.
- [22] K. Van Breugel, Simulation of hydration and formation of structure in hardening cement-based materials., (1993).
- [23] S. Bishnoi, K.L. Scrivener,  $\mu$ ic: A new platform for modelling the hydration of cements, *Cem. Concr. Res.* 39 (2009) 266–274.
- [24] D.P. Bentz, Modeling the influence of limestone filler on cement hydration using CEMHYD3D, *Cem. Concr. Compos.* 28 (2006) 124–129.
- [25] H.S. Wong, M.K. Head, N.R. Buenfeld, Pore segmentation of cement-based materials from backscattered electron images, *Cem. Concr. Res.* 36 (2006) 1083–1090.
- [26] P.D. Tennis, H.M. Jennings, A model for two types of calcium silicate hydrate in the microstructure of Portland cement pastes, *Cem. Concr. Res.* 30 (2000) 855–863.
- [27] H. Zhang, B. Šavija, E. Schlangen, Towards understanding stochastic fracture performance of cement paste at micro length scale based on numerical simulation, *Constr. Build. Mater.* 183 (2018) 189–201.
- [28] M. Yip, J. Mohle, J.E. Bolander, Automated modeling of three-dimensional structural components using irregular lattices, *Comput. Civ. Infrastruct. Eng.* 20 (2005) 393–407.
- [29] Z. Qian, Multiscale modeling of fracture processes in cementitious materials, Delft University of Technology, PhD Thesis, 2012.
- [30] E. Schlangen, Experimental and numerical analysis of fracture process in concrete, *Heron.* 38 (1993) 1–17.
- [31] H. Zhang, Y. Xu, Y. Gan, Z. Chang, E. Schlangen, B. Šavija, Combined experimental and numerical study of uniaxial compression failure of hardened cement paste at micrometre length scale, *Cem. Concr. Res.* 126 (2019).
- [32] G. Lilliu, 3D analysis of fracture processes in concrete, Eburon Uitgeverij BV, 2007.
- [33] J. Qiu, E. Yang, Micromechanics-based investigation of fatigue deterioration of engineered cementitious composite (ECC), *Cem. Concr. Res.* 95 (2017) 65–74.
- [34] Q. Li, B. Huang, S. Xu, B. Zhou, R.C. Yu, Compressive fatigue damage and failure mechanism of fiber reinforced cementitious material with high ductility, *Cem. Concr. Res.* 90 (2016) 174–183.
- [35] K. Nagai, Y. Sato, T. Ueda, Mesoscopic Simulation of Failure of Mortar and Concrete by 2D RBMSM, 2 (2004) 359–374.
- [36] D. Hordijk, Local approach to fatigue of concrete, PhD Thesis, Delft Univ. Technol. (1991) 216.
- [37] Y. Gan, H. Zhang, Y. Zhang, Y. Xu, E. Schlangen, K. van Breugel, B. Šavija, Experimental study of flexural fatigue behaviour of cement paste at the microscale, *Int. J. Fatigue.* 151 (2021).
- [38] Y. Gan, H. Zhang, B. Šavija, E. Schlangen, K. van Breugel, Static and fatigue tests on cementitious cantilever beams using nanoindenter, *Micromachines.* 9 (2018).
- [39] T.T.C. Hsu, Fatigue and microcracking of concrete, *Matériaux Constr.* 17 (1984) 51–54.
- [40] T.T.C. Hsu, Fatigue of Plain Concrete, *ACI J. Proc.* 78 (1981) 292–304.
- [41] E.W.C. Wilkins, Cumulative damage in fatigue, in: *Colloq. Fatigue/Colloque Fatigue/Kolloquium Über Ermüdungsfestigkeit*, Springer, 1956: pp. 321–332.
- [42] J.O. Holmen, Fatigue of Concrete by Constant and Variable Amplitude Loading, *ACI*

- Spec. Publ. 75 (1982) 71–110.
- [43] K. Matsumoto, Y. Sato, T. Ueda, L. Wang, Mesoscopic analysis of mortar under high-stress creep and low-cycle fatigue loading, *J. Adv. Concr. Technol.* 6 (2008) 337–352.
- [44] W. Schlitz, A history of fatigue, *Eng. Fract. Mech.* 54 (1996) 263–300.
- [45] K. Keerthana, J.M. Chandra Kishen, An experimental and analytical study on fatigue damage in concrete under variable amplitude loading, *Int. J. Fatigue.* 111 (2018) 278–288.
- [46] K.M.P. Fathima, J.M.C. Kishen, A thermodynamic framework for the evolution of damage in concrete under fatigue, *Arch. Appl. Mech.* 85 (2015) 921–936.
- [47] B. Sun, Z. Xu, An efficient numerical method for meso-scopic fatigue damage analysis of heterogeneous concrete, *Constr. Build. Mater.* 278 (2021) 122395.
- [48] H.W. Reinhardt, H.A.W. Cornelissen, Post-peak cyclic behaviour of concrete in uniaxial tensile and alternating tensile and compressive loading, *Cem. Concr. Res.* 14 (1984) 263–270.
- [49] Z.P. Bazant, M.H. Hubler, Theory of cyclic creep of concrete based on Paris law for fatigue growth of subcritical microcracks, *J. Mech. Phys. Solids.* 63 (2014) 187–200.
- [50] Y. Gan, M. Vandamme, H. Zhang, Y. Chen, E. Schlangen, K. van Breugel, B. Šavija, Micro-cantilever testing on the short-term creep behaviour of cement paste at micro-scale, *Cem. Concr. Res.* 134 (2020) 1–26.
- [51] Y. Gan, C.R. Rodriguez, E. Schlangen, K. van Breugel, B. Šavija, Assessing strain rate sensitivity of cement paste at the micro-scale through micro-cantilever testing, *Cem. Concr. Compos.* 121 (2021).
- [52] K. Kirane, Z.P. Bazant, Size effect in Paris law and fatigue lifetimes for quasibrittle materials: Modified theory, experiments and micro-modeling, *Int. J. Fatigue.* 83 (2016) 209–220.
- [53] R.R. Pedersen, A. Simone, M. Stroeve, L.J. Sluys, Mesoscopic modelling of concrete under impact, *Proc. 6th Int. Conf. Fract. Mech. Concr. Concr. Struct. - Fract. Mech. Concr. Concr. Struct.* 1 (2007) 571–578.
- [54] Y. Gan, M. Vandamme, Y. Chen, E. Schlangen, K. van Breugel, B. Šavija, Experimental investigation of creep recovery of cement paste at the microscale, *Cem. Concr. Res.* (n.d.).
- [55] Z.P. Bazant, K. Xu, Size effect in fatigue fracture of concrete, *ACI Mater. J.* 88 (1991) 390–399.
- [56] J.-L. Le, Z.P. Bazant, Unified nano-mechanics based probabilistic theory of quasibrittle and brittle structures: II. Fatigue crack growth, lifetime and scaling, *J. Mech. Phys. Solids.* 59 (2011) 1322–1337.
- [57] J.L. Le, J. Manning, J.F. Labuz, Scaling of fatigue crack growth in rock, *Int. J. Rock Mech. Min. Sci.* 72 (2014) 71–79.
- [58] A. Toumi, A. Bascoul, A. Turatsinze, Crack propagation in concrete subjected to flexural- cyclic loading, *Mater. Struct.* 31 (1998) 451–458.
- [59] L.P. Guo, A. Carpinteri, R. Roncella, A. Spagnoli, W. Sun, S. Vantadori, Fatigue damage of high performance concrete through a 2D mesoscopic lattice model, *Comput. Mater. Sci.* 44 (2009) 1098–1106.
- [60] K.M. Simon, J.M.C. Kishen, Influence of aggregate bridging on the fatigue behavior of concrete, *Int. J. Fatigue.* 90 (2016) 200–209.
- [61] M. Saito, Characteristics of microcracking in concrete under static and repeated tensile loading, *Cem. Concr. Res.* 17 (1987) 211–218.
- [62] J. Zhang, V.C. Li, H. Stang, Size effect on fatigue in bending of concrete, *J. Mater. Civ. Eng.* 13 (2001) 446–453.



# 6

## LATTICE MODELLING OF FATIGUE RESPONSE OF ITZ AT MICROSCALE

*In this chapter the fatigue behaviour of the interfacial transition zone (ITZ) at the microscale is investigated using the fatigue lattice model presented in Chapter 5. Microstructures of ITZ obtained from X-ray computed tomography (XCT) tests are explicitly considered in the model. Local mechanical and fatigue properties of different phases in the ITZ are calibrated and validated using the experimental results obtained at the same length scale. The simulation provides a satisfactory prediction of fatigue behaviour of the ITZ with different w/c ratios. The validated model is then used to predict the uniaxial tensile fatigue fracture of the ITZ. The effect of microscopic roughness on the overall fatigue behaviour is studied using the proposed model.*

## 6.1 INTRODUCTION

The interfacial transition zone (ITZ) between aggregate and paste matrix plays a vital role in the fracture behaviour of mortar and concrete subjected to static and fatigue loading. To properly simulate the mesoscopic fatigue behaviour of mortar, a micro-scale constitutive model of ITZ is needed. In this chapter, the mechanical and fatigue behaviour of the ITZ at the microscale are simulated using the fatigue lattice modelling approach developed in previous chapter. Realistic ITZ microstructures obtained from XCT results are implemented into the model. The experimental results of the performance of the ITZ taken from the Chapter 4 are used to calibrate and validate the model. To investigate the effect of microscopic roughness of the aggregate surface on the overall mechanical and fatigue performance, uniaxial tensile simulations of ITZ virtual samples with different roughness are also performed. The predicted micromechanical and fatigue properties of the ITZ can be further used in the modelling of concrete or mortar at the meso-scale, which will be presented in Chapter 7.

## 6.2 NUMERICAL APPROACH

### 6.2.1 2D ITZ VIRTUAL SPECIMENS

To investigate the effect of micro-roughness on the overall mechanical performance of the ITZ, two types of aggregate surfaces, i.e. artificial flat surface and natural rough surface, are prepared using the quartzite aggregate. For the flat aggregate, miniature ITZ specimens with two w/c ratios (0.3 and 0.4) as discussed in Chapter 4 are scanned by a Micro CT-Scanner to obtain a realistic microstructure. In this case, an aggregate is first cut and ground to obtain a flat surface using a Minitom low-speed cutting machine and a Struers Labopol-5 thin sectioning machine. Another aggregate with a natural rough surface is only cleaned without grinding. All aggregate samples are then dried in an oven (60°C) for 48 hours. After cooling down to the room temperature, the fresh paste is then cast on the aggregate surface. After sealed curing for 28 days, the ITZ specimens with the flat aggregate are cut by a precision micro-dicing machine (MicroAce Series 3 Dicing Saw) to generate micro-cantilever ITZ beams with a square cross section of  $150 \times 150 \mu\text{m}^2$ . The cantilevered length of the beam is  $750 \pm 45 \mu\text{m}$ , see Figure 6-1. For more details regarding the preparation process of miniature ITZ specimens, the reader is referred to Chapter 4. In addition, two large ITZ prisms (w/c 0.4) with the size of around  $1 \times 1 \times 1.5 \text{ mm}^3$  containing rough aggregate surfaces are prepared using the similar cutting procedure. The prepared ITZ samples are scanned by XCT to obtain greyscale-based 2D images, see Figure 6-2. The X-ray source tube used for ITZ cantilever beams is set at 90 kV/170  $\mu\text{A}$  during scanning, which results in a voxel resolution of  $0.5 \times 0.5 \times 0.5 \mu\text{m}^3$ . For ITZ prisms, the X-ray source tube is set at 90 kV/110  $\mu\text{A}$  resulting in a voxel resolution of  $1.5 \times 1.5 \times 1.5 \mu\text{m}^3$ . According to the

experimental observations in Chapter 4, the width of the ITZ is only around 30-100  $\mu\text{m}$ . Therefore, a finer element size instead of 5  $\mu\text{m}$  is preferred to properly consider the microstructural features in the interfacial zone. The spatial resolution of XCT images is then merged to 2.5  $\mu\text{m}/\text{pixel}$  using the bilinear interpolation algorithm. As a result, the element size for ITZ simulation is 2.5  $\mu\text{m}$ . Note that in the uniaxial fatigue tensile simulation, the size of the ITZ sample is  $500 \times 500 \mu\text{m}^2$ , which is consistent with the size of cement paste virtual samples in Chapter 5.

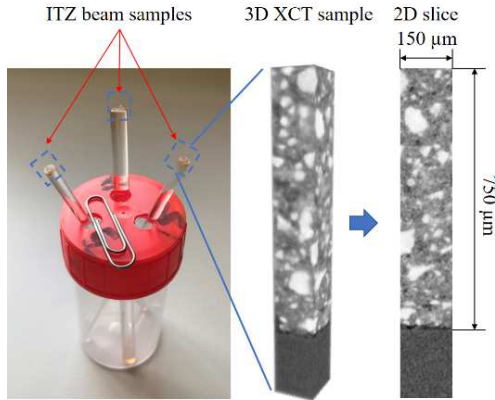


Figure 6-1 The 3D XCT results of w/c 0.3 ITZ beam samples and 2D slices

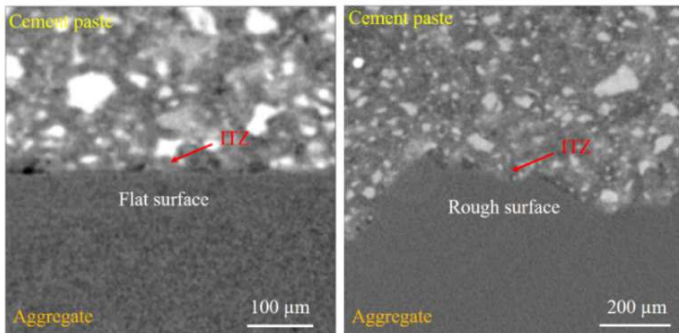


Figure 6-2 The 2D XCT images of w/c 0.4 paste-aggregate composites with different aggregate surfaces

## 6.2.2 LATTICE MODELLING OF ITZ

For modelling of the ITZ the modelling approach presented in Chapter 4 is used. For ITZ simulation, the same global thresholding approach in Chapter 5 is used to segment four phases (i.e. LD C-S-H, HD C-S-H, UHC and pore) in 2D images randomly selected from XCT results. Three threshold values for pore, low density C-S-H (LD C-S-H) and high density C-S-H (HD C-S-H) are defined based on the grey-scale histogram. More details of the segmentation procedure can be found in Chapter 5. After specifying the surface texture of aggregate, hydration products that are in contact with the aggregate surface are defined as interfacial elements. Therefore, mainly two interfacial elements can be detected, i.e. aggregate-LD C-S-H and aggregate-HD C-S-H. In total, ten types of elements are used in the ITZ model, see Table 6-2. Note that the interfacial bonding between the aggregate and (unhydrated cement) UHC is assumed to be extremely weak and can be neglected. Its strength and elastic modulus are assumed to be as low as 0.0001 MPa and 0.0001 GPa, respectively. In addition, all elements connecting to pores are considered as pore elements, which have zero strength and stiffness. Therefore, they are removed from the mesh to avoid the singularities when assembling the global stiffness matrix, see Figure 6-3.

Two types of model are generated: the first is the ITZ beam model with the size of  $150 \times 750 \mu\text{m}^2$ , which is utilized for the calibration and validation of the model simulation output with experimental results. The second is the ITZ model with the size of  $500 \times 500 \mu\text{m}^2$  containing pure ITZ and aggregate, which is used to predict the uniaxial tensile behaviour of the ITZ. Since the linear elastic aggregate element is assumed not to fail in the model, the part of the ITZ model that only contains the aggregate is removed and the model is resized to  $500 \times 250 \mu\text{m}^2$  to save computation time. Figure 6-4 shows the generated lattice models for two types of aggregate surface. For quantitative characterization of the surface texture, the arithmetic average roughness ( $R_a$ ) is calculated for each ITZ model and summarized in Table 6-4. In order to evaluate the sole effect of aggregate surface roughness, a homogenized paste using only LD C-S-H phase is also generated for the ITZ model, see Figure 6-4.

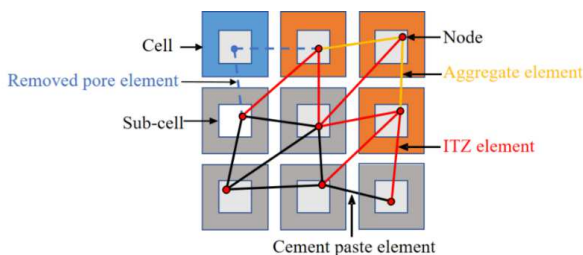


Figure 6-3 Lattice element generation procedure (grey pixel represents cement paste, orange represents aggregate and blue represents pore)

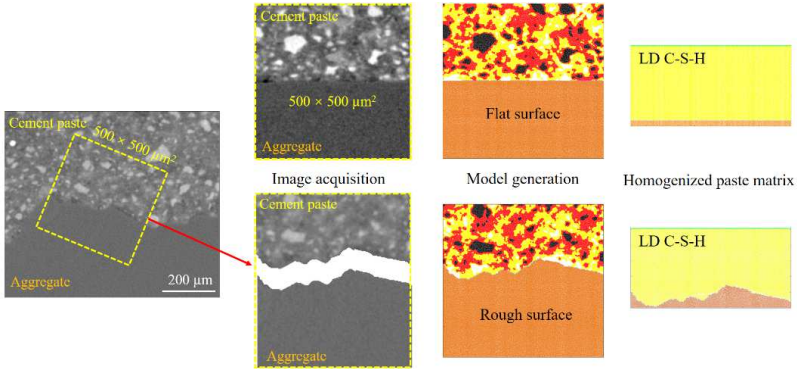


Figure 6-4 Generation lattice model based on 2D images of ITZ microstructures with different surface textures (black pixel represents UHC, orange represents aggregate, yellow represents LD C-S-H and red represents HD C-S-H)

For the static fracture simulation, a set of linear elastic analyses is performed by calculating the comparative stress within each element using Eq.(5-1). Details about the numerical algorithm of fatigue simulation can be found in Chapter 5. The local mechanical properties of different phases are determined by fitting with experimental results presented in Chapter 4. For the fatigue simulation, the same cyclic constitutive law for the cement paste elements presented in Chapter 5 are used here and will be recalibrated for interfacial elements using testing results of ITZ beams. At each analysis step, the maximum fatigue load is imposed on the composite system. The fatigue damage in all elements is calculated based on the local stress and number of cycles. A thousand cycles are initially considered as one loading case using the 'block cycle jump' technique described in Chapter 5. The value of a cycle block will be adjusted until it is at least ten times lower than the simulated fatigue life. A post-peak cyclic softening behaviour is also assumed for the ITZ element. Four softening steps are required for an element to reach final fracture. At each softening step, the percentage of reduction in strength  $d_{\text{soft}}$  is assumed to be 20% for all interfacial elements. Following the approach described in Chapter 5, a constant strain ( $\epsilon_c = -400 \mu\epsilon$ ) at the compression branch is introduced for all phases to determine the reduction percentage of the elastic moduli and the residual strains (e.g.  $\epsilon_{p1}$  and  $\epsilon_{p2}$ ) using Eq.(5-4) and Eq.(5-5). Note that the UHC and aggregate phase are both assumed to have infinite fatigue life without any fatigue damage accumulation. Only the two C-S-H phases in the cement paste and the corresponding interfacial elements are assumed to experience fatigue damage. After one loading cycle, the system will be updated in consideration of the new stiffness matrix and local strength. If the global stiffness of the whole system falls below 20% of its original stiffness, the simulation is stopped and the total number of cycles is assumed to be the final fatigue life. Otherwise, another analysis step is executed.



### 6.3 MODEL CALIBRATION AND VALIDATION

The calibration of the ITZ model is performed by comparing the numerical results with experimental results. For local mechanical properties, static flexural bending tests on micro-cantilever beams described in Chapter 4 are used. The boundary conditions in the simulation are the same as those in the experiments, as is illustrated in Figure 6-5. The local mechanical properties of three components (i.e. LD C-S-H, HD C-S-H and UHC) derived in the Chapter 5 are directly used herein. For calibration of two interfacial phases (aggregate-LD C-S-H and aggregate-HD C-S-H), three sets of parameters as listed in Table 6-1 are evaluated. The simulated results are compared for investigating the effect of local mechanical properties on the overall fracture behaviour and to determine the parameters fitted best with experimental results.

Table 6-1 Local properties for different interfacial phases

Interfacial phases	Aggregate-LD C-S-H		Aggregate-HD C-S-H	
	$E$ (GPa)	$f_t$ (MPa)	$E$ (GPa)	$f_t$ (MPa)
Case 1	0.2	4.3	0.3	6.0
Case 2	0.2	13.0	0.3	18.0
Case 3	0.2	21.6	0.3	30.0

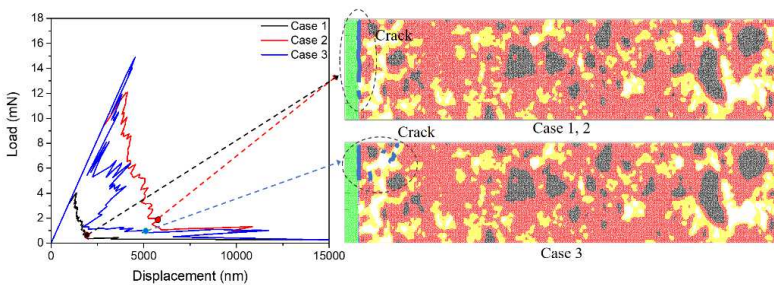
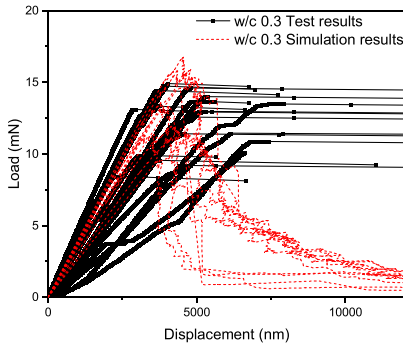


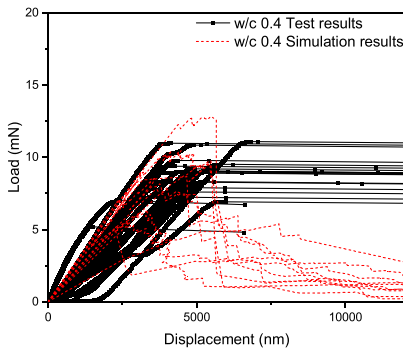
Figure 6-5 Comparison of simulated load-displacement curves and fracture patterns of ITZ beams with the w/c ratio of 0.3 using three different sets of local mechanical properties, see Table 6-1

Figure 6-5 shows the simulated load-displacement curves and corresponding fracture patterns at certain analysis steps. Both the interfacial strengths assumed in Case 1 and 2 are much lower than the strength of the hydration products (i.e. 52.2 MPa).

Therefore, a similar fracture pattern is observed in both cases, where the critical crack is generated along the interface. Moreover, since the assumed elastic moduli in both cases are identical and the fracture patterns are similar, the obtained load-displacement curves, especially in the post-peak stage, also resemble each other qualitatively. The strength assumed in Case 3 is relatively close to that of the hydration products. A strong interfacial bonding allows the crack to penetrate into the interfacial transition zone, as is shown in Figure 6-5. As a result, the maximum load calculated in Case 3 is controlled by the local microstructure of the ITZ. In this case, the global strength only increase slightly compared to Case 2 due to the local high porosity.



(a) w/c 0.3



(b) w/c 0.4

Figure 6-6 Comparison of experimentally measured load-displacement curves and simulation results of (a) w/c 0.3 and (b) w/c 0.4

From the simulation of ten virtual samples with w/c ratio 0.3, it is found that the simulated load-displacement curves using the local properties in Case 2 agree well with the experimental results, see Figure 6-6(a). Moreover, when the same local properties are used in the w/c 0.4 virtual samples with different microstructures, the obtained load-displacement results still correspond well with the experimental results. Therefore, the local elastic moduli  $E_n$  and tensile strengths  $f_t$  of all element types are settled and summarized in Table 6-2. The determined local mechanical properties will also serve as the initial properties in the following fatigue simulations.

Table 6-2 Local mechanical properties of different phases in paste-aggregate composite

Element type	Phase 1	Phase 2	$f_t$ (MPa)	$E_n$ (GPa)
U-U	UHC	UHC	614.7	84.2
L-L	LD C-S-H	LD C-S-H	52.2	21.3
H-H	HD C-S-H	HD C-S-H	82.8	26.4
L-H	LD C-S-H	HD C-S-H	52.2	21.3
U-L	UHC	LD C-S-H	52.2	21.3
U-H	UHC	HD C-S-H	82.8	26.4
A-A	Aggregate	Aggregate	700	70
A-U	Aggregate	UHC	0.0001	0.0001
A-L	Aggregate	LD C-S-H	13	0.2
A-H	Aggregate	HD C-S-H	18	0.3

For calibration of parameters related to the fatigue damage evolution (i.e. fatigue parameter  $a$  and  $b$ ), fatigue testing results of ITZ beams reported in Chapter 4 are used. The local fatigue parameters of main hydration products in hardened cement paste determined in the previous chapter are directly employed here. In the calibration process, in total 13 sets of fatigue parameters for two interfacial element types are evaluated. Figure 6-7 presents the simulated  $S-N$  curves and the comparison with experimental results. With the change of local fatigue properties, the slopes of simulated  $S-N$  curves vary significantly. Generally, the increase of the value of parameter  $a$  compromises the fatigue resistance, whilst the obtained fatigue life is increased with the increasing of the value of  $b$ , as discussed in Chapter 5. However, the parameter  $b$  seems to have minor influence on the global fatigue performance in comparison with the parameter  $a$ . Moreover, in most experimental investigations this value ( $b$ ) is found to be almost constant, i.e. 1.00 to 1.20, for the same material composition [1,2]. The meaning of parameter  $b$  could be interpreted as the ratio of strength subjected to one fatigue loading cycle and the static strength. This value is usually larger than 1 suggesting that the sample's strength under the fatigue loading is higher than the strength measured under the quasi-static loading. This enhanced

strength is probably due to the increased loading rate in the fatigue loading protocol [3]. Herein, the parameter  $b$  is kept constant for both interface elements. It can be seen from Figure 6-7 that the parameter combination  $a(\text{LD})=0.09$ ,  $a(\text{HD})=0.07$  and  $b=1.05$  results in a  $S$ - $N$  curve most close to experimental results. Therefore, this parameter combination is adopted in subsequent simulations.

It is important to note that a large scatter observed in fatigue tests may arise from the stochastic nature of the cementitious materials. It has been proved that the stochastic mechanical properties of cement paste can be simulated by lattice fracture model using microstructures randomly extracted from XCT images [4]. By explicitly considering heterogeneous microstructures, the deterministic values of micromechanical parameters are used here as inputs for the sake of simplicity. An alternative solution is to introduce probability distribution of local properties [5].

It needs to be clarified that due to the lack of available experimental data on the creep behaviour of ITZ at the microscale, the calibration of parameters related to the residual deformation is not performed in current ITZ model. Moreover, since the incremental residual deformation at each step is very small, it is believed that the absence of residual deformation accumulation may have negligible effect on the simulated fatigue fracture behaviour. This calibration procedure will be performed in future work.

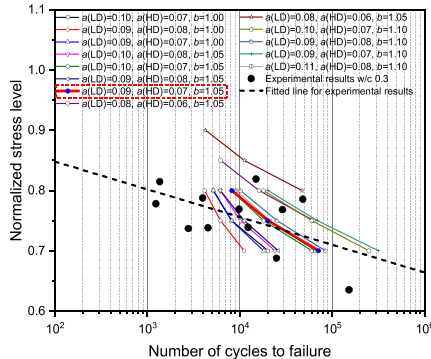
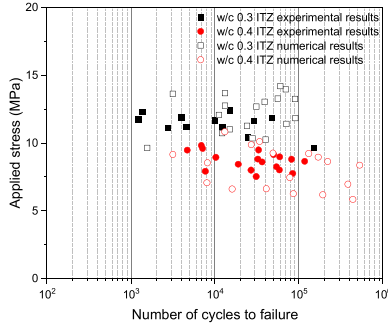


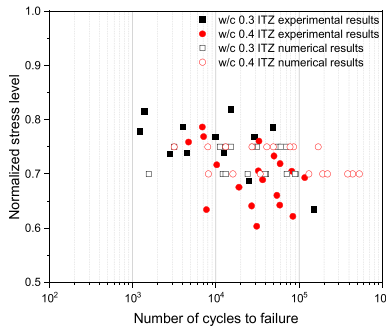
Figure 6-7 Simulated  $S$ - $N$  results using 13 different sets of local fatigue properties and the comparison with experimental results in Chapter 4

The local fatigue parameters for different phases are summarized in Table 6-3. Assuming elastic-brittle behaviour of hydration products at the microscale, the maximum strain  $\varepsilon_{\text{max}}$  for each phase is slightly larger than the ratio between the strength and elastic modulus. The  $S$ - $N$  curves for ten virtual ITZ beams with different  $w/c$  ratios are simulated and shown in Figure 6-8. Due to the high scatter, it is difficult to see the difference between the fatigue strengths for two  $w/c$  ratios. By plotting the

fatigue life against the applied stress magnitude (Figure 6-8(a)), it can be seen that for a given number of cycles a higher stress level is needed to reach the failure of the samples with a lower w/c ratio. Overall, the simulated fatigue life of pastes for both w/c ratios match well with experimental results. Note that in the simulations, the scatter in the simulated fatigue life can only be attributed to the variation in microstructure. Even though other sources of scatter are not considered in this study, the simulated scatter is quite close to the experimental observations.



(a) Applied stress magnitude-fatigue life curves



(b) Stress level-fatigue life curves

Figure 6-8 The simulated results of (a) applied stress magnitude-fatigue life curves and (b) stress level-fatigue life curves

Figure 6-9 shows the changes of the stiffness of all virtual samples with increasing load cycles, which indicates the fatigue damage evolution. Basically, three stages can be

detected. The initial stage, which is characterised by a small reduction of stiffness, accounting for less than 10% of fatigue life. This stage is determined by the initiation of cracks around stress concentrators in the ITZ. Next, the degradation of stiffness reaches a plateau, which lasts most of the fatigue life. During this stage, the fatigue damage accumulation is relatively small. At the third stage, a sudden drop of stiffness occurs, which can be attributed to unstable cracking. This is similar to the experimental observations reported in Chapter 4. In addition, the percentage of stiffness reduction, especially in the initial stage, seems to be larger in pastes with higher w/c ratio. When compared with the stiffness degradation in cement paste (Figure 5-13), the fatigue damage evolution in the ITZ is much faster. This could explain the significant stiffness degradations observed in most macroscopic fatigue tests on mortar or concrete samples [2,6,7], where damage initiates in the ITZ.

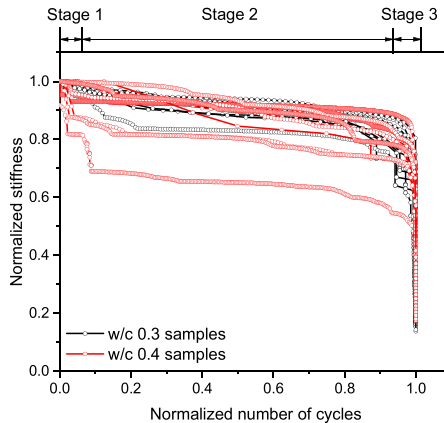


Figure 6-9 The simulated evolution of sample stiffness

Table 6-3 Local fatigue parameters of different phases in paste-aggregate composite

Element type	Phase 1	Phase 2	a	b	$\epsilon_{\max}$
L-L	LD C-S-H	LD C-S-H	0.04	1.10	3200
H-H	HD C-S-H	HD C-S-H	0.02	1.10	3200
L-H	LD C-S-H	HD C-S-H	0.04	1.10	3200
U-L	UHC	LD C-S-H	0.04	1.10	3200
U-H	UHC	HD C-S-H	0.02	1.10	3200
A-L	Aggregate	LD C-S-H	0.09	1.05	2100
A-H	Aggregate	HD C-S-H	0.07	1.05	2100

## 6.4 UNIAXIAL TENSILE SIMULATION OF ITZ

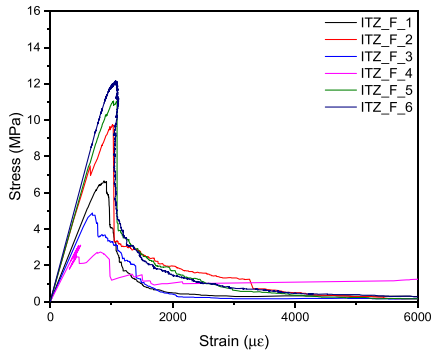
ITZ microstructures generated in Section 6.2.2 are used in the simulation of the performance of the ITZ under uniaxial tension. The aim of the uniaxial tensile test is to obtain homogenized mechanical and fatigue properties of the ITZ at the microscale. The outcome of these simulations will serve as inputs in meso-scale simulation of mortar (Chapter 7). In the uniaxial tensile simulations, the bottom of aggregate is fixed and the nodal load is applied to the top of cement paste. The calibrated local properties listed in Table 6-2 and Table 6-3 are used. The influence of surface roughness of aggregate on the overall mechanical and fatigue properties is also analysed. Table 6-4 summaries all the features of the ITZ models. The simulated stress-strain curves are presented in Figure 6-10. For both surface types, the highest uniaxial strength can be found in the ITZ models with the homogenized paste matrix (zero porosity). As expected, the uniaxial tensile strength decreases with increasing porosity of the paste. By comparing the results using two types of surfaces, it is found that the rough surface exhibits a higher tensile strength when the heterogeneity of the ITZ microstructure is not considered. However, the correlation between the roughness parameter and the uniaxial tensile strength is not apparent when comparing the simulation results from ITZ\_R\_6 to R\_10. Note that on the one hand irregularities of the rough surface may form nucleation sites for cracks and result in a lower strength. On the other hand, roughness may also promote adhesion and mechanical interlocking leading to a stronger interfacial bonding strength. Moreover, due to the so-called ‘wall effect’ [8], the surface roughness may also affect the strength in a sense of altering the hydration process near the aggregate surface. Therefore, one has to be aware of multiple factors influencing the overall fatigue performance.

In addition, a higher fracture energy (defined as the area under the post-peak stress-strain curve, see Figure 6-10) is always obtained for aggregates with the rough surface. This is because more tortuous cracking paths are generated along the aggregate surfaces, as is shown in Figure 6-11. Similar findings have also been reported in [9]. Despite the effect of roughness, the local distribution of pores generated during hydration also plays an important role in the fracture process, see ITZ\_R\_5 in Figure 6-11. Both the weak adhesion strength and the high local porosity in ITZ lead to the low tensile strength of the ITZ sample.

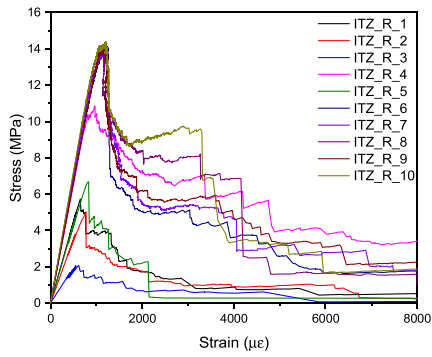
Table 6-4 The summary of ITZ models

Aggregate type	Model	$R_a$ ( $\mu\text{m}$ )	Porosity (%)	Tensile strength (MPa)	Elastic modulus (GPa)
Flat	ITZ_F_1	0	6.60	6.65	8.50
	ITZ_F_2	0	4.84	9.74	11.70
	ITZ_F_3	0	8.31	4.89	7.63
	ITZ_F_4	0	8.60	3.10	6.70
	ITZ_F_5	0	5.91	10.92	11.87
	ITZ_F_6	0	0	11.65	12.72
Rough	ITZ_R_1	14.76	5.75	5.74	8.98
	ITZ_R_2	19.73	9.41	5.03	7.03
	ITZ_R_3	13.24	11.75	2.08	3.94
	ITZ_R_4	9.88	1.80	10.86	13.15
	ITZ_R_5	24.66	9.90	6.69	8.65
	ITZ_R_6	14.76	0	13.05	13.37
	ITZ_R_7	19.73	0	12.61	13.97
	ITZ_R_8	13.24	0	13.32	14.34
	ITZ_R_9	9.88	0	13.83	13.33
	ITZ_R_10	24.66	0	13.02	14.48





(a) Flat aggregate



(b) Rough aggregate

Figure 6-10 The simulated stress-strain diagrams of ITZ models with (a) flat aggregate surfaces and (b) natural rough surfaces under uniaxial tension

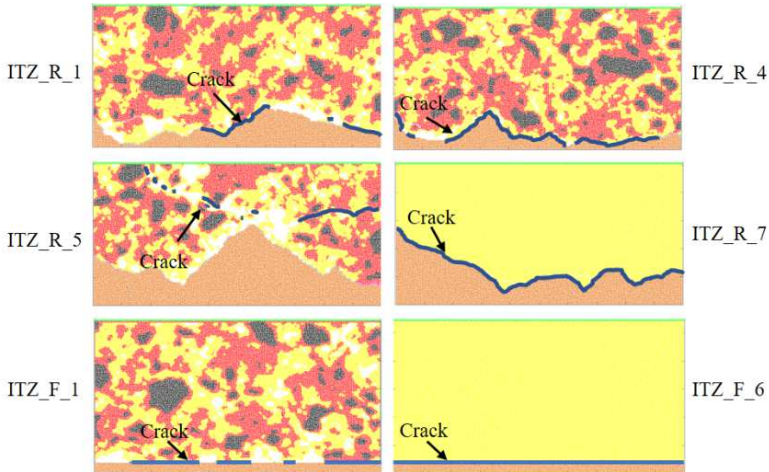
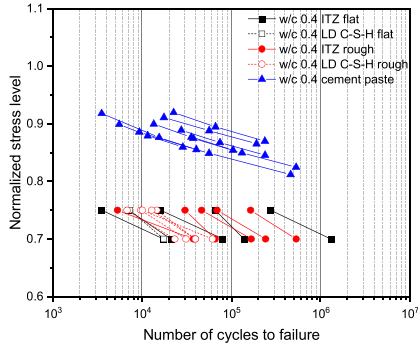
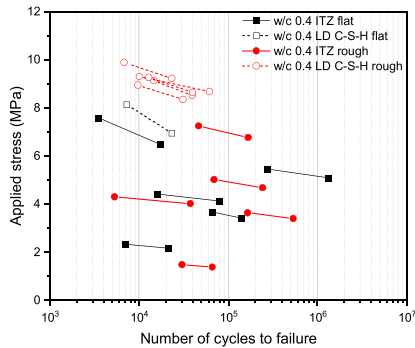


Figure 6-11 The crack patterns for different ITZ models

For the uniaxial tensile fatigue simulations, two stress levels, i.e. 70% and 75% of the tensile strength, are considered in the ITZ models. The calibrated fatigue parameters in Table 6-3 are used. The obtained relationship between the simulated uniaxial tensile fatigue life of ITZ models and the stress level are shown in Figure 6-12. For comparison, the simulation results of cement paste are also presented. It is clear that the fatigue strength of cement paste is much higher than the ITZ indicated by the number of cycles to failure at a given stress level. However, the difference of fatigue properties between two types of ITZ models is not apparent. The fatigue fracture process is governed by the initiation and propagation of cracks. The rough surface of the aggregate leads to more stress concentrations, which may easily initiate cracks. This is shown by the higher percentage reduction of stiffness at the initial stage, as shown in Figure 6-13. However, the propagation of these cracks near stress concentrations may be postponed due to the stress redistribution. The fatigue damage accumulation is then switched to a slow and stable stage. Even though the irregularities of the aggregate surface may accelerate the initiation of cracks, the higher overall strength of ITZ sample with the rough aggregate allows it to sustain a higher stress, and hence a higher degree of fatigue damage. When the fatigue life is plotted against the magnitude of applied stress, see Figure 6-12(b), the model with the rough surface exhibits superior fatigue resistance for the same stress magnitude. This is in accordance with the findings in [10] that the tensile strength and fatigue resistance are positively correlated.

(a)  $S-N$  curves between cement paste and ITZ

(b) The relationship between the applied stress and fatigue life

Figure 6-12(a) The comparison of  $S-N$  curves between cement paste and ITZ; (b) The relationship between the applied stress and number of cycles to failure

The change of stiffness of the virtual ITZ specimen subjected to uniaxial fatigue loading is plotted in Figure 6-13. Similar to previous findings, during most of the fatigue life the stiffness degradation is slow and insignificant. Nevertheless, fatigue damage is accumulating all the time. When the damage has accumulated to a certain degree, unstable cracking occurs leading to the final failure. It has been discussed above that the microstructural features have significant impact on the mechanical properties. Moreover, there is a large difference of fatigue damage evolution between the cement paste and the ITZ. A question is now: how the fatigue damage accumulates in the mortar

or concrete sample, where the cement paste and ITZ work together. This question will be dealt with in the next chapter.

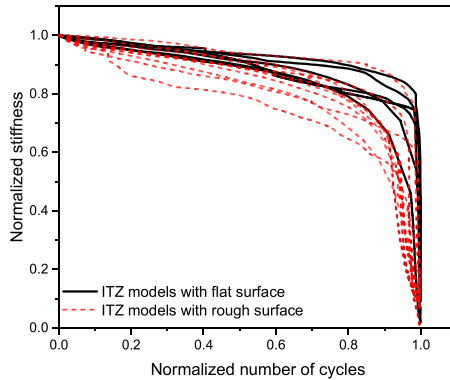


Figure 6-13 The variation of ITZ stiffness during the whole fatigue life under uniaxial tensile fatigue loading

## 6.5 CONCLUSIONS

In this chapter, the 2D lattice fatigue model is used to investigate the fatigue behaviour of microscopic ITZ specimen. The experimental results for flexural fatigue of ITZ at the same length scale in Chapter 4 are used to calibrate and validate the model. The following conclusions can be drawn:

- (1) The calibrated mechanical and fatigue properties of interface elements are used as inputs in ITZ models of specimens made with two different w/c ratios. The simulated mechanical properties and fatigue life for samples with both w/c ratios agree well with experimental results.
- (2) The model is then utilized to predict the uniaxial tensile fracture of cement paste. The effect of surface roughness on the mechanical and fatigue properties is investigated. A higher fracture energy is observed in the ITZ sample with a rough aggregate surface. Both the weak adhesion strength indicated by the mechanical properties of interface elements and high local porosity in the transition zone lead to the low tensile strength of the ITZ sample.
- (3) Since the surface roughness may affect the mechanical properties in multiple ways, the sole mechanical effect of roughness is also studied by homogenizing the microstructure of ITZ. It is found that the ITZ model with the rough surface

exhibits a higher uniaxial tensile strength when the heterogeneity of ITZ microstructure is suppressed.

- (4) For the fatigue properties, the effect of roughness on fatigue properties of ITZ models is not apparent if the stress level is considered. On the one hand, the irregularities of the rough surface aggregate leads to more stress concentrations, which may favor initiations of cracks. On the other hand, the higher bonding strength of rough aggregate allows it to sustain a higher stress, and therefore a higher degree of fatigue damage. When the applied stress magnitude is considered, the specimen with rough aggregate surface definitely exhibits superior fatigue resistance.

This work contributes to the multiscale modelling framework in the next chapter. The obtained interface properties can be used as inputs in the mesoscopic fatigue simulation of a mortar sample. In the next chapter, the fatigue damage evolution in the mortar sample and how the interfacial properties affect the overall fatigue performance of mortar are investigated.

**REFERENCES**

- [1] K.M.A. Sohel, K. Al-Jabri, M.H. Zhang, J.Y.R. Liew, Flexural fatigue behavior of ultra-lightweight cement composite and high strength lightweight aggregate concrete, *Constr. Build. Mater.* 173 (2018) 90–100.
- [2] X. Chen, J. Bu, X. Fan, J. Lu, L. Xu, Effect of loading frequency and stress level on low cycle fatigue behavior of plain concrete in direct tension, *Constr. Build. Mater.* 133 (2017) 367–375.
- [3] Y. Gan, C.R. Rodriguez, E. Schlangen, K. van Breugel, B. Šavija, Assessing strain rate sensitivity of cement paste at the micro-scale through micro-cantilever testing, *Cem. Concr. Compos.* 121 (2021).
- [4] H. Zhang, B. Šavija, E. Schlangen, Towards understanding stochastic fracture performance of cement paste at micro length scale based on numerical simulation, *Constr. Build. Mater.* 183 (2018) 189–201.
- [5] F. Gong, T. Ueda, Y. Wang, D. Zhang, Z. Wang, Mesoscale simulation of fatigue behavior of concrete materials damaged by freeze-thaw cycles, *Constr. Build. Mater.* 144 (2017) 702–716.
- [6] B. Zhang, Relationship between pore structure and mechanical properties of ordinary concrete under bending fatigue, *Cem. Concr. Res.* 28 (1998) 699–711.
- [7] Z. Fan, Y. Sun, Detecting and evaluation of fatigue damage in concrete with industrial computed tomography technology, *Constr. Build. Mater.* 223 (2019) 794–805.
- [8] K.L. Scrivener, A.K. Crumbie, P. Laugesen, The interfacial transition zone (ITZ) between cement paste and aggregate in concrete, *Interface Sci.* 12 (2004) 411–421.
- [9] M. Lukovic, E. Schlangen, G. Ye, B. Šavija, Impact of surface roughness on the debonding mechanism in concrete repairs, *Proc. 8th Int. Conf. Fract. Mech. Concr. Concr. Struct. Fram.* 2013. (2013) 611–621.
- [10] M.K. Lee, B.I.G. Barr, An overview of the fatigue behaviour of plain and fibre reinforced concrete, *Cem. Concr. Compos.* 26 (2004) 299–305.



# 7

## MESOSCOPIC MODELLING OF FATIGUE BEHAVIOUR OF MORTAR USING OUTPUT FROM THE MICROSCOPIC MODELLING

*In this chapter the uniaxial tensile fatigue behaviour of mortar at the mesoscale is predicted by using the developed fatigue lattice model. Digital mesostructures of mortar, considering the randomly distributed irregular aggregate particles and air voids, are first established. In total, four phases can be recognised in the mortar model: the cement paste, aggregates, ITZ and air voids. An uncoupled upscaling approach is employed to bridge two scales, i.e. the microscale and the mesoscale. Mechanical and fatigue properties of the ITZ and cement paste obtained from the microscopic modelling in Chapter 5 and 6 are used as inputs for the mesoscopic model. The influence of different ITZ properties on the fracture performance of mortar is investigated. Special attention is paid to the effect of ITZ properties on the fatigue damage evolution in the mortar.*



## 7.1 INTRODUCTION

Numerous efforts have been invested to develop multiscale models [1–7] which are capable of coupling mechanical properties at different length scales. The main goal of such models is to establish a relationship between macroscopically observable phenomena and their lower-scale origin and evolution. Once this relation is found, changes in structural features of the material can be considered at the respective observation scales and their effects on the macroscopic performance can be predicted by means of appropriate upscaling approaches. Moreover, multiscale models help to realize the performance-oriented optimization of the material microstructure by modifying the material chemistry and composition and evaluating the outcome.

For the multiscale model proposed in this chapter, the material structures at different scales are explicitly considered. Generally, the heterogeneous microstructure of cement paste can be obtained by either experimental techniques [8,9] or digital hydration programs [2,10–12]. In the microscopic model (presented in Chapter 5 and 6), microstructures of cement paste and the ITZ including microstructural features of basic components, e.g. hydration products and pores, are obtained using the XCT technique. Meanwhile, microscale tests on miniature samples are performed using the nanoindenter. The mechanical and fatigue properties of individual constituents in the cement paste and ITZ are determined by an inverse analysis. The experimental results are further used to validate the microscopic model. For simulating the mortar, four main phases, e.g., air voids, cement paste matrix, aggregates and ITZ, should be considered. The constitutive relations of the bulk paste matrix and ITZ will be preferably derived from the microscopic simulations [6]. It means that the outputs from the micromechanical modelling should be used as the input for the mesoscopic modelling.

In this chapter, virtual mortar specimens are first generated using the Anm model developed by Qian [2]. The size of the mortar specimen is set to  $50 \times 50 \text{ mm}^2$  with a mesh size of  $500 \text{ }\mu\text{m}$ . As the sizes of cement paste and ITZ virtual specimens are also  $500 \text{ }\mu\text{m}$  in the microscopic model, the length of  $500 \text{ }\mu\text{m}$  is used to bridge two scales. For the upscaling approach, an uncoupled parameter-passing scheme developed by Qian [2] is adopted to connect the two scales, i.e. micro- and meso-scale. It has been examined in [3,13] that this upscaling method is a valid tool to bridge different scales. The previously simulated uniaxial tensile static and cyclic stress-strain curves of ITZ and cement paste at this length scale are approximated with multi-linear curves and used as local inputs in the mesoscopic simulation. The simulated global *S-N* relations for the ITZ and cement paste in microscopic models are directly used as local fatigue properties in the mortar simulation. By explicitly considering the mesostructure of mortar, the mechanical and fatigue behaviour of mortar is simulated. Moreover, a parametric study focusing on the effects of stress level and ITZ properties is conducted. The simulation results are compared with experimental results from the literature. Emphasis is also placed on the fatigue damage evolution in mortar samples with different ITZ properties.

## 7.2 NUMERICAL APPROACH

### 7.2.1 2D MORTAR VIRTUAL SPECIMENS

It is well-known that the shape and size of aggregate particles have a significant influence on the mechanical performance of mortar or concrete [14,15]. For a quantitative prediction of the material behaviour, realistic aggregate shape and size should be used. In this work, the Anm material model developed by Qian [2] is used to generate the mesostructure of mortar. The Anm material model is programmed on the basis of the 3D mathematical analysis of particle shape as described in [16]. Aggregate particles with irregular shape are uniquely described by the spherical harmonics with a set of spherical harmonic coefficients. An example of an irregular particle is shown in Figure 7-1. Aggregate particles can be selected from a particle shape database. All the particles are separated into several sieve ranges according to the particle sizes indicated by the particle widths.

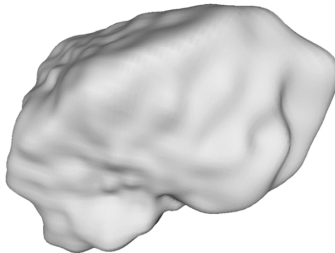


Figure 7-1 An irregular shape particle described by spherical harmonics from [2]

The simulated aggregate particles are then placed into a pre-defined 3D domain following a parking algorithm. A brief description of the parking algorithm is given here: An empty cubic container is first created to represent the specimen. All particles are placed one after another into this container, from the larger ones to smaller ones. For each parking step, the particle is placed at a random location and is checked against all the previously placed particles for overlap. If the overlap is detected, the particle will be relocated, rescaled or rotated depending on the number of attempts. More details about this parking algorithm are available in [2].

In this work, the volumetric fraction of sand is set to be 30.0% and the size of individual sand particle is randomly selected from 5 mm to 10 mm. Besides, air voids are packed separately in a similar way by assuming spherical voids. The air content is

3.5% and the diameter range of the voids is from 1 mm to 12 mm. It needs to be noted that the 30% volumetric fraction of sand is lower than the fraction commonly used in mortar samples. In consideration of the important role of sand in the mechanical performance of mortar [17], the effect of low sand content on the mechanical and fatigue properties of mortar will be discussed in Section 7.3. After packing sand particles and air voids, the geometrical structure of the mortar is obtained and digitalized into the digital specimens with a resolution of 500  $\mu\text{m}/\text{voxel}$ , resulting in a  $100 \times 100 \times 100$  voxels mesostructure ( $50 \times 50 \times 50 \text{ mm}^3$ ). The generated 3D digital mortar sample is shown in Figure 7-2. Afterwards, 2D slices are extracted and converted to the lattice model containing four element types: cement paste matrix, sand, ITZ and air void.

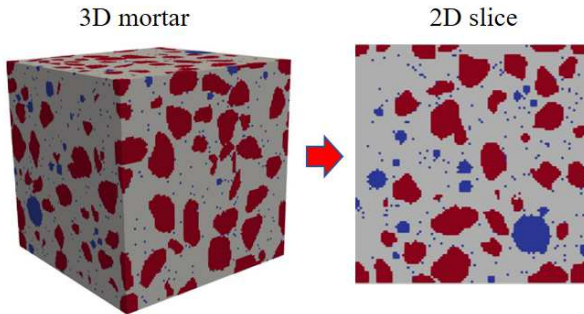


Figure 7-2 The 3D digital mortar sample ( $50 \times 50 \times 50 \text{ mm}^3$ ) and the extracted 2D slice (red represents sand, grey represents paste matrix and blue is pore)

### 7.2.2 CONSTITUTIVE LAW FOR MORTAR SIMULATION

The simulation results presented in Chapter 5 and 6, have shown that the local post-peak softening behaviours of cement paste and ITZ are significant and should be properly introduced in the mesoscopic model. Therefore, an uncoupled upscaling approach as proposed by Qian [2] is used to formulate the constitutive relations by approximating the original non-linear stress-strain curve with a multi-linear curve. Figure 7-3 schematically shows the generated multi-linear curves for both the cement paste and the ITZ. For each component, five points are selected from the stress-strain diagram to form a multi-linear curve. These points should be chosen in such a way that the local properties gradually decrease in terms of elastic modulus and tensile strength. In this work, five segments are taken for each phase and they are selected by choosing a random reduction percentage between 40% and 60% for the elastic modulus. The

selected points are listed in Table 7-1. With respect to cement paste elements, their constitutive relations are taken from Chapter 5, in which uniaxial tension simulations were conducted on the  $500 \times 500 \mu\text{m}^2$  cement paste specimens. The simulated stress-strain curve on the ITZ virtual specimen with the same size (Chapter 6) is also approximated using the multi-linear curve. In order to investigate the effect of ITZ properties on the global performance of mortar, two different surface roughness, i.e. ITZ\_F\_4 and ITZ\_R\_4, are used as inputs for the mesoscale modelling. The choice of the properties of ITZ\_F\_4 sample is such that it has the lowest strength in flat ITZ samples and can be considered as the lower bound. The ITZ\_R\_4 is the higher bound, which is the strongest of the rough ITZ samples. There is an apparent difference in their stress-strain curves, as is shown in Figure 7-3, and they can in principle be labelled as ‘weak’ and ‘strong’ ITZ, respectively. The sand in the model is assumed to experience no degradation under static and fatigue loading. Therefore, a linear elastic brittle constitutive law is used for the sand. Its elastic modulus is taken from the literature [18], i.e. 70 GPa. Its tensile strength is assumed as 1/1000 of the elastic modulus.

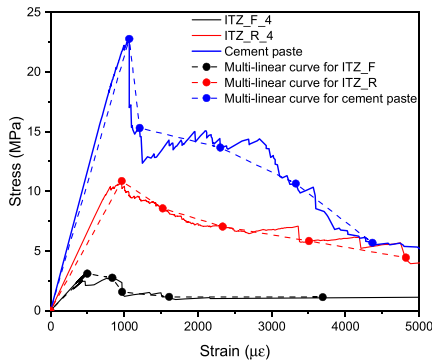


Figure 7-3 Approximations of the non-linear stress-strain responses of paste matrix and ITZ using multi-linear curves

For the fatigue simulation, the post-peak cyclic behaviour is also described by the chosen points, which are introduced in cyclic constitutive laws using Eq.(5-4) and Eq.(5-5). In addition, the simulated  $S-N$  relationships for cement paste and ITZ are also used as parameters that control the local fatigue damage evolution in mesoscopic modelling. For the cement paste element, the fatigue damage is negligible when the local stress is small. Therefore, the fatigue damage in a paste element is accumulated only when its stress level exceeds 10% of the remaining strength.

Similar to the static fracture simulation, two interfacial element types with different mechanical and fatigue properties are also implemented in fatigue simulations.

The mechanical and fatigue properties of components in the mortar simulation are summarised in Table 7-2. Note that the fatigue parameter  $a$  in Eq.(5-2) is a decisive factor in determining the damage evolution and a higher value of this parameter generally indicates a lower fatigue resistance. However, as mentioned earlier, the overall fatigue performance also depends on the ultimate stress that the material can sustain. The cement paste in the model has better fatigue resistance compared to the ITZ because of its higher tensile strength and higher value of  $a$ . Even though the difference between fatigue parameters of two interfacial elements is small, the ITZ with stronger mechanical properties exhibits a better fatigue performance. Note that the stress concentrations in a mortar or concrete composite always emerge near the ITZ, where high stress levels can be expected. In this case, the fatigue performance of ITZ mainly depends on its ultimate strength instead of the value of fatigue parameter.

Table 7-1 Step-wise constitutive relations of cement paste and ITZ up-scaled from the microscopic modelling in Chapter 5 and 6 (Interface 1: strong ITZ, Interface 2: weak ITZ)

Element type	Mechanical properties	Segment 1	Segment 2	Segment 3	Segment 4	Segment 5
Cement paste	$f_t$ (MPa)	22.76	15.30	13.66	10.64	5.68
	$E$ (GPa)	21.29	12.64	5.93	3.20	1.30
Interface 1 (ITZ_F_4)	$f_t$ (MPa)	10.86	8.57	7.04	5.83	4.44
	$E$ (GPa)	11.23	5.63	3.01	1.66	0.92
Interface 2 (ITZ_R_4)	$f_t$ (MPa)	3.10	2.75	1.57	1.15	1.13
	$E$ (GPa)	6.19	3.28	1.62	0.71	0.31

Table 7-2 Local fatigue properties of different phases in mortar (Interface 1: strong ITZ, Interface 2: weak ITZ)

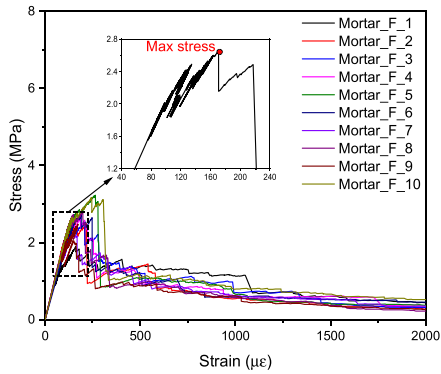
Element type	$f_t$ (MPa)	$E$ (GPa)	a	b	$\epsilon_{\max}$
Cement paste (w/c 0.4)	22.76	21.29	0.04	1.07	6500
Interface 1 (ITZ_F_4)	3.10	6.19	0.10	1.13	5000
Interface 2 (ITZ_R_4)	10.86	11.23	0.09	1.17	5000
Aggregate	70	70	-	-	-

## 7.3 RESULT AND DISCUSSION

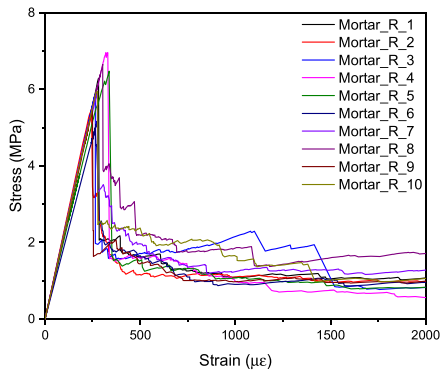
### 7.3.1 UNIAXIAL TENSILE FRACTURE SIMULATION

In total, ten virtual mortar samples are modelled. To determine the mechanical properties of these mortar samples, static uniaxial tension tests are performed by applying a unit nodal load at one end while the nodes at the other end are fixed. The simulated stress-strain curves are given in Figure 7-4. For the weak ITZ sample, there are many nonlinearities observed before the peak stress is reached due to initial fracture of interfacial elements [1]. For the strong ITZ mortar samples, the stress-strain curves are almost linear up to the peak stress. Based on the simulation results, the average strength and elastic modulus for mortar samples with the weak ITZ samples are  $2.30 \pm 0.12$  MPa and  $19.76 \pm 0.92$  GPa, respectively, while the average results for the strong ITZ samples are  $6.02 \pm 0.57$  MPa and  $21.84 \pm 1.16$  GPa, respectively. The overall strength is clearly higher when the ITZ is stronger. The simulated mechanical properties are within a reasonable range compared to the experimental results reported in the work of Zhang et al. [3], where mortars with a similar volume fraction of aggregate but lower w/c ratio (0.3) were tested. The obtained strength and elastic modulus in their study are 5.74 MPa and 26.36 GPa, respectively.

The simulated fracture patterns for different ITZ properties are given in Figure 7-5. When the ITZ is weak, the major crack mostly follows the edges of aggregates. For the strong ITZ, the crack will also penetrate into the paste matrix, given the same mesostructure of mortar. It is also found that the total number of cracked elements is higher in weak ITZ samples. Moreover, the mortar with a strong ITZ seems to be more brittle than the weak ITZ samples at the post-peak stage. However, it should be mentioned again that the realistic 3D connectivity and tortuosity of the pore structure cannot be considered in 2D simulations. This may result in lower fracture energy and possibly higher strength. Therefore, it is important and necessary to perform 3D simulation in future studies. In addition, the packing density of sand used in current model is relatively low compared to the standard mortar mix. When the sand content increases, the content of ITZ and the possibility of ITZ being connected or overlapped will also increase. In this case, the occurrence of nonlinearity at the pre-peak stage would be sooner and the amount of nonlinearity would also increase. Moreover, a lower strength of mortar and a more tortuous of crack pattern would be expected. However, during the mixing of paste with sands, a portion of water may be adsorbed by sands [19,20], resulting in a decrease of the effective w/c ratio [17]. As a result, the strength of both paste and ITZ will increase due to the decrease of w/c ratio. This strengthening effect mainly depends on the content and water absorption capacity of the sand. To account for this strengthening effect in the simulation of mortar, the possible microstructural changes due to the decrease of effective w/c ratio may need to be considered in the microscopic models of cement paste and ITZ.



(a) 'Weak' ITZ



(b) 'Strong' ITZ

Figure 7-4 The simulated stress-strain curves of mortar for (a) the 'weak' ITZ and (b) 'strong' ITZ

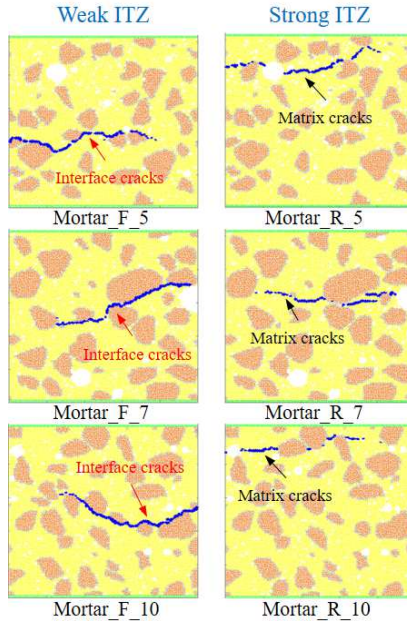


Figure 7-5 The simulated fracture patterns of mortar samples with different ITZ properties (yellow represents the paste matrix, grey represents the ITZ and the orange represents the aggregate, and the crack is blue)

### 7.3.2 UNIAXIAL FATIGUE SIMULATION

For fatigue simulations, the applied stress levels are 60%, 70% and 80% of the corresponding static strength. Two types of ITZ elements are used in fatigue simulations of mortar samples. The simulated  $S-N$  curves are shown in Figure 7-6. It appears that the stronger ITZ also yields a higher fatigue resistance, indicated by the longer fatigue life at a given stress level. Nevertheless, the simulated fatigue life of mortar is significantly shorter compared to that of cement paste at the same stress level (Chapter 3) due to the presence of the ITZ. The ITZ may provide more locations for the initiation and propagation of cracks. For the validation of the mortar simulation, the experimental data regarding fatigue of mortar at similar length scale are used. However, there is very limited experimental investigation on the tensile fatigue of mortar in literature. As a remedy, the comparison with available experimental results focusing on the flexural fatigue of mortar or concrete is conducted to evaluate the numerical results. The collected  $S-N$  data from literature [21–24] are presented in Figure 7-6. The



simulated fatigue life of numerical mortar based on inputs from micromechanical models lies within a reasonable range compared to the experimental results. This supports the reasonableness of the multiscale modelling procedure used in this work and the validity of fatigue parameters employed in this model. It has to be noted that even though the simulation results are close to the results reported in literature, it would be very beneficial to conduct fatigue tests on mortar samples with the identical size and material composition used in the simulation. The experimental results of such fatigue tests could be used to further validate the mesoscopic model. In addition, the prediction accuracy of the mesoscopic model can also be improved by considering more realistic material structures and conducting more calibration procedures based on different microscopic experimental results.

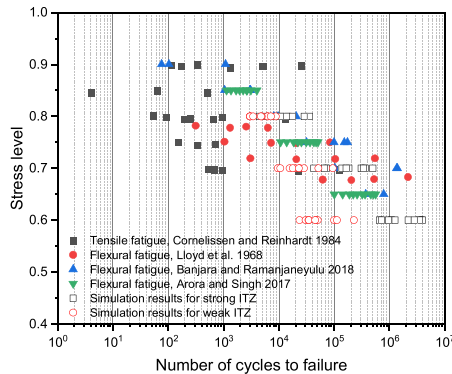


Figure 7-6 The comparison of experimental and numerical S-N results

### 7.3.3 FATIGUE DAMAGE EVOLUTION

Generally, several damage characterization indicators, e.g. the secant stiffness and residual strain of a sample, are used in experimental investigations to indirectly evaluate the fatigue damage evolution. One advantage of the proposed modelling scheme is that the whole process of damage evolution can be visualized by mapping the variation of the damage degree (i.e. index  $D$ ) in each element. This allows to directly analyse the fatigue damage development inside the mortar sample. Note that the fatigue damage mainly depends on the local stress field and the element type (interface or bulk paste element). Meanwhile, the stress field will also be updated for each cycle due to the degradation of stiffness of individual element. It is possible that a severely damaged element may suffer less damage in the next cycle owing to the stress redistribution. This would affect the fatigue cracking path and the final fatigue life. Therefore, the fatigue

fracture process is more complicated compared to the static fracture as different degrees of degradation are accumulated simultaneously in the sample.

Figure 7-7 shows the fatigue damage contour map at different number of cycles for a mortar sample at the stress level of 60%. The results using two ITZ element types are presented. For the mortar sample with the weak ITZ in Figure 7-7(a), the fatigue damage at 10% of fatigue life  $N_f$  is mainly accumulated in the ITZ, and some minor damage is also observed in the paste matrix near air voids. With the increase of loading cycles, fatigue damage in ITZ elements is generated much faster than in the paste matrix. Some ITZ elements have already broken at around half of the fatigue life (their damage indexes have reached to 1). Before the end of the simulation, the damage development in the ITZ is continued and multiple fatigue cracks surrounding the aggregate particles gradually form. However, only mild damages have been detected in most cement paste elements, even when the fatigue failure criterion is fulfilled. For the case of mortar with the strong ITZ, most cement paste elements have already been damaged when the simulation is at the initial stage (25% of  $N_f$ ), which is different from the sample with the weak ITZ. It indicates that the paste matrix may suffer more damage due to the stronger ITZ. However, when the major crack occurs, the damage in cement paste barely increases further with increasing number of loading cycles. Another significant difference between the results of mortars with a weak and strong ITZ is the distribution and number of fatigue cracks. The mortar sample with the weak ITZ tends to generate more fatigue cracks in the ITZ, while much less interfacial cracks are detected in the sample with a strong ITZ. Moreover, the main reason for fatigue failure of the sample with a weak ITZ is the massive breakdown of ITZ elements, whereas the critical crack formed in strong ITZ samples is due to the coalescence of cracks in both the ITZ and the paste matrix.

The simulated fatigue damage evolution is qualitatively similar to the experimental observations reported by Fan and Sun [25], in which the XCT tests were performed on different stages of fatigue loading. Their XCT results show that the number, length and width of fatigue cracks in concrete samples gradually increase with the increasing number of cycles. Many microcracks were formed along the edge of aggregates. Multiple cracks were also detected and these cracks were connected to each other along aggregates' edge and the weak areas of the cement mortar. Moreover, they also found that after the initial stage of fatigue loading, the pores in concrete did not develop into new cracks. Instead, they provided a channel for the expansion of existing cracks. This phenomenon is similar to the simulation results presented here.

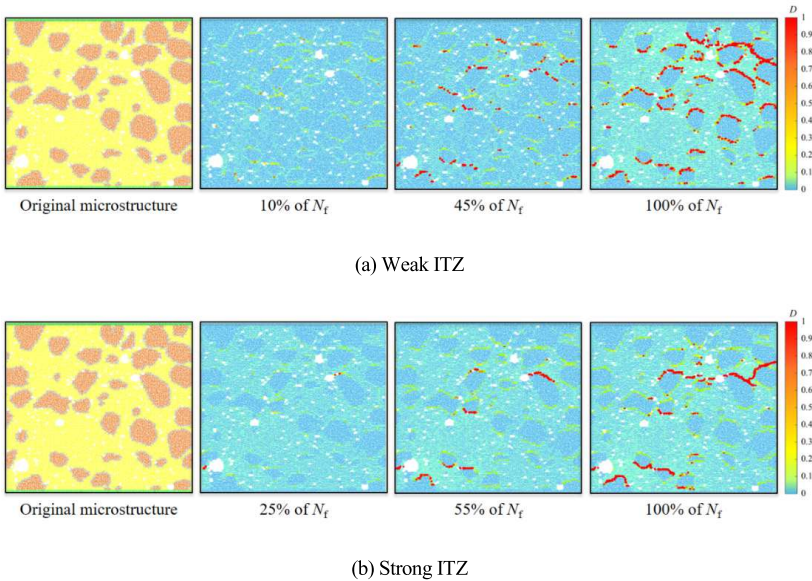


Figure 7-7 The contour maps of fatigue damage at different stages of cyclic loading at the stress level of 60% for virtual mortar samples with (a) the weak ITZ (Mortar\_F\_2,  $N_f=30486$ ) and (b) the strong ITZ (Mortar\_R\_2,  $N_f=660866$ )

To gain more insight into the fatigue damage evolution, the contour maps of fatigue damage in the final stage of the fatigue life under different stress levels (60% and 80%) are analyzed. The results of two virtual mortar samples, i.e. Mortar\_R\_4 and Mortar\_F\_7, are presented in Figure 7-8. When the strong ITZ is used in the mortar simulation, the final distributions of cracks are slightly different for these two stress levels, as is shown in Figure 7-8(a). Nevertheless, fatigue damage generated in cement paste under the two stress levels, in terms of number of damaged elements and damage degree ( $D$ ), are very similar. For instance, around 52.0% and 56.9% of the cement paste elements have been damaged to a certain degree (i.e.,  $0 < D \leq 0.2$ ) for the two stress levels, respectively. In the case of Mortar\_F\_7 with the weak ITZ, the major difference is the accumulation degree of fatigue damage in the cement paste. When the applied stress level is 80%, there is almost no damage in the cement paste. The mortar fails immediately after the formation of the critical crack in the ITZ. This phenomenon is similar to the crack localization in static fracture (see Figure 7-5). However, at lower stress levels some damage accumulates in the cement paste and the fatigue life increase considerably. The XCT results reported by Fan and Sun [25] also indicate that the evolution of the main fatigue crack was largely related with the stress level. When the stress level was lower, the fatigue damage evolution in the concrete was more

significant. The main fatigue crack's width was also found to be larger at a lower stress level. Similar findings were also reported in studies performed on Chen and Cheng [26], in which more fatigue cracks in concrete beams were observed at lower stress level.

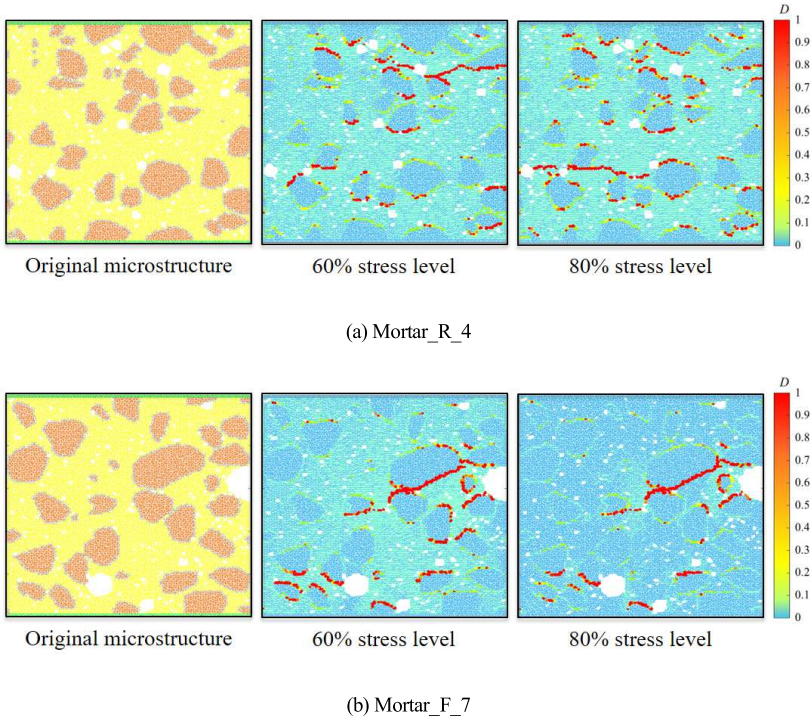


Figure 7-8 The contour maps of fatigue damage at different stress levels for virtual mortar samples (a) Mortar\_R\_4,  $N_f = 661074$  (60%), 10670 (80%) and (b) Mortar\_F\_7,  $N_f = 34543$  (60%), 10918 (80%)

In general, the fatigue fracture process may also be affected by the content of sand in a similar manner to the static fracture. When the volumetric fraction of sand is increased, the fatigue damage evolution would be accelerated due to the increasing volume of ITZ. The period for the initiation and propagation of crack would be reduced and, consequently, the final fatigue life of mortar would also be decreased. Based on the simulation results in Figure 7-8, it can be expected that the fatigue resistance of the remaining paste matrix becomes increasingly important to the fatigue life with the increasing content of sand content, especially when the ITZ is still isolated and the stress

level is low. Once the ITZ is connected and overlapped, the fatigue life of mortar would significantly decrease, especially under the high stress level. In addition, the fatigue failure of mortar may be more brittle with the increasing content of sand as there would be considerable damage accumulated in the mortar before the occurrence of unstable crack.

The ratio between the strength of strong ITZ and weak ITZ is around 2.44 in current simulations. When the applied stress level is the same and the difference in local fatigue properties of the ITZ is small, the 244% increase of ITZ strength leads to a boost of the fatigue life by approximately one to two orders of magnitude. It can be concluded that the mechanical properties of the ITZ significantly affect the fatigue properties of mortar by altering the damage evolution process, and eventually the final fatigue life. Therefore, the strength of the ITZ plays an important role in fatigue behaviour of cementitious composites.

## 7.4 CONCLUSIONS

In this chapter, the uniaxial tensile fatigue behaviour of mortar at the mesoscale is simulated and predicted by using the fatigue lattice model developed in Chapter 5. Digital mesostructures of mortar are established using the Anm model. Mechanical and fatigue properties of the ITZ and cement paste obtained from the microscopic modelling in Chapter 5 and 6 are used as inputs for the mesoscopic model. The influence of different ITZ properties and stress levels on the fatigue behaviour of mortar is investigated. It is found that the uncoupled upscaling approach using the step-wise constitutive laws is a suitable tool to bridge two scales in a multiscale modelling scheme. The simulated mechanical properties and *S-N* curves lie within a reasonable range compared to experimental results found in literature. Simulation results indicate that the inclusion of an ITZ is the main reason for reduced fatigue resistance of mortar samples compared to cement paste. Moreover, the mechanical properties of the ITZ play an important role in the fracture behaviour of mortar samples subjected to both static and fatigue loading. Essentially, a strong ITZ may force the development of cracks and damage in the cement paste, and thus affect the fracture properties and the fatigue life. Similarly, different stress levels will also affect the fatigue damage evolution depending on the properties of the ITZ. Therefore, the increase of the ITZ strength can significantly improve the fatigue properties of mortar by means of altering the damage evolution process, and eventually the final fatigue life.

The simulation model presented in this chapter is a first attempt to develop a lattice fatigue model at the micro- and mesoscale, and is considered an essential starting point for predicting the fatigue performance of concrete structures. Although the current 2D model offers the opportunity to simulate the fatigue behaviour of cementitious material in a multiscale framework, 3D simulation is still required to consider more realistic material structures. Nevertheless, the current model has successfully demonstrated the effect of heterogeneities at different scales on the fatigue

performance of cementitious material in a very efficient way and provided some valuable insights into the fatigue damage evolution and fatigue fracture phenomena. With the help of the developed model, it is possible to predict the fatigue life of the cement paste or mortar for a given material structure. Moreover, the output of numerical simulations at the mesoscale could be further used to predict the macroscopic fatigue performance of concrete structures.

## REFERENCES

- [1] J.G.M. Van Mier, Concrete fracture: a multiscale approach, CRC press, 2012.
- [2] Z. Qian, Multiscale modeling of fracture processes in cementitious materials, Delft University of Technology, PhD Thesis, 2012.
- [3] H. Zhang, Y. Xu, Y. Gan, E. Schlangen, B. Šavija, Experimentally validated meso-scale fracture modelling of mortar using output from micromechanical models, *Cem. Concr. Compos.* 110 (2020).
- [4] Z. Ding, D.C. Feng, X. Ren, J. Wang, Physically based constitutive modeling of concrete fatigue and practical numerical method for cyclic loading simulation, *Eng. Fail. Anal.* 101 (2019) 230–242.
- [5] B. Šavija, H. Zhang, E. Schlangen, Micromechanical testing and modelling of blast furnace slag cement pastes, *Constr. Build. Mater.* 239 (2020).
- [6] H. Zhang, Y. Xu, Y. Gan, Z. Chang, E. Schlangen, B. Šavija, Microstructure informed micromechanical modelling of hydrated cement paste: Techniques and challenges, *Constr. Build. Mater.* 251 (2020) 118983.
- [7] J.L. Le, J. Manning, J.F. Labuz, Scaling of fatigue crack growth in rock, *Int. J. Rock Mech. Min. Sci.* 72 (2014) 71–79.
- [8] H. Zhang, B. Šavija, S.C. Figueiredo, M. Lukovic, E. Schlangen, Microscale testing and modelling of cement paste as basis for multi-scale modelling, *Materials (Basel)*. 9 (2016).
- [9] Y. Gan, H. Zhang, M. Liang, E. Schlangen, K. van Breugel, B. Šavija, A numerical study of fatigue of hardened cement paste at the microscale, *Int. J. Fatigue*. 151 (2021) 106401.
- [10] K. Van Breugel, Simulation of hydration and formation of structure in hardening cement-based materials., (1993).
- [11] S. Bishnoi, K.L. Scrivener,  $\mu$ ic: A new platform for modelling the hydration of cements, *Cem. Concr. Res.* 39 (2009) 266–274.
- [12] D.P. Bentz, Modeling the influence of limestone filler on cement hydration using CEMHYD3D, *Cem. Concr. Compos.* 28 (2006) 124–129.
- [13] H. Zhang, B. Šavija, S.C. Figueiredo, E. Schlangen, Experimentally validated multi-scale modelling scheme of deformation and fracture of cement paste, *Cem. Concr. Res.* 102 (2017) 175–186.
- [14] W. Trawiński, J. Tejchman, J. Bobiński, A three-dimensional meso-scale modelling of concrete fracture, based on cohesive elements and X-ray  $\mu$ CT images, *Eng. Fract. Mech.* 189 (2018) 27–50.
- [15] Y. Zhou, H. Jin, B. Wang, Modeling and mechanical influence of meso-scale concrete considering actual aggregate shapes, *Constr. Build. Mater.* 228 (2019) 116785.
- [16] E.J. Garboczi, Three-dimensional mathematical analysis of particle shape using X-ray tomography and spherical harmonics: Application to aggregates used in concrete, *Cem. Concr. Res.* 32 (2002) 1621–1638.
- [17] Y. Gao, G. De Schutter, G. Ye, Z. Tan, K. Wu, The ITZ microstructure, thickness and porosity in blended cementitious composite: Effects of curing age, water to binder ratio and aggregate content, *Compos. Part B Eng.* 60 (2014) 1–13.
- [18] H. Zhang, Y. Gan, Y. Xu, S. Zhang, E. Schlangen, B. Šavija, Experimentally informed fracture modelling of interfacial transition zone at micro-scale, *Cem. Concr. Compos.* 104 (2019).
- [19] W. Piasta, B. Zarzycki, The effect of cement paste volume and  $w/c$  ratio on shrinkage strain, water absorption and compressive strength of high performance concrete, *Constr. Build. Mater.* 140 (2017) 395–402.

- [20] A. Yacoub, A. Djerbi, T. Fen-Chong, Water absorption in recycled sand: New experimental methods to estimate the water saturation degree and kinetic filling during mortar mixing, *Constr. Build. Mater.* 158 (2018) 464–471.
- [21] H.A.W. Cornelissen, H.W. Reinhardt, Uniaxial tensile fatigue failure of concrete under constant-amplitude and programme loading, *Mag. Concr. Res.* 36 (1984) 216–226.
- [22] J. Lloyd, J. Lott, C. Kesler, *Fatigue of Concrete*, (1968) 25.
- [23] N.K. Banjara, K. Ramanjaneyulu, Experimental investigations and numerical simulations on the flexural fatigue behavior of plain and fiber-reinforced concrete, *J. Mater. Civ. Eng.* 30 (2018) 1–15.
- [24] S. Arora, S.P. Singh, Fatigue strength and failure probability of concrete made with RCA, *Mag. Concr. Res.* 69 (2017) 55–67.
- [25] Z. Fan, Y. Sun, Detecting and evaluation of fatigue damage in concrete with industrial computed tomography technology, *Constr. Build. Mater.* 223 (2019) 794–805.
- [26] C. Chen, L. Cheng, Fatigue behavior and prediction of NSM CFRP-strengthened reinforced concrete beams, *J. Compos. Constr.* 20 (2016) 4016033.





# 8

## RETROSPECTION, CONCLUSIONS AND PROSPECTS

*In this chapter a brief summary of the work presented in this PhD thesis is given. Additionally, general conclusions and findings of this research are presented. In the end, recommendations for further work are given.*

## 8.1 RETROSPECTION

Ageing is an inherent feature of all natural and man-made materials and products, including concrete. As one of the typical ageing phenomena, fatigue of concrete has received considerable research attention, motivated by its practical importance. Many concrete structures, such as off-shore structures, tall buildings, roads and bridges, are inevitably subjected to fatigue loading and may suffer from serious fatigue-induced safety and durability issues. However, the phenomenon of concrete fatigue is very complex as it involves multiple spatial scales owing to the multiscale heterogeneous nature of concrete, as explained in Chapter 1. To better understand the fatigue behaviour of concrete, investigations on fatigue behaviours of concrete at different scales are necessary. For this reason, the first goal of this thesis was to investigate the microscopic fatigue behaviour of two basic components of concrete, i.e., cement paste and paste-aggregate interfacial transition zone (ITZ).

To achieve this goal, novel experimental techniques for characterisation of mechanical and fatigue properties of cementitious materials at the microscale were developed. These techniques include preparation of miniature samples and microscale fatigue testing. Firstly, a precision micro-dicing machine was used to fabricate micrometre sized samples. With the help of a nanoindentation measurement device, micro-bending tests were performed to study the flexural fatigue behaviour of cement paste and the ITZ. Other techniques, including environmental scanning electron microscopy and X-ray computed tomography, have been used to investigate the fatigue fracture surface and damage evolution. The fatigue life, characteristics of fatigue fracture, stiffness degradation and residual deformation evolution of cementitious materials at the microscale were investigated. These experimental results can be further used as the benchmark for the development of the multiscale model.

Another major goal of this thesis was to predict the fatigue properties of cementitious materials, for example in view of the fatigue life and fatigue damage evolution process. To this aim, the 2D lattice fracture model was extended to consider the fatigue behaviour of cementitious material. Microstructures of cement pastes and ITZ obtained from XCT tests were used as input for the lattice model. Different mechanical and fatigue properties were assigned to different phases of the cement paste and the interfacial transition zone. A cyclic constitutive law was proposed for considering the fatigue damage evolution, in which the pre-peak fatigue damage evolution is determined based on the combined  $S-N$  approach and Miner's law, while the post-peak behaviour is controlled using a step-wise softening law. Fatigue experiments performed at the same length scale were used to calibrate and validate the model. The global fatigue response of different microstructures of cement paste and ITZ can be evaluated by using the developed model. Afterwards, a multiscale modelling approach was proposed to link the fatigue behaviour between the micro- and mesoscales. Digital mesostructures of mortar were established using the Anm model for particle packing. The simulated properties of cement paste and ITZ from the microscale modelling were used as input properties for mesoscale modelling of mortar.

The influence of different ITZ properties and stress levels on the fatigue behaviour of mortar was investigated as well. The major source of scatter for fatigue results is the heterogeneity of the microstructure, which can clearly be demonstrated by simulations. Reasonably good agreements have been observed between the simulation results and experimental data from literature.

## 8.2 CONCLUSIONS

The fatigue fracture, fatigue damage and residual deformation evolution of cementitious material at the microscale were investigated in this study. Besides, a lattice model for simulating the fatigue response of cementitious material was developed. Finally, a multiscale modelling scheme connecting the micro and mesoscale was used to connect the fatigue properties at the micro and mesoscale. The results of this thesis help to improve the understanding of fatigue behaviour of cementitious materials and offer a reference to engineers and researchers for predicting the ageing process, including the fatigue life and fatigue damage evolution, in concrete structures subjected to the cyclic loading. General conclusions of this research are given below:

*Microscale testing techniques offer an opportunity to investigate the microscopic mechanical and fatigue properties of cementitious materials.* The micromechanical properties including the flexural strength and elastic modulus, as well as the fatigue properties including the relationship between the fatigue life and stress level, the stiffness degradation and residual deformation evolution, can be obtained using the developed microscale testing approach. Therefore, the effect of material composition on the microscopic mechanical and fatigue properties of cementitious material can be directly examined via these techniques.

*There is a strong size dependence of fracture behaviour of cementitious materials under cyclic loading.* For the same stress level, the fatigue life of cement paste at the microscale (around several hundreds of micrometre) is almost two orders of magnitude longer than that of macroscopic centimetre-sized specimen reported in literature. If the stress magnitude is compared, the fatigue resistance of microscopic specimen is significantly higher than that of macroscopic samples owing to the size effect of static fracture in cementitious materials. Moreover, the microscopic fatigue damage evolution in both the cement paste and the ITZ is very slow and limited, even under high stress levels, which is different from the macroscopic fatigue damage evolution. The fatigue damage in microscopic samples is assumed to accumulate in the form of nanoscale crack propagation. Hence, the fatigue damage is affected by the nanostructure of cementitious material. The nanoscale cracks would gradually evolve into higher scale cracks and eventually lead to fatigue failure. The knowledge regarding the size-dependent fatigue properties of cementitious materials is useful particularly in practical design of fatigue life of large scale concrete structures based on testing results of laboratory sized specimens.

*The microscopic fracture mechanisms of cementitious materials are different for the static and cyclic loading.* When compared to the fracture surface occurring under static loading, a higher density of nanoscale cracks can be detected in fatigue fractured samples. Most of these cracks are a result of fractured C-S-H phases, which are generally located at the stress concentrations. It is suggested that several microscopic processes, e.g. stress redistribution and crack branching, occur during fatigue loading. As a result, multiple nanocracks propagate simultaneously inside the C-S-H gel particles in a diffuse manner and coalesce into a major crack before failure. This is also revealed by the simulation results.

*Two major mechanisms for residual deformation accumulation in cementitious materials are found at the microscale.* In general, three distinct stages of the development of residual deformation can be identified at the microscale, which is similar to most macroscopic observations on concrete fatigue in literature. However, due to the slow decrease of stiffness, it is suggested that the residual deformation of cement paste at the microscale is not caused only by the fatigue cracking growth. Based on the assumption of linear viscoelasticity, the viscoelastic deformation under cyclic loading seems to account for most of the measured residual deformation, especially in the initial stage of the fatigue test. At later stage, the residual deformation could be explained by the coupled effect of fatigue crack growth and viscoelastic deformation. The understanding of the origin of residual deformation is extremely important for predicting the long-term fatigue compliance of concrete bridges subjected to traffic loadings.

*The lattice fracture model is a promising tool for modelling the static and fatigue fracture behaviour of cementitious material at different scales.* The original lattice fracture model was extended to consider the fracture behaviour under cyclic loading by introducing a cyclic constitutive law. The material structure can be easily implemented in the lattice model. After the calibration and validation of the model using the experimental results, a unique set of input parameters is determined and used for two different boundary conditions, i.e. flexural and uniaxial tensile tests. The effects of w/c ratio, stress level and roughness of aggregate on the simulated fatigue life and fatigue damage evolution were investigated. In general, a lower w/c ratio leads to a higher fatigue resistance. The developed model is able to investigate the effect of microstructure heterogeneities on fatigue damage evolution in a very efficient way and can establish a quantitative relationship between the material structure and the global fatigue performance. The stress level and properties of ITZ significantly affect the fatigue damage evolution process, which eventually influence the final fatigue life.

*The uncoupled upscaling approach is useful for bridging two scales in the multiscale modelling scheme.* Via this approach, the global fatigue fracture behaviour (i.e. stress-strain response and *S-N* relation) simulated at smaller scale can be used as input for the fatigue fracture modelling at the larger scale. It is worth noting that the local constitutive relation of mortars at the mesoscale are directly derived from the microscopic models, without using any further parameter-fitting process at the higher scale. The model can predict satisfactory crack patterns, mechanical and fatigue

properties under fatigue loading. Hence, the model has fully predictive capabilities at the mesoscale and offers an opportunity to investigate in more detail the influence of material structures at different scales on the macroscopic fatigue performance. On the other hand, the multiscale model would be helpful for material designers in guiding performance-oriented optimization of the macroscopic fatigue properties of concrete structures, such as bridges, marine structures and road pavements.

### 8.3 PROSPECTS

From this study, several aspects of experimental testing and numerical simulations are recommended for further research:

The current study focuses on constant-amplitude fatigue loading, but actual concrete structures experience stress cycles varying in magnitude, number and sequence. Furthermore, innovative materials, such as fibre-reinforced cementitious materials and alkali activated concretes, are increasingly used and their fatigue behaviour may be different and need to be understood. Microscopic experimental investigations for other loading schemes and material compositions are needed.

The fatigue fracture mechanisms at the nanoscale remain untouched in this thesis. To better understand the origin of fatigue and establish a physics-based law for the fatigue crack propagation, more advanced techniques are needed to investigate the nanoscale fatigue fracture behaviour of cementitious materials.

To obtain more realistic simulation results, it is necessary to extend the current 2D lattice fatigue model to a 3D lattice fatigue model. The effects of 3D distribution of aggregate, connectivity of pore structures and crack branching behaviour on the global fatigue performance and fatigue damage evolution need further investigations.

Since the fatigue properties of cementitious materials at different scales exhibit significant scatter, future studies on multiscale modelling of fatigue behaviour should be conducted in a statistical manner. Moreover, to further improve the quantitative prediction accuracy of the multiscale modelling scheme developed in this study, experimental results for the fatigue of mortar or concrete samples at higher scales are needed.

Fatigue induced damage may be very detrimental for marine concrete structures that suffer from chloride ingress, such as foundations of offshore wind farms. Therefore, investigations on fatigue damage evolution coupled with chloride ingress or other cracking-related durability issues could be of great practical interest. Meanwhile, coupling the lattice fatigue model with a lattice transport model on multiple length scales could help to study the influence of cracks at different length scales on transport properties.



## SUMMARY

Ageing is an inherent feature of cementitious materials. Ageing of material leads to gradual loss of the function of a concrete structure with increasing likelihood of failure. As one of the typical ageing phenomena, fatigue of concrete, has recently received considerable research attention. The phenomenon of concrete fatigue is complicated as it inherently involves multiple spatial scales owing to the multiscale heterogeneous nature of concrete. Over the past century, tremendous efforts have been devoted to concrete fatigue. However, many important scientific problems still remain unsolved. These problems include at least: how does the multiscale heterogeneous material structure of concrete affect the fatigue behaviour; how does fatigue damage evolve inside the concrete; how to properly simulate and predict the fatigue behaviour. The main objective of this thesis is to improve the knowledge of fatigue behaviour of cementitious materials at the microscale and to develop a multiscale modelling scheme from micro- to meso-scale to estimate the fatigue properties.

Firstly, experimental techniques for characterization of mechanical and fatigue properties of cementitious materials at the microscale are developed. These techniques include the preparation and testing of micrometre sized sample. For sample preparation, a precision micro-dicing machine is used. With the help of a nanoindentation measurement device, micro-bending tests are performed to study the flexural fatigue behaviour of two major components in the mortar, i.e. the cement paste and the interfacial transition zone (ITZ). The fatigue fracture surface and damage evolution are assessed using an Environmental Scanning Electron Microscope (ESEM) and X-ray computed tomography (XCT). The mechanical properties, including the strength and elastic modulus, as well as the fatigue properties including the relationship between fatigue life and stress level, the stiffness degradation and residual deformation evolution, can be obtained using the developed microscale testing approach.

Secondly, a numerical model using a 2D lattice network is developed to simulate the fatigue behaviour of cementitious material at the microscale. Images of 2D microstructures of cement pastes and ITZ obtained from XCT tests are used as inputs and mapped to the lattice model. Different local mechanical and fatigue properties are assigned to different phases of the cement paste and interfacial transition zone. A constitutive law for cyclic loading is proposed to consider the fatigue damage evolution. Experimental results obtained at the microscale are used to calibrate and validate the model. The developed model is able to investigate the effect of microstructure heterogeneities on fatigue damage evolution in a very efficient way and can establish a quantitative relationship between the material structure and the global fatigue performance. Moreover, it can also provide valuable insight into the fatigue damage evolution and fatigue fracture phenomena under different stress levels.



Finally, a parameter-passing scheme is adopted for upscaling of the mechanical and fatigue properties. Via this approach, the global fatigue fracture behaviour (i.e. stress-strain response and  $S-N$  relation) simulated at smaller scale can be used as input for the fatigue fracture modelling at the larger scale. The model can satisfactorily predict crack patterns, mechanical and fatigue properties under fatigue loading. The model has fully predictive capabilities at the mesoscale. Hence, the model offers an opportunity to investigate in more detail the influence of material structures at different scales on the macroscopic fatigue performance.

## SAMENVATTING

Veroudering is een inherente karakteristiek van cementgebonden materialen. De veroudering van het materiaal leidt tot geleidelijk verlies van functionaliteit van betonconstructies met een toenemende kans op falen. Een typisch verouderingsverschijnsel, dat de laatste tijd veel aandacht heeft gekregen van onderzoekers, is vermoeiing van beton. Vermoeiing van beton is een gecompliceerd fenomeen, omdat vanwege het heterogene karakter van beton vermoeiings-mechanismen op meerdere schaalniveaus een rol spelen. In de afgelopen eeuw is veel onderzoek gedaan naar vermoeiing van beton. Veel belangrijke wetenschappelijke vragen zijn echter nog niet opgelost. Deze vragen betreffen in ieder geval: hoe beïnvloedt de heterogene materiaalstructuur van beton het vermoeiingsgedrag, hoe evolueert vermoeiings-schade binnenin het beton en hoe kan het vermoeiingsgedrag goed worden gesimuleerd en voorspeld. Het hoofddoel van dit proefschrift is het vergaren en verdiepen van kennis over het vermoeiingsgedrag van cementgebonden materialen op microschaal en het ontwikkelen van een (multischaal) numeriek model om het vermoeiingsgedrag te kunnen voorspellen.

Eerst worden experimentele technieken ontwikkeld voor het karakteriseren van mechanische en vermoeiingseigenschappen van cementgebonden materialen op microschaal. Dit omvat de voorbereiding en het testen van monsters op micrometerschaal. Voor het vervaardigen van proefstukken wordt een *precision micro-dicing machine* gebruikt. Met behulp van een nanoindenter worden microbuigtesten uitgevoerd om het vermoeiingsgedrag onder buiging te bestuderen van twee belangrijke componenten van mortel, namelijk de (bulk)cementsteen en de grenslaag tussen cementsteen en toeslagkorrel (zgn. interface zone, ITZ). Het breukoppervlak bij vermoeiingsbreuk en het schadeverloop worden beoordeeld met behulp van een Environmental Scanning Elektronenmicroscop (ESEM) en X-ray computertomografie (XCT). De mechanische eigenschappen, waaronder de sterkte en elasticiteitsmodulus, evenals de vermoeiingseigenschappen, waaronder de relatie tussen de vermoeiingslevensduur en het spanningsniveau, de stijfheidsafname en de resterende vervorming, kunnen worden verkregen met behulp van de ontwikkelde testmethode op microschaal.

Ten tweede wordt een numeriek model ontwikkeld met behulp van een 2D-roosternetwerk om het vermoeiingsgedrag van cementgebonden materiaal op microschaal te simuleren. Beelden van 2D-microstructuren van cementsteen en grenslagen (ITZ) verkregen uit XCT-tests worden gebruikt als invoer voor het roostermodel. Verschillende lokale mechanische en vermoeiingseigenschappen worden toegekend aan verschillende componenten van de cementsteen en de grenslaag. Er wordt een constitutieve wet voor cyclische belasting voorgesteld die rekening houdt met de ontwikkeling van vermoeiingsschade. Experimentele resultaten verkregen op micro-

schaal worden gebruikt om het rekenmodel te kalibreren en te valideren. Het ontwikkelde model kan het effect van heterogeniteit van microstructuren op de ontwikkeling van vermoeiingsschade op een zeer efficiënte manier onderzoeken en kan een kwantitatieve relatie leggen tussen de materiaalstructuur en het globale vermoeiingsgedrag. Bovendien kan het ook waardevol inzicht verschaffen in de ontwikkeling van vermoeiingsschade, respectievelijk vermoeiingsbreukverschijnselen onder verschillende spanningsniveaus.

Ten slotte wordt een multiparameter schema aangenomen voor het opschalen van de mechanische en vermoeiingseigenschappen. Via deze benadering kan het globale breukgedrag (d.w.z. spanning-reakrespons en *S-N*-relatie) op kleinere schaal worden gesimuleerd en gebruikt als input voor de vermoeiingsbreukmodellering op grotere schaal. Het model kan scheurpatronen, mechanische en vermoeiingseigenschappen onder vermoeiingsbelasting bevredigend voorspellen. Vanwege de voorspellende mogelijkheden van het model op mesoschaal en biedt het model de mogelijkheid voor gedetailleerd onderzoek naar de invloed van materiaalstructuren op verschillende schaalniveaus op het macroscopische vermoeiingsgedrag.

## ACKNOWLEDGEMENTS

The process of completing a PhD can be very lonely and strenuous. Luckily, I was accompanied by many generous and supportive people throughout the whole journey. I would never have been able to complete this challenging mission without their invaluable help, either in my personal or professional life, and sometimes in both. At the end of this thesis, I would like to take this opportunity to thank all of them.

Foremost, I would like to express my sincere gratitude to my promotor Prof. Klaas van Breugel for his guidance, patience and motivation over the whole course of my research. I profited tremendously from his unique insights and his striving for clarity and precision. At every meeting, he kept encouraging me to dig deeper into my research. We held so many fruitful discussions and he always spiced up our conversations with incisive questions. Discussions with Klaas not only brought new understandings on my current work, but also raised new challenges that I needed to face with. He was always patient and careful to review all my manuscripts and gave many insightful and constructive comments. I may still struggle to say exactly what I mean when I write, but his emphasis on clear and precise scientific writing has helped me understand and communicate my research better.

I also would like to express my great appreciation to Prof. Erik Schlangen, firstly for his continuous support and guidance throughout my PhD period, and secondly for allowing me a great amount of freedom to develop my own research interests. Erik is inspirational, passionate and kind-hearted. I am very grateful to him for boosting my curiosity and passion on my research. Whenever I was struggling to overcome obstacles, he was always there to enlighten me with his knowledge and wisdom. He is not only a good promoter but also a life coach to me. I still remember the little pep talk he gave to me before my first presentation at a conference. His encouragements and positive attitude helped me to build more self-confidence. I would never have had such memorable experiences in TU Delft without his persistent support and help.

I am immensely thankful to my daily supervisor, Dr. Branko Šavija, for providing timely and constructive feedback and assisting me on my path to completion. I count myself very fortunate to have a supervisor so interested in my work and dedicated to my development, both inside and outside academia. He is always supportive and inspiring to me. He helped me to improve my research skills and incentivised me to strive towards my goal. I really appreciated his thoughtful comments, which enabled me to mature my ideas. I am also very grateful to him for tirelessly answering endless questions and generously sharing many interesting ideas. Working with Branko has yielded many of the most exciting moments of the past few years. My research would not be running well without his supervision.

I am very thankful to all the committee members: Prof. Wei Chen, Prof. Henrik Stang, Prof. Bert Sluys, Prof. Rinze Benedictus and Prof. Max Hendriks for taking the

time and effort to carefully review the thesis draft, and also for their availability and willingness to serve on my defence committee. My appreciation extends to Prof. Matthieu Vandamme for productive discussions and sharing his expertise and knowledge. I deeply appreciate his precious help and valuable comments.

My great gratitude goes to Dr. Guang Ye for the consideration and support, and also for the nice parties and barbecues, which made me feel at home. I also would like to thank Dr. Oguzhan Copuroglu for his valuable suggestions and help. Enormous thanks to Prof. Xudong Shao at Hunan University, who recommended me as a PhD candidate at TU Delft and has been supporting me to pursue an academic career.

I would like to acknowledge China Scholarship Council (CSC) and Delft University of Technology (TU Delft). The research work reported in this thesis was sponsored by these institutes.

My deep appreciation goes to Hongzhi Zhang for his friendship and continuous support, without which I would have never been able to embark in such amazing journey in the first place. The enthusiasm he has for the research is extremely contagious and our countless brainstorming discussions were so much fun. I truly enjoyed the moments that we shared together.

I wish to thank all my present and former colleagues, especially Hua Dong, Zhiwei Qian and Xu Ma for their precious help and support at the beginning of my journey. My gratitude also goes to Claudia Romero Rodríguez, Fernando Franca de Mendonca Filho, Stefan Chaves Figueiredo, Bart Hendrix and Amir Tabakovic for the encouragements, valuable help and interesting discussions. My appreciation extends to Shi Xu, Wenjuan Lyu, Jiayi Chen, Tianshi Lu, Shizhe Zhang, Zhenming Li, Xiaowei Ouyang, Xuliang Hou, Zhipei Chen, Yibing Zuo, Hao Huang, Bei Wu and Yong Zhang for the help and support, and also for the nice parties and stories.

I am very grateful to those who assisted me in my experimental works: Arjan Thijssen, Maiko van Leeuwen, John van den Berg and Ton Blom for their unfailing support and help. My appreciation also extends to our secretary group: Jacqueline van Unen-Bergenhengouwen, Jaap Meijer, Iris Batterham and former secretary Claire de Bruin for their kind help on various daily issues.

I would like to thank my officemates Yu Chen, Emanuele Rossi and Yask Kulshreshtha for the friendship and all the great times that we have shared. My special appreciation goes to Yading Xu, Minfei Liang, Ze Chang, Zhi Wan, Shan He and Yu Zhang for the interesting discussions and nice collaboration. It is really my honor to work with these diligent, intelligent and energetic young researchers. Many thanks to Henk Jonkers, Albina Kostiuhenko, Boyu Chen, Xuhui Liang, Zhiyuan Xu, Yun Chen, Xingliang Yao, Yitao Huang, Chen Liu, Zixia Wu, Kuba Pawlowicz, Anne Linde van Overmeir, Luiz Miranda de Lima Junior, Marija Nedeljković and Patrick Holthuizen for their friendship, support and discussions.

I am also very thankful to friends that I met in Delft, Sihang Qiu, Shushuai Li, Xuehui Zhang and Renfei Bu. Thanks for the warm friendliness and encouragement. Additionally, I would like to express my gratitude to my landlord, Adriaan van der Burgh, for his generous support and help.

I am forever grateful to my dear parents and parents-in-law, who have made untold sacrifices. Without their unconditional love and support, I would never have had such colorful and enjoyable life. I hope that I will make them proud.

Lastly and most importantly, I would like to express my deepest gratitude to my gorgeous and elegant wife Jingcun Cheng for all she has done to support my studies. There is no doubt that travelling to the other side of the world for me is a huge sacrifice and an act of love. Whether near or afar, she has taken the brunt of my stress and excitement, neither of which are easy to handle. I am so lucky to have her by my side on this journey.

Yidong Gan(甘屹东)  
July, 2022

# LIST OF PUBLICATIONS

## JOURNAL PUBLICATIONS

**Gan, Y.**, Zhang, H., Šavija, B., Schlangen, E., & Van Breugel, K. (2018). Static and fatigue tests on cementitious cantilever beams using nanoindenter, *Micromachines*

**Gan, Y.**, Vandamme, M., Zhang, H., Chen, Y., Schlangen, E., van Breugel, K., & Šavija, B. (2020). Micro-cantilever testing on the short-term creep behaviour of cement paste at micro-scale. *Cement and Concrete Research*.

**Gan, Y.**, Rodriguez, C., Zhang, H., Schlangen, E., & Van Breugel, K., Šavija, B., (2021). Modelling of microstructural effects on the creep of hardened cement paste using an experimentally-informed lattice model. *Computer-Aided Civil and Infrastructure Engineering*.

**Gan, Y.**, Rodriguez, C., Schlangen, E., van Breugel, K., Šavija, B. (2021). Assessing strain rate sensitivity of cement paste at the micro-scale through micro-cantilever testing, *Cement and Concrete Composites*.

**Gan, Y.**, Zhang, H., Zhang, Y., Xu, Y., Schlangen, E., van Breugel, K., & Šavija, B. (2021). Experimental study of flexural fatigue behaviour of cement paste at the microscale, *International Journal of Fatigue*.

**Gan, Y.**, Vandamme, M., Chen, Y., Schlangen, E., van Breugel, K., & Šavija, B. (2021). Experimental investigation of the short-term creep recovery of hardened cement paste at micrometre length scale, *Cement and Concrete Research*.

**Gan, Y.**, Zhang, H., Liang, M., Schlangen, E., van Breugel, K., & Šavija, B. (2021). A numerical study of fatigue of hardened cement paste at the microscale, *International Journal of Fatigue*.

**Gan, Y.**, Zhang, H., Liang, M., Zhang, Y., Schlangen, E., van Breugel, K., & Šavija, B. (2022). Flexural strength and fatigue properties of interfacial transition zone at the microscale, *Cement and Concrete Composites*.

Zhang, H., **Gan, Y.\***, Xu, Y., Zhang, S., Schlangen, E., & Šavija, B. (2019). Experimentally informed fracture modelling of interfacial transition zone at micro-scale. *Cement and Concrete Composites*

Liang, M., **Gan, Y.\***, Chang, Z., Wan, Z., Schlangen, E., & Šavija, B. (2021). Microstructure-Informed Deep Convolutional Neural Network for Predicting Short-Term Creep Modulus of Cement Paste, *Cement and Concrete Research*.

Liang, M., Chang, Z., Wan, Z., **Gan, Y.\***, Schlangen, E., & Šavija, B. (2021). Interpretable Ensemble-Machine-Learning Models for Predicting Creep Behavior of Concrete, Cement and Concrete Composites.

## CONFERENCE PROCEEDINGS

**Gan, Y.**, Zhang, H., Šavija, B., Schlangen, E., & van Breugel, K. (2019). Micro-cantilever testing of cementitious materials under various loading conditions. In Proceedings of the 10th International Conference on Fracture Mechanics of Concrete and Concrete Structures.

**Gan, Y.**, Zhang, H., Šavija, B., Schlangen, E., & van Breugel, K. (2021). Microprism compression investigation of short-term creep behavior of cement paste at the microscale. In Proceedings of the Biot-Bažant Conference on Engineering Mechanics and Physics of Porous Materials.



# CURRICULUM VITAE

**YIDONG GAN**



**14-11-1991**      **Born in Hunan, China**

Email: ganyd@outlook.com

## **Education**

2010-2014	B.Sc. student Civil Engineering Hunan University, China
2014-2017	M.Sc. student Bridge Engineering Hunan University, China
2017-Present	Ph.D. candidate Civil Engineering and Geosciences Delft University of Technology, The Netherlands

  
**TU Delft**

